Influences of Higher Order Modeling Techniques on the Analysis of Layered Viscoelastic Damping Treatments

Eric Michael Austin

Dissertation submitted to the Faculty of the
Virginia Polytechnic Institute and State University
in partial fulfillment of the requirements for the degree of

Doctor of Philosophy
in
Engineering Mechanics

Daniel J. Inman, Chair
Romesh C. Batra
David A. Dillard
Scott L. Hendricks
William R. Saunders

November, 1998
Blacksburg, Virginia

Keywords: Viscoelasticity, Damping, Sandwich Beams

Influences of Higher Order Modeling Techniques on the
Analysis of Layered Viscoelastic Damping Treatments

Eric Michael Austin

(ABSTRACT)

Much of the work done on active and passive constrained layer beams is done with mathematical models proposed by Kerwin and extended by DiTaranto, Mead and Markus, and others. The mathematics proposed by these early researchers was tailored to fit the damping treatments in use at that time: thin foil damping tapes applied to panels for noise reduction. A key assumption was that all layers had identical transverse displacements. While these assumptions are reasonable when the core layer, normally a soft viscoelastic material(VEM), is thin and the constraining layer is weak in bending, there are many situations in industry and in the literature where the "Mead and Markus" (MM) assumptions should be questioned. An important consequence of the MM modeling assumptions is that the strain energy in the VEM core is dominated by shear strain, and this in turn means that only the shear modulus is of primary importance. This is fortunate since only the shear modulus is available to engineers for viscoelastic materials used for layered damping treatments. It is a common practice in industry and academia to simply make an educated guess of the value of Poisson's ratio. It is shown in the dissertation that this can result in erroneous predictions of damping, particularly in partial-coverage configurations. Finite element analysis is used to model both the MM assumptions and a less-restrictive approach commonly used in industry. Predictions of damping from these models are compared against models with elements from C^0 elements and a C^1-capable element that matches tractions at material interfaces. It is shown that the time-honored modal strain energy method is a good indicator of modeling accuracy. To assess the effects of the MM assumptions on an active PZT used as a constraining layer, closed-loop damping versus gain is determined using both the MM and higher order elements. For these analyses, the time-dependent properties of the viscoelastic material are represented by a Maxwell model using internal variables. Finally, the basic MM premise that all layers share the same transverse displacement is disproved by experiment.

Dedication

I dedicate this to my wife, Elizabeth, and our children, Margaret Ann and Gavin Winchester. I also dedicate this to my parents, George W. and Dolores A. Austin, to whom I owe the most. That they were not able to share this with my family and me is a source of great sorrow.

Acknowledgments

The love and support from my wife over the past few years has been immeasurable. The effort and number of hours Liz put in raising two small children with a part-time dad is humbling to me. Thanks to Maggie for letting Daddy go to the office far too often and too long, and thanks to Gavin for always being awake to greet me when I eventually came home. Come to think of it, he was always awake, period. I guess two good sleepers in a row would be too much to ask.

Thanks to my sister, Drew Austin, for the love and support over the years, especially in making the decision to return to school and pursue an academic career. She is a gifted educator, and her creative teaching has always been an inspiration to me. Many thanks also to Betty and Bernard Goodpaster for their welcome visits to provide grandparenting for the kids, relief for their daughter, and support for their "favorite" (only) son-in-law.

Next I'd like to acknowledge the three individuals who have had the most influence on my professional life. First was Professor Lawrence A. Bergman of the University of Illinois at Urbana-Champaign. It was Larry's voice of experience that suggested to me as an undergraduate that a Master's degree with a combination of finite element and vibration courses would be very marketable. He was right, and he thus formed the model of a professor with an industry perspective that I hope to emulate. To this day I still call him for advice. Next was Dr. Conor D. Johnson of CSA Engineering. Conor showed a lot of confidence by inviting a 23-year-old to join a startup engineering firm as the first employee, and I can never thank him and the other founders of CSA, Drs. Warren Gibson and Dave Kienholz, enough for the education in practical engineering and the opportunity to practice over a span of 12 years. Finally, I owe a huge thanks to Professor Daniel J. Inman*, my advisor at Virginia Tech, for taking on a nontraditional student and providing constant

support, encouragement, and perspective. I've feel as if I'm learning the in's and out's of academia from a master.

I'd like to thank my committee — Professors R. C. Batra, D. A. Dillard, S. L. Hendricks, and W. R. Saunders — for their contributions through coursework and/or discussions. In particular, Professor Batra fielded many questions about finite elements and solid mechanics, and I am very grateful for his patience. Thanks also to Dr. A. R. Johnson of the Army Research Laboratory for many discussions about the implementation of Maxwell models via internal variables. Thanks to summer intern Jennifer Lowery for assisting in data collection during the tests.

Finally, I must thank all of those who have made our group a *group* over the past few years: Greg Agnes, Mauro Atalla, Sergio Carneiro*, Clay Carter, Jens Cattarius*, Dan Cole*, Prasad Gade, Myung-Hyun Kim*, Marca Lam, Don Leo, Debbie Pilkey, Brett Pokines, Ralph Rietz, and Dino Sciulli. (*regular participants in Friday lunch at Mike's) Mauro, Debbie, Greg, and Marca: Ollie thanks you for the dog-sitting. Thanks to visiting researcher Nick Perray* for translating some French papers and to officemate Jens Cattarius for translating German. An additional thanks to Jens for proofreading the dissertation with a knowledge of the English language that would put many Americans to shame. Finally, heartfelt thanks to Sergio Carneiro, whose practical engineering background and sound understanding of mechanics provided a much-needed sounding board for ideas, frustrations, and conclusions.

This work is supported by the US Army Research Office, grant number DAAG–98–1–0030, under the direction of Dr. Gary Anderson and NSF grant CMS 9713453 for which the author is grateful.

Contents

List of Figures

List of Tables

Chapter 1

Introduction

1.1 Early Applications of Viscoelastic Layers for Damping

The concept of enhancing energy dissipation by adding viscoelastic materials to a structure dates back to at least 1919 when Lord Corporation literature states that Hugh Lord began "exploring rubber bonded-to-metal components for noise and vibration control." Some of the first published works are by Liénard [55] in France and Oberst [74] in Germany. Oberst applied single homogeneous layers of damping materials to thin automotive panels to reduce acoustic emmissions. He did not develop mathematical models of the mechanics, and most of his and the followup papers [73, 72] dealt with his methods for testing the effectiveness of various configurations. Liénard had similar goals and applications. The loss mechanism in these configurations, commonly called free-layer damping, is extension within the viscoelastic layer.

1.1.1 Emergence of the Constraining Layer: Kerwin's Model

In 1957 Plass [78] studied primarily free-layer damping of circular bars, though he proposed and discussed briefly the related problem of a sandwich plate with a viscoelastic core. He assumed the facesheets to be very thin, and as a result he accounted for their stiffness only in an equivalent moment of inertia of the sandwich structure as opposed to modeling them explicitly. Kerwin [41] in 1959 was the first to present a general analysis of viscoelastic material (VEM) constrained by

another metal layer, where now the loss mechanism is primarily shear in the VEM. His models predicted attenuation of a traveling wave on either a simply supported or infinitely long beam by assigning the beam a complex composite stiffness. An important point is the target structures were thin-skin beams or plates and the damping treatments consisted of a viscoelastic material (VEM) prepackaged with a thin metal backing. Kerwin applied both prepackaged damping tapes and made-up constrained-layer damping treatments to yard-stick-size (36"×2") aluminum bars with thicknesses of 0.063, 0.125, and 0.250 inches. The later treatments consisted of a 10-mil-thick (0.010") VEM and maximum constraining-layer thickness of 20 mils. Ross, Ungar, and Kerwin [87] applied Kerwin's analysis approach to damping configurations such as multiple damping tapes (piggyback) and "spaced" damping treatments, where the damping tape is offset from the substrate by a lightweight layer, stiff in shear but weak in extension. They produced a significant number of design charts. Kerwin and Ross compared effectiveness of free- and constrained-layer damping [42] (damping tapes) on large flat plates and concluded that constrained-layer treatments are more weight efficient in most situations. DiTaranto [21] developed sixth-order equations of motion in terms of axial displacements, and Mead and Markus [59] developed sixth-order equations of motion in terms of transverse displacements. Both works used Kerwin's basic set of assumptions, and both extended Kerwin's work by allowing for general boundary conditions.

Since the 1950's, there have been many hundreds of papers published on the theory and application of constrained layer damping. While many researchers used Kerwin's basic model, some made modifications to investigate the validity of the assumptions, look for other loss mechanisms, or suit the needs of individual applications. In the context of the present work, many of these were minor changes done during an era when finite element analysis was not as economical and closed-form approximations were generally sought first. There are excellent reviews on the evolution of modeling of constrained layer damping by Nakra [64, 65, 66], Torvik [103], and Mead [58]. Nakra summarized the body of published work by saying, "Much of the work that has been done has been restricted to simple idealized structural configurations subjected to harmonic excitations; the viscoelastic material is treated linearly." Torvik reviewed the mathematics of various modeling approaches. In his 1982 retrospect, Mead [58] wrote that most authors made the same basic assumptions:

1. the core carried shear, but no normal stress, was linearly viscoelastic, and had complex shear modulus $G_c\,(1 + i\beta)$;
2. the face-plates were elastic and isotropic and suffered no shear deformation normal to the plate surface;
3. the inertia forces of transverse flexural motions were dominant, with longitudinal and rotary inertia of faceplates and core negligible;
4. all points on a line normal to the plate moved with the same transverse displacement;
5. no slip occurred at the interfaces of the core and face plates.

The authors then state that all the theories predict the same loss factors for sinusoidal modes of vibrations, and they then discuss the differences and similarities between the theories. Although Kerwin published the initial modeling assumptions, Douglas and Yang [23] in 1978 termed this set of assumptions the *Mead and Markus* [59] model. For the remainder of this dissertation, this set of assumptions will be called the Mead and Markus (MM) assumptions.

1.1.2 Engineering Design of Passive Damping Treatments

The concept of constrained-layer damping has been applied to many types of problems in the decades since Kerwin's initial work. Many can be found in the proceedings of the "Damping" conferences sponsored by the Air Force Wright Aeronautical Laboratories between 1984 and 1993 [1, 2, 3, 4, 6] as well as sessions within broader meetings such as the "SDM" conferences (see for example [5]). The relationship between damping and energy was noted by Ungar and Kerwin in 1962 [105], and in 1981 Johnson, Kienholz, and Rogers [40] published an important work on using the modal strain energy (MSE) method for damping design by finite element methods. With this, the design of damping treatments by finite elements became much easier, and analytical formulations based on the MM assumptions became less popular due to their restriction to simple geometries. As evidence of this statement, the only paper among the 58 presented at Damping '84 that used the MM assumptions was by Kerwin, and the assumptions were perfectly applicable to his study on the optimum length of constraining layers [43]. The combination of complex geometries and the MSE method made finite element methods the dominant choice for industry applications (primarily aerospace).

Applications for thin-panel damping did not disappear suddenly when the MSE method gained acceptance. Rather, new and more challenging applications arose. Of particular interest here is damping of components such as the equipment racks and stiffened panels reported in [31] and [95]. These are cases where candidate constraining layers are no longer thin panels; rather they range from composite materials to C- and I-shaped structural members. In 1962, Ross *et al.* [87] stated, "It is true of almost all practical applied damping treatments that the extensional stiffness of the layer adjoining the base plate is very small compared to that of the base plate itself, and that the stiffness of a constraining layer is at most one-fourth or one-fifth that of the plate to be damped." By stiffness they mean extensional stiffness per unit width, i.e., Young's modulus times thickness. Contrast this with references [31] and [95] and the statement in Johnson's [38] 1995 review of passive damping designs, "Instead of a constraining layer, the VEM [viscoelastic material] could be sandwiched between the base structure and built-up sections (I-beams, C-channels, hat sections, etc.)." Perhaps the first example of this concept is given by Miles [61] in a design to reduce cabin noise on the Boeing 747 aircraft. Miles and Reinhall [62] later formalized the work.

Damping problems in industry include, but certainly are not limited to, thin beams and plates. When designing a damping treatment, there are five main design options:

1. the thickness of the VEM,
2. the modulus of the VEM (frequency and temperature dependent!),
3. the location of the VEM,
4. the thickness of the constraining layer, and
5. the modulus of the constraining layer, i.e., the type of material.

The design process consists of finding the combination of the above options that results in the maximum damping for the vibration modes of interest. An effective damping treatment is one that "coaxes" strain energy into the VEM, and a good VEM is one that dissipates this energy efficiently. In situations where the substrate is very stiff and significant (5%+) damping is needed, a thick soft VEM and thin constraining layer will be ineffective. For simple beams, the optimum damping treatment occurs when the stiffness of the constraining layer is close to that of the base structure, [67] and intuitively the engineer will recognize that this trend is similar for more complicated

structures. In practical situations, the engineer's job is to maximize the damping while staying within geometry and weight constraints imposed. Sometimes extruded C- or I-sections are used as constraining elements to increase specific stiffness in local areas of a structure when wide-area coverage is not allowed. In these situations the question of whether the constraining layer is still "following" the motions of the substrate must be addressed.

1.1.3 Active Constrained-Layer Damping

The purpose of the constraining layer is to *direct* strain energy into the viscoelastic layer, where it can be dissipated. Plump and Hubbard [79] introduced the concept of an active constraining layer that could increase effectiveness of passive constrained-layer damping treatments. They in particular identified low-amplitude vibrations as a situation that would benefit:

> With a passive constrained layer damper, the shear, and therefore the energy dissipated from the structure, tends toward zero as the vibration amplitude decreases. With an active constraining layer it would be possible to have finite dissipation at low amplitudes.

The authors do not cite any references on this concern, but Lagnese *et al.* [45] had shown in 1984 that material loss factors do not decrease with strain amplitude. Later, Austin *et al.* [9] showed an example where the effectiveness of a constrained-layer did not decrease with vibration amplitude. Nonetheless, the concept is well founded, and much of the research on constrained-layer damping in the 1990's had tried to increase shear in the VEM by using a piezoelectric (PZT) material as an active constraining layer. The literature on active constrained layer damping (ACLD) is summarized by Baz and Ro [17]. Piezoelectric wafers are typically thin ($\leq$ 0.015 inches), so as passive constraining layers on a much thicker substrate they should be well represented by the MM assumptions. Not surprisingly, most of the research done in academia relies on these basic assumptions when developing mathematical models. The Mead and Markus assumptions impose the constraint that all layers have the same transverse motion, so an interesting question is whether the actuated PZT (Lead Zirconate Titanate) would violate the MM assumptions given the opportunity.

1.2 Objectives

The Mead and Markus assumptions are most accurate for constraining layers weak in bending, though *engineers* such as Miles [61], Ikegami [32], Stahle [94], Johnson [38], and Austin [10] have recognized that a constraining layer stiff in bending has engineering utility. Much research has been published on maximizing damping in various configurations through wide-ranging trade studies and genetic optimization algorithms using the MM assumptions and/or cylindrical bending for mathematical convenience. The primary objective of this research is to explore from a mechanics standpoint the accuracy of the Mead and Markus modeling assumptions for full- and partial-coverage damping treatments. Finite element analysis (FEA) was chosen so that the analyses could extend outside of the realm where exact elasticity solutions exist. Using FEA also provides an important link between academic work and industry problems. What level of FEA is necessary to converge to a strain energy distribution that can be used to predict damping performance? Are linear elements sufficient? Is it necessary to match the tractions between material layers and at outside boundaries? Are extreme aspect ratios (nominally the ratio of longest to shortest element dimension) detrimental to prediction of strain energy? The first objective is therefore to determine what finite element strategy should be the baseline with which the MM model is compared. One approach would be conventional C^0 elements, i.e., elements which only guarantee continuity of displacements at element boundaries. An alternate C^1 element is developed to see if it provides better convergence for fewer degrees of freedom. In addition to these higher order approaches, a "low order" sandwich consisting of Euler-Bernoulli beams for the facesheets and bilinear C^0 elements for the core is modeled. This low-order method is the standard approach in industry [40], and the special case of a single bilinear C^0 element through the core is termed "MR" in these studies after the analytical work done by Miles and Reinhall [62].

Analytical predictions can only be as good as the material properties used in the model, and this is a particular problem when viscoelastic materials are involved [38]. The time-dependent properties of viscoelastic materials are often represented by a complex modulus approach. This is sufficient for a frequency-domain analysis, but it is inadequate for response predictions in the time domain. In order to allow time-domain simulations, another objective of the dissertation is to incorporate the VEM properties using an internal variable approach and determine if the straightforward modal

strain energy approach [40] is sufficient. The conventional wisdom on layered damping treatments is that most of the energy is dissipated by shear. This is true for thin panels with constraining layers weak in bending. For more complicated strain fields within a viscoelastic material, the mechanics of the energy dissipation is an unanswered question. In any case, only the shear modulus is available for the the vast majority of viscoelastic materials used for layered damping treatments, so for 3-D applications the "other" property must be assumed. Poisson's ratio is well-known for isotropic metals, and it is a comfortable way for engineers to define the second property needed for a VEM as well. Unfortunately, data on Poisson's ratio for elastomers is difficult to measure, and little is available for the thin viscoelastic materials typically used on layered damping treatments. Guesses on Poisson's ratio for elastomers in the damping literature range from 0.3 [62] to 0.5 [81]. An objective of this work was to determine the effect of not knowing Poisson's ratio.

Many papers have been published where the passive constraining layer was replaced by an active PZT layer. Most PZT's are thin and weak in bending, so as a passive constraining layer they should be characterized well by the Mead and Markus assumptions. An objective of this work was to determine whether this changes when feedback gain is applied by comparing MM and higher order predictions of closed-loop damping.

Finally, an experiment was performed to check the validity of the MM assumptions for constraining layers relatively thick and thin compared to the thickness of the base layer. Sandwich beams using 3M's ISD 112, a viscoelastic material used widely in industry and academia, were tested and compared to analysis. The properties for this material, like most VEM's, are measured by simple shear tests and are assumed to be linear during testing. A full-blown nonlinear analysis would require a substantial effort in material testing to characterize the VEM thoroughly for multi-axis strain states and large deformations. Damping is inherently a modal property, but the amplitude at and degree to which any particular mode participates in a response is specific to dynamic loads. Consequently, both the elastic and viscoelastic modeling are assumed linear.

Summarizing, the objectives of the research are as follows:

- implement higher order, MM (Mead-Markus), and MR (Miles-Reinhall) finite element models of sandwich beams,

- investigate the effect of higher order modeling on full- and partial-coverage passive and active damping treatments,
- investigate the consequences of guessing at Poisson's ratio for the VEM,
- determine whether applying a gain to a PZT used as the constraining layer changes the ability of the MM model to predict closed-loop damping,
- implement linear time-dependent properties for the viscoelastic material, and
- perform a proof-of-concept experiment.

1.3 Overview of Dissertation

The literature is reviewed in Chapter 2. There are many hundreds of references on modeling of sandwich structures in the composites literature, so the scope here is limited to modeling of sandwiches specifically for damping analysis and design. The mathematics used in modeling the sandwich structures is given in Chapter 3. A key contribution is the 2-D C^1-capable element that matches tractions at material interfaces in a functional sense. A family of C^0 elements is presented along with the mathematics necessary to model the Mead-Markus and Miles-Reinhall approaches. The aspects of viscoelasticity used in the dissertation are discussed in Chapter 4. Generalized Maxwell models are used for the viscoelasticity following mathematics describe by Johnson *et al.* [34, 37]. The analytical studies are described and reported in Chapter 5. The C^0 and C^1 elements are first compared to Pagano's [76] elasticity results for cylindrical bending to draw conclusions about mesh sizes and element aspect ratios. Various results predicted by the MM and MR approaches are then compared to those predicted with a higher order element. An active constraining layer is also modeled by both MM and higher order approaches to determine if gain affects accuracy of the MM predictions. Experimental evidence that the MM assumptions do not work well for thick or stiff-in-bending constraining layer is reported in Chapter 6. Finally, conclusions, contributions, and future work are discussed in Chapter 7.

Chapter 2

Review of Literature

2.1 Deviations from the Mead and Markus Model

The focus of this work is on the state of stress and strain within the viscoelastic core. The large majority of academic research to this day is performed with models assuming a constant shear strain through the thickness of the VEM. This is a reasonable assumption when a constraining layer is weak in bending and thus follows the transverse deflections of the base layer. The remainder of this section will discuss literature, more directly related to the dissertation, in one or more of the following categories:

- facesheets with independent transverse displacements
- core strain more than simple shear
- partial coverage
- higher order modeling of sandwich structures

Some of these are necessarily interrelated, especially the first two. Below is a discussion of the key literature in these areas.

2.1.1 Facesheets with Independent Transverse Displacements

Considering all the papers published on constrained-layer damping, there are relatively few that model independent transverse displacements of the facesheets.

Ojalvo (1977) [75]

Ojalvo analyzed soft-core sandwiches with identical Euler beams for the facesheets. He assumed linear variations in axial and transverse displacements within the VEM core and derives a closed-form solution for pinned-pinned beam. Ojalvo did not address damping problems.

Douglas and Yang (1978) [23]

Douglas and Yang model the facesheets as two independent Euler beams coupled by a complex-valued compressional spring (the VEM). They conclude that, "transverse compressional damping can provide significant attenuation in the vibrational energy of resonant structures in a narrow frequency band centered at the compressional frequency of the composite." Compressional damping is essentially a through-the-thickness mode of vibration. The authors end their paper with the following statement:

> It is concluded that shear damping is a broadband mechanism, which, for most engineering purposes and commercially available damping materials, adequately describes the damping inherent in the transverse dynamic response of thin elastic-viscoelastic-elastic beams outside the spectral influence of compressional effects. Inside this spectral band, the relative displacement between the elastic face layers of the composite must be considered in dynamic calculations.

The example problems worked by the authors are full coverage with relatively thin constraining layers, so their conclusions are justified.

Saito and Tani (1984) [88]

Similar to Douglas and Yang, Saito and Tani define independent cantilever Euler beams. The difference is they are joined at the free end by varying lengths of a thick pad of VEM. The shear and Young's moduli they list for their viscoelastic core are inconsistent with an isotropic material, so it remains a question what they assumed for Poisson's ratio.

Douglas (1986) [22]

Douglas expands his 1978 work with Yang to include rotary inertia and shear deformation in the elastic layers. It is a key to note that he also looks at the effects of a nearly incompressible viscoelastic damping core. On that point Douglas concludes. "...it is apparent that the compressional frequency of a three-layer damped beam with a thin relatively incompressible viscoelastic layer and low thickness-to-width ratio will be significantly affected by the Poissons ratio of the core." Again this is compressional damping, but at least he recognized the effect of Poisson's ratio when shear is not the only damping mechanism.

Miles (1984) [61]

Miles introduces the concept of a "beam damper," for which he was awarded a patent in 1984. The "beam damper" utilizes the thickness deformation in the VEM instead of just shear. There are no mathematics in this application-oriented paper. However, the analysis is included in Miles' 1986 paper with Reinhall [62].

Miles and Reinhall (1986) [62]

This is the mathematical complement to Miles' earlier work [61]. Miles and Reinhall recognize that the thickness deformation of a soft adhesive can be significant "if at least one of the metal layers is stiff in bending." They model the facesheets as Euler beams and assume linear variations of axial and transverse displacement through the VEM core. A key point that separates this work from other similar works [12, 13] is that they let their constraining layer *float* on the VEM core, i.e., it is treated as a free-free beam. Miles and Reinhall look only at full-coverage treatments, and they assume a value of 0.3 for Poisson's ratio in order to get Young's modulus from the shear modulus for the VEM.

Sylwan (1987) [97]

Sylwan writes about compressional damping in the VEM in the same manner as Douglas and Yang [23]. Sylwan shows an example where compressional damping is significant in a 1-kHz mode of a beam, but such specialized situations are of little interest in industry. It is worth noting that

Sylwan recognized that Poisson's ratio has a large effect on compressional damping, but he does not study this issue in this publication.

Bai and Sun (1993, 1995) [12, 13]

In both of these publications, Bai and Sun focus on slip at interfacial bonds between layers of a sandwich. They recognize that the facesheets must deform independently and that higher order modeling of the core is needed. They also show how their predicted results diverge from Mead and Markus' for beams with low aspect ratios. However, their end application is apparently honeycomb plates since the core is fifty times as thick as the facesheets. Additionally, they assume the core to be incompressible (Poisson's ratio = 0.5) and pin all layers at the edges. This work is not applicable to the problem of interest in the dissertation.

Taylor and Nayfeh (1997) [101, 98, 99, 100]

Taylor and Nayfeh develop a 3-D elasticity solution for damping of sandwich beams. They restrict themselves, however, by pinning all layers at the boundaries, and they do not mention any knowledge or effects of Poisson's ratio. Two of their examples are thin, full-coverage constraining layers, and the other features a relatively thin constraining layer on a very thick VEM layer.

Lee and Kim (1997) [48]

Similar to Taylor and Nayfeh, Lee and Kim's work is limited to full coverage treatments where all layers are pinned at the boundary. Similar to Miles and Reinhall [62] that assume a linear variation of the axial and transverse displacements through the VEM core. They address some important issues like Poisson's ratio and the stiffness of the constraining layer relative to the base layer, but in the context of a model unrealistic for engineering purposes.

Austin and Inman (1998) [11]

The authors extend some work by Lee *et al.* [49] for cylindrical bending to show that the MM assumptions perform poorly on a full-coverage, short-aspect-ratio beam where the constraining layer is allowed to "float."

2.1.2 Partial-Coverage Damping Treatments

Nokes and Nelson (1968) [69]

Nokes and Nelson cover the central portion of beams using the basic Kerwin and Ungar (MM) model. Their analysis structure is a steel, free-free beam 20" × 2" ×$\frac{1}{8}$" with a 0.050-inch-thick layer of VEM and a $\frac{1}{32}$-inch-thick steel constraining layer. For various values of VEM shear modulus they plot loss versus percent coverage. Their results show optimum coverages less than 100% for some combinations of VEM shear stiffness divided by constraining layer membrane stiffness.

Plunkett and Lee (1970) [80]

Plunkett and Lee's work on partial-coverage damping is widely referenced. They recognize that energy dissipation due to shear strain in the viscoelastic layer can be increased by making the constraining layer stiffer, though it appears they were referring to axial stiffness and axial vibrations. They looked at single- and multiple-layer partial coverage damping treatments under the following key assumptions:

1. The thicknesses of the constraining and constrained layers (VEM) are small compared to the base structure; thus, the bending effects in these layers are negligible, so that the constraining layer is subjected to tension only and the constrained layer is subjected to shear only;
2. Linear behavior of the VEM;
3. Poissons ratio effects are negligible;
4. Uniform shear strain is assumed through the thickness of the viscoelastic layer;
5. Uniform normal stress is assumed through the thickness of the constraining layer; and
6. The elastic moduli of the VEM layers are small in comparison with those of the constraining layer.

Plunkett and Lee showed good comparison between their analysis and experiments. The test article was a cantilever beam 6" ×$\frac{1}{2}$" ×$\frac{1}{8}$" with a 0.002-inch-thick layer of VEM and a 0.0007-inch-thick aluminum foil constraining layer.

Sylwan (1978) [96]

Sylwan's concept for partial coverage is different from the others reported here: he studied a full-coverage constraining layer attached with discrete patches of VEM in the context of civil structures, e.g., stairs, floors.

Lall, Asnani, and Nakra (1988) [46]

These authors contrast different solution approaches for a model using the standard MM assumptions.

Marcelin, Trompette, and Smati (1992) [57]

Marcelin *et al.* use optimization techniques to adjust the location and length of partial coverage damping patches. They use standard MM assumptions on a 3-mm-thick cantilevered beam with a 1.5-mm-thick, stiff (125 MPa = 18,415 psi) VEM and a 0.02-mm-thick (very thin!) constraining layer.

Baz and Ro (1993) [16]

Baz and Ro used the standard MM modeling approach to investigate partial-coverage with an active constraining layer. The authors used a complex modulus representation due to Douglas and Yang [23] for the VEM properties.

Lesieutre and Lee (1996) [52]

Besides presenting good reviews of both active constrained-layer damping and internal variable methods for viscoelasticity, Lesieutre and Lee make the point that a segmented active constraining layer is more robust than a continuous one because of possible phase problems in the mode shapes in the latter. The authors do not attempt to maximize performance by changing the number, size, or location of the segments.

Lam (1997) [47]

Lam investigates partial-coverage damping with passive and active partial-coverage constraining layers. The time dependency of the VEM is modeled by the GHM [28] method.

2.1.3 Higher Order Modeling of Sandwich Structures for Damping

Higher order is inherently a relative term. Here it refers to displacement fields of order higher than the linear variations in Euler-Bernoulli beam and Kirchhoff plate theories. There have been hundreds, if not thousands, of papers published on the modeling of sandwich structures, most directed specifically at composite materials. Many authors have explored the merits of higher order modeling, and there is no attempt to review this large body of work here since good reviews have been written by Noor and Burton [71], Reddy [83, 84], Librescue and Reddy [54], and Tessler [102]. When the scope is narrowed to higher order modeling for the purpose of damping analysis, there are relatively few publications, explicitly discussed below.

Dubbelday (1986) [24]

Dubbelday constructs a hybrid model in which a 10-cm-thick baselayer is analyzed by exact elasticity and relatively thin VEM and constraining layers follow the MM assumptions. The author's analysis centers around wave motion in a thick base layer, and he shows that his analysis diverges from Kerwin's at frequencies above 1 kHz.

Imaino and Harrison (1991) [33]

These authors approach higher order analysis via p-version finite elements. They first reproduce successfully an example done by Lall *et al.* [46]. They then make some good points about whether or not the constraining layer follows the base layer for various stiffnesses of VEM core. They address full coverage using a made-up complex-modulus VEM, but they do not address any Poisson's ratio effects.

Agnes (1995) [7]

Agnes adopts a variational asymptotic approach to capture the sharp gradients that exist in the stress field at the border between two materials of greatly differing modulus. It is not clear if this level of modeling is warranted, though it represents an elegant approach to higher order modeling. The example problems are full coverage of thin plates, so there is no reason to explore issues related to Poisson's ratio.

Bhimaraddi (1995) [18]

Bhimaraddi does a nice job of higher order modeling of all the layers, but he does so under the restriction that all the layers have the same transverse displacements. His examples are cylindrical bending.

Taylor and Nayfeh (1997) [101, 98, 99, 100]

See discussion in Section 2.1.1 above.

2.1.4 Summary

Of all the work found in the literature, only Miles [61, 62] recognizes that a stiff, floating constraining layer can be beneficial in increasing damping in some practical engineering situations. The other works cited either looked at compressional damping or took the mathematically convenient step of pinning the structures at the boundaries; a situation not practical in most engineering situations. The goal of this research is to suggest that partial constrained layer damping can be exploited much the same way Miles exploited the full-coverage damping. At the same time more attention will be paid to materials aspects — specifically the need for detailed material propertied beyond the normal shear modulus measured currently.

Chapter 3

Modeling of Sandwich Beams

3.1 Development of the Equations of Motion

Equilibrium and energy methods are the two choices for deriving the equations of motion of a dynamic system. Most of the early authors (e.g., [78, 41, 87, 21, 59, 80, 75, 88, 79, 97, 14]) derived equations of motion by enforcing equilibrium for the layered structure. More recently, energy methods have become popular ([62, 15, 13, 18, 53, 91, 48]). Taylor and Nayfeh [101] derive equations of motion directly from the momentum equations for a 3-D continuum under restrictions discussed in Section 2.1.1. The equations of motion in this dissertation are developed using energy via Hamilton's principle[90]:

$$\delta \left(\int_{t_1}^{t_2} (T - U - V)\, dt \right) = 0, \tag{3.1}$$

where

T = kinetic energy,

U = strain energy, and

V = potential energy of external forces.

Consider a continuum with displacements u_i (i = 1,2,3) over some domain Ω with tractions $T_i^{(\nu)}$ applied over some portion of the boundary S where displacements are not specified. The kinetic

energy assuming mass density ρ is

$$T = \frac{1}{2} \int_{\Omega} \rho \frac{\partial u_i}{\partial t} \frac{\partial u_i}{\partial t} d\Omega, \tag{3.2}$$

and its first variation in Equation (3.1) follows using integration by parts.

$$\begin{aligned} \delta \int_{t_1}^{t_2} T dt &= \delta \int_{t_1}^{t_2} \int_{\Omega} \rho \left(\frac{\partial u_i}{dt} \right) \delta \left(\frac{\partial u_i}{\partial t} \right) d\Omega dt \\ &= \int_{\Omega} \rho \left(\frac{\partial u_i}{dt} \delta u_i \Big|_{t_1}^{t_2} - \int_{t_1}^{t_2} \frac{\partial^2 u_i}{\partial t^2} \delta u_i dt \right) d\Omega \\ &= \int_{t_1}^{t_2} \left(- \int_{\Omega} \rho \frac{\partial^2 u_i}{\partial t^2} \delta u_i d\Omega \right) dt \end{aligned} \tag{3.3}$$

A condition of Hamilton's principle is that the variation in the path (δu_i) is zero at times t_1 and t_2. Considering only external tractions, the potential energy V is

$$V = - \oint_{S} T_i^{(\nu)} u_i dS, \tag{3.4}$$

which yields the straightforward first variation

$$\delta V = - \oint_{S} T_i^{(\nu)} \delta u_i dS. \tag{3.5}$$

To compute the strain energy, first assume there exists a strain energy density function W so that the stresses obey $\tau_{ij} = \frac{\partial W}{\partial \epsilon_{ij}}$. (Much of this discussion comes from Sokolnikoff's [93] excellent discription of strain energy density functions). Retaining only the six unique components of stress and strain, Sokolnikoff writes $\tau_i = \frac{\partial W}{\partial \epsilon_i}$ and gives the strain energy density function as

$$W = \frac{1}{2} c_{ij} \epsilon_i \epsilon_j \tag{3.6}$$

Writing the constitutive relationship

$$\tau_i = c_{ij} \epsilon_j, \tag{3.7}$$

Equation (3.6) can be written as the Clapeyron formula [93]

$$W = \frac{1}{2} \tau_i \epsilon_i \qquad (i = 1, 2, \ldots, 6). \tag{3.8}$$

The strain energy of the continuum is the strain energy density integrated over the domain:

$$U = \int_{\Omega} W d\Omega = \frac{1}{2} \int_{\Omega} c_{ij} \epsilon_i \epsilon_j d\Omega \tag{3.9}$$

The first variation of this assuming c_{ij} symmetric is

$$\delta U = \int_{\Omega} c_{ij} \epsilon_i \delta\epsilon_j d\Omega = \int_{\Omega} \tau_j \delta\epsilon_j d\Omega \tag{3.10}$$

Substitution of Equations (3.3), (3.5), and (3.10) into Equation (3.1) yields

$$\int_{t_1}^{t_2} \left[-\int_{\Omega} \rho \frac{\partial^2 u_i}{\partial t^2} \delta u_i d\Omega - \int_{\Omega} c_{ij} \epsilon_i \delta\epsilon_j d\Omega + \oint_{S} T_i^{(\nu)} \delta u_i dS \right] dt = 0 \tag{3.11}$$

Since the variations must be arbitrary, the bracketed term in Equation (3.11) must be zero, and the equations of motion (consistant with [90]) can be written

$$\int_{\Omega} \rho \frac{\partial^2 u_i}{\partial t^2} \delta u_i d\Omega + \int_{\Omega} c_{ij} \epsilon_i \delta\epsilon_j d\Omega = \oint_{S} T_i^{(\nu)} \delta u_i dS \tag{3.12}$$

Most of the work in this dissertation deals with free vibrations, so only the kinetic and strain energies apply. The integrations over the domain of the sandwich beams are done as integrals over the subdomains of each layer. The sections that follow describe how these energies are determined for sandwich models with various kinematic assumptions.

3.2 C^0 Finite Elements

C^0 finite elements are elements that exhibit C^0 continuity, i.e., only the displacements, not their slopes, are continuous at element boundaries. Robbins and Reddy [86] make a case for using C^0 continuity where transverse stresses are important. C^0 continuity means that transverse strains are not necessarily continuous across element boundaries, and on that subject Robbins *et al.* say

> This leaves the possibility that the transverse stresses will be continuous across thickness subdivisions boundaries that represent the interface between non-similar material layers. Note that the use of piecewise Hermite interpolation through the thickness is kinematically incorrect for general laminates since the transverse strains are forced to be continuous through the thickness.

The second point will be addressed in Section 3.3. In that same reference the authors say the following about C^0 continuity:

> Any desired degree of displacement variation through the thickness is easily obtained by either adding more one-dimensional finite element subdivisions through the thickness or using higher-order Lagrangian interpolation polynomials through the thickness.

A goal of this dissertation is to look at problems of engineering interest, which in most cases do not coincide with problems possessing closed-form solutions. Thus, higher order C^0 elements are used to produce the baseline results against which the other modeling techniques are compared.

3.2.1 Shape Functions

The purpose of shape, or interpolation, functions is to relate element degrees of freedom (DOFs) to the displacement field. C^0 elements with 4, 8, 12, 16, and 20 nodes were implemented. The shape functions for a basic four-node "master" element (Figure 3.1) can be found in any book on finite elements (for example, see Reddy [85]) to be

$$\begin{aligned} N_1(\xi,\zeta) &= \frac{1}{4}(1-\xi)(1-\zeta) & \qquad N_3(\xi,\zeta) &= \frac{1}{4}(1+\xi)(1+\zeta) \\ N_2(\xi,\zeta) &= \frac{1}{4}(1+\xi)(1-\zeta) & \qquad N_4(\xi,\zeta) &= \frac{1}{4}(1-\xi)(1+\zeta) \end{aligned} \tag{3.13}$$

where $-1 \leq \xi \leq 1$ and $-1 \leq \zeta \leq 1$. If x_1 and z_1 are the physical coordinates of node 1, the mapping between the physical and master coordinates is

$$x = x_1 + \frac{l_e}{2}(\xi + 1) \quad \Longrightarrow \quad \xi = \frac{2}{l_e}(x - x_1) - 1 \tag{3.14}$$

$$z = z_1 + \frac{h_e}{2}(\zeta + 1) \quad \Longrightarrow \quad \zeta = \frac{2}{h_e}(z - z_1) - 1, \tag{3.15}$$

where l_e and h_e are the length and height of the rectangular element, as shown in Figure 3.1. The shape functions for the 8-, 12-, 16-, and 20-node serendipity elements, i.e., rectangular elements with no interior nodes, are listed in Appendix A.

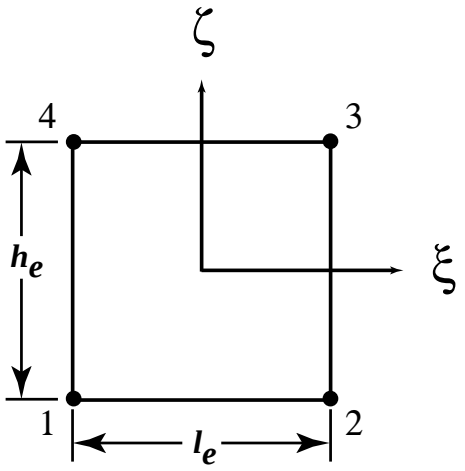

Figure 3.1: Node points for an four-node C^0 element

3.2.2 Equations of Motion

The procedure for finding the equations of motion is independent of the order of shape functions used. Each node in Figure 3.1 has an axial DOF U_i and a transverse DOF W_i, so the number of DOFs on an element is twice the number of nodes. Both the axial and transverse displacements are defined with the same set of shape functions, e.g., Equation (3.13), so the displacements over a general C^0 element are

$$\begin{aligned} u^e(\xi,\zeta) &= \{N_u(\xi,\zeta)\}^T \{a\} \\ w^e(\xi,\zeta) &= \{N_w(\xi,\zeta)\}^T \{a\} \end{aligned} \tag{3.16}$$

where

$$\{a\} = \begin{Bmatrix} U_1 \\ W_1 \\ U_2 \\ W_2 \\ \vdots \\ U_n \\ W_n \end{Bmatrix}, \quad \{N_u(\xi,\zeta)\} = \begin{Bmatrix} N_1(\xi,\zeta) \\ 0 \\ N_2(\xi,\zeta) \\ 0 \\ \vdots \\ N_n(\xi,\zeta) \\ 0 \end{Bmatrix}, \quad \text{and} \quad \{N_w(\xi,\zeta)\} = \begin{Bmatrix} 0 \\ N_1(\xi,\zeta) \\ 0 \\ N_2(\xi,\zeta) \\ \vdots \\ 0 \\ N_n(\xi,\zeta) \end{Bmatrix} \tag{3.17}$$

for a n-node element. The element DOF vector, $\{a\}$, as well as all other forms of generalized coordinates in this chapter are functions of time, and the (t) is left off only for clarity. The linear

strains over an element are

$$\epsilon_x = \frac{\partial u^e}{\partial x} = \frac{\partial u^e}{\partial \xi}\,\frac{\partial \xi}{\partial x} = \frac{2}{l_e}\,\frac{\partial u^e}{\partial \xi} \tag{3.18}$$

$$\epsilon_z = \frac{\partial w^e}{\partial z} = \frac{\partial w^e}{\partial \zeta}\,\frac{\partial \zeta}{\partial z} = \frac{2}{h_e}\,\frac{\partial w^e}{\partial \zeta} \tag{3.19}$$

$$\gamma_{zx} = \frac{\partial u^e}{\partial z} + \frac{\partial w^e}{\partial x} = \frac{\partial u^e}{\partial \zeta}\,\frac{\partial \zeta}{\partial z} + \frac{\partial w^e}{\partial \xi}\,\frac{\partial \xi}{\partial x} = \frac{2}{h_e}\,\frac{\partial u^e}{\partial \zeta} + \frac{2}{l_e}\,\frac{\partial w^e}{\partial \xi}, \tag{3.20}$$

where the derivatives $\frac{\partial \xi}{\partial x}$ and $\frac{\partial \zeta}{\partial z}$ come from Equation (3.14). Note that $\frac{\partial \xi}{\partial z}$ and $\frac{\partial \zeta}{\partial x}$ are zero for right retangular elements.

Substituting the displacements as defined in Equation (3.16) the strains become

$$\{\epsilon\} = \begin{Bmatrix} \epsilon_x \\ \epsilon_z \\ \gamma_{zx} \end{Bmatrix} = \begin{bmatrix} \frac{2}{l_e}\frac{\partial \{N_u\}^T}{\partial \xi} \\ \frac{2}{h_e}\frac{\partial \{N_w\}^T}{\partial \zeta} \\ \frac{2}{h_e}\frac{\partial \{N_u\}^T}{\partial \zeta} + \frac{2}{l_e}\frac{\partial \{N_w\}^T}{\partial \xi} \end{bmatrix} \{a\} = [B]\,\{a\}\,. \tag{3.21}$$

The 2-D problem (either plane strain or plane stress) defined by the displacement field has a reduced [30] constitutive relationship of the form

$$\begin{Bmatrix} \tau_x \\ \tau_z \\ \tau_{zx} \end{Bmatrix} = \begin{bmatrix} Q_{11} & Q_{13} & 0 \\ Q_{13} & Q_{33} & 0 \\ 0 & 0 & Q_{55} \end{bmatrix} \begin{Bmatrix} \epsilon_x \\ \epsilon_z \\ \gamma_{zx} \end{Bmatrix} \tag{3.22}$$

Use this to get the stresses and strain energy

$$U^e = \frac{1}{2}\int_{\Omega^e} \{\epsilon\}^T\,\{\sigma\}\,d\Omega^e = \frac{1}{2}\,\{a\}^T\,[k^e]\,\{a\}\,, \tag{3.23}$$

where the element stiffness matrix is

$$[k^e] = \int_{\Omega^e} [B]^T\,[Q]\,[B]\;dx\,dz. \tag{3.24}$$

The Jacobian matrix [85] is

$$[J] = \begin{bmatrix} \frac{\partial x}{\partial \xi} & \frac{\partial z}{\partial \xi} \\ \frac{\partial x}{\partial \zeta} & \frac{\partial z}{\partial \zeta} \end{bmatrix} = \begin{bmatrix} \frac{l_e}{2} & 0 \\ 0 & \frac{h_e}{2} \end{bmatrix} \tag{3.25}$$

from which the Jacobian, $\mathcal{J}$, the determinant of Equation (3.25) is

$$\mathcal{J} = \det[J] = \frac{\partial x}{\partial \xi}\,\frac{\partial z}{\partial \zeta} - \frac{\partial z}{\partial \xi}\,\frac{\partial x}{\partial \zeta} = \frac{l_e\,h_e}{4}. \tag{3.26}$$

The Jacobian allows the area element $dx\,dz$ in Equation (3.24) to be written as $\mathcal{J}\,d\xi\,d\zeta$, so the element stiffness matrix can be written as

$$[k^e] = \int_{-1}^{1}\int_{-1}^{1} [B]^T [Q] [B]\ \mathcal{J}\,d\xi\,d\zeta. \tag{3.27}$$

Similarly, the kinetic energy from Equation (3.2) is

$$\begin{aligned} T^e &= \frac{1}{2}\int_{\Omega^e} \rho \left[\left(\{N_u\}^T \{\dot{a}\} \right)^T \left(\{N_u\}^T \{\dot{a}\} \right) + \left(\{N_w\}^T \{\dot{a}\} \right)^T \left(\{N_w\}^T \{\dot{a}\} \right) \right] d\Omega^e \\ &= \frac{1}{2} \{\dot{a}\}^T [m^e] \{\dot{a}\} \end{aligned} \tag{3.28}$$

where the element mass matrix is

$$[m^e] = \int_{-1}^{1}\int_{-1}^{1} \left[\{N_u\} \{N_u\}^T + \{N_w\} \{N_w\}^T \right] \mathcal{J}\,d\xi\,d\zeta. \tag{3.29}$$

Assemble Equations (3.27) and (3.29) to get the system-level energies and take their variations with respect to the global DOF vector $\{u\}$ as in Section 3.1.

$$T = \frac{1}{2} \{\dot{u}\}^T [M] \{\dot{u}\} \quad \Longrightarrow \quad \delta T = \{\delta u\}^T [M] \{\ddot{u}\} \tag{3.30}$$

$$U = \frac{1}{2} \{u\}^T [K] \{u\} \quad \Longrightarrow \quad \delta U = \{\delta u\}^T [K] \{u\} \tag{3.31}$$

From Hamilton's principle this leads to

$$\{\delta u\}^T \left([M] \{\ddot{u}\} + [K] \{u\} \right) = 0, \tag{3.32}$$

and the only way to satisfy this for an arbitrary variation $\{\delta u\}$ is to set

$$[M] \{\ddot{u}\} + [K] \{u\} = 0 \tag{3.33}$$

3.3 A C^1-Capable Finite Element With Traction Continuity

The goal here is to somehow enforce traction continuity at outer layer and at material boundaries to determine the effect on energy predictions. Robbins and Reddy [86] state correctly (Section 3.2) that C^1 elements are "kinematically incorrect" since they force strains to be continuous across borders with different material, thus preventing tractions from being continuous. C^1 finite elements are

elements that exhibit C^1 continuity, i.e., both displacements and slopes are continuous at element boundaries. There are several schemes for matching tractions [106, 109], but the one presented here follows work by Lee and Liu [49].

Lee and Liu introduced their strategy on an analysis of a composite beam in cylindrical bending. In their initial work they discretize the transverse direction with C^1 finite elements and assume one-function expansions in sines and cosines (as cylindrical bending allows) along the length of the beam. They match tractions at material boundaries by defining rotation DOFs on each side of the material boundary and then relating them through material properties in such a way that the appropriate tractions are continuous. Properly stated, this element is C^1 capable, not C^1 continuous. They compare very well with Pagano's test case [76] of cylindrical bending by forcing traction continuity at both material interfaces and at outer boundaries. As a final step, the authors discretize the axial direction with finite elements also and show reasonably good results. Lee and Liu's work is directed at composite materials, so they did not analyze partial coverage or any boundary conditions other then cylindrical bending. Their 2-D discretization occurred in two steps, i.e., one dimension at time, and this unnecessarily complicated the task of modeling partial coverages. The dissertation work extends Lee and Liu's work to a general 2-D element, suitable for partial coverage, that matches tractions between both dissimilar materials and at outer boundaries.

3.3.1 Equations of Motion

Lee and Liu discretize the transverse direction initially with elements as shown in Figure 3.2(a). The corresponding 2-D displacement field is

$$u_j(x, z_j) = U_j(x)\,\phi_1^j(z_j) + \hat{S}_{2j-1}(x)\,\phi_2^j(z_j) + U_{j+1}(x)\,\phi_3^j(z_j) + \hat{S}_{2j}(x)\,\phi_4^j(z_j) \tag{3.34}$$

$$w_j(x, z_j) = W_j(x)\,\phi_1^j(z_j) + \hat{R}_{2j-1}(x)\,\phi_2^j(z_j) + W_{j+1}(x)\,\phi_3^j(z_j) + \hat{R}_{2j}(x)\,\phi_4^j(z_j) \tag{3.35}$$

where $\{\phi^j(z_j)\}$ are the Hermite cubic shape functions

$$\begin{aligned}
\psi_1(z_j) &= \frac{1}{4}\left(2 - \frac{6}{h_j}z_j + \frac{8}{h_j^3}z_j^3\right) \\
\psi_2(z_j) &= \frac{h_j}{8}\left(1 - \frac{2}{h_j}z_j - \frac{4}{h_j^2}z_j^2 + \frac{8}{h_j^3}z_j^3\right) \\
\psi_3(z_j) &= \frac{1}{4}\left(2 + \frac{6}{h_j}z_j - \frac{8}{h_j^3}z_j^3\right) \\
\psi_4(z_j) &= \frac{h_j}{8}\left(-1 - \frac{2}{h_j}z_j + \frac{4}{h_j^2}z_j^2 + \frac{8}{h_j^3}z_j^3\right),
\end{aligned} \tag{3.36}$$

$\frac{-h_j}{2} \leq z_j \leq \frac{h_j}{2}$, and h_j is the thickness of the j^{th} layer. The nature of these C^1 shape functions identifies degrees of freedom $\hat{S}(x)$ and $\hat{R}(x)$ as the derivatives with respect to the through-the-thickness direction of the displacements at the layer boundaries, i.e.,

$$\hat{S}_{2j-1}(x) = \frac{\partial u_j\left(x, \frac{-h_j}{2}\right)}{\partial z_i} \qquad \hat{S}_{2j}(x) = \frac{\partial u_j\left(x, \frac{+h_j}{2}\right)}{\partial z_i} \tag{3.37}$$

$$\hat{R}_{2j-1}(x) = \frac{\partial w_j\left(x, \frac{-h_j}{2}\right)}{\partial z_i} \qquad \hat{R}_{2j}(x) = \frac{\partial w_j\left(x, \frac{+h_j}{2}\right)}{\partial z_i} \tag{3.38}$$

These degrees of freedom allow the transverse normal derivatives ($\frac{\partial}{\partial z_i}$) to be independent across layer boundaries. Next calculate the strains and key tractions at the top and bottom surfaces of an element. At the upper surface of the j^{th} element, the strains are

$$\begin{aligned}
\epsilon_x^j\left(x, \frac{h_j}{2}\right) &= \frac{\partial u_j\left(x, \frac{h_j}{2}\right)}{\partial x} = \frac{\partial U_{j+1}(x)}{\partial x} \\
\epsilon_z^j\left(x, \frac{h_j}{2}\right) &= \frac{\partial w_j\left(x, \frac{h_j}{2}\right)}{\partial z_j} = \hat{R}_{2j}(x) \\
\gamma_{zx}^j\left(x, \frac{h_j}{2}\right) &= \frac{\partial u_j\left(x, \frac{h_j}{2}\right)}{\partial z_j} + \frac{w_j\left(x, \frac{h_j}{2}\right)}{\partial x} = \hat{S}_{2j}(x) + \frac{\partial W_{j+1}(x)}{\partial x},
\end{aligned}$$

and using Equation (3.22), the two tractions to be matched are

$$\tau_z^j\left(x, \frac{h_j}{2}\right) = Q_{13}^j \frac{\partial U_{j+1}(x)}{\partial x} + Q_{33}^j \hat{R}_{2j}(x) \tag{3.39}$$

$$\tau_{zx}^j\left(x, \frac{h_j}{2}\right) = Q_{55}^j\left(\hat{S}_{2j}(x) + \frac{\partial W_{j+1}(x)}{\partial x}\right) \tag{3.40}$$

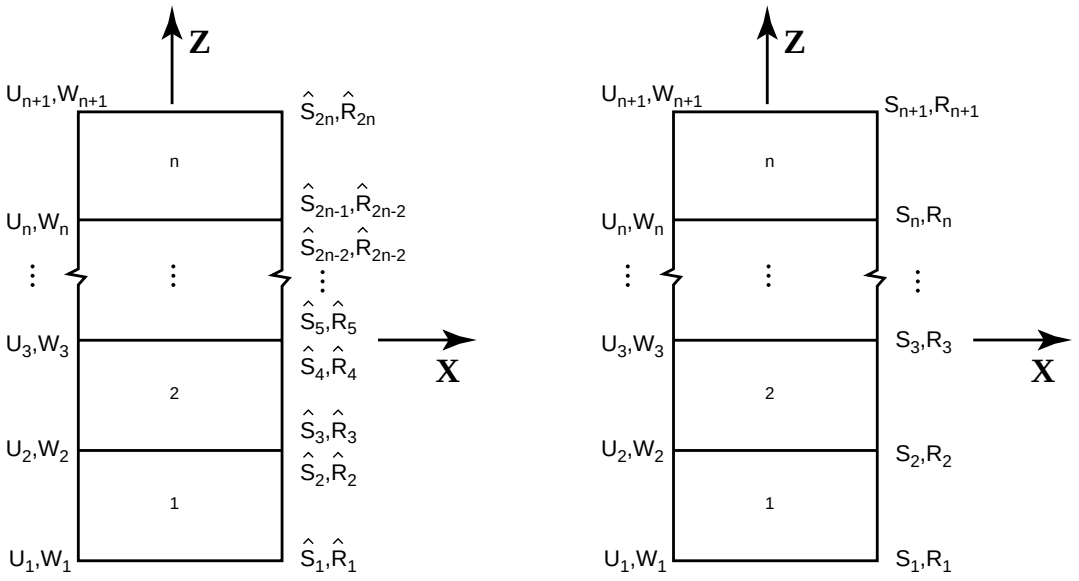

(a) Initial displacement field

(b) Final displacement field

Figure 3.2: Displacement fields for the Lee and Liu model

At the lower surface of the $(j+1)^{st}$ element, the strains are

$$\epsilon_x^{j+1}\left(x, \frac{-h_{j+1}}{2}\right) = \frac{\partial u_{j+1}\left(x, \frac{-h_{j+1}}{2}\right)}{\partial x} = \frac{\partial U_{j+1}(x)}{\partial x}$$

$$\epsilon_z^{j+1}\left(x, \frac{-h_{j+1}}{2}\right) = \frac{\partial w_{j+1}\left(x, \frac{-h_{j+1}}{2}\right)}{\partial x} = \hat{R}_{2j+1}(x)$$

$$\gamma_{zx}^{j+1}\left(x, \frac{-h_{j+1}}{2}\right) = \frac{\partial u_{j+1}\left(x, \frac{-h_{j+1}}{2}\right)}{\partial z} + \frac{w_{j+1}\left(x, \frac{-h_{j+1}}{2}\right)}{\partial x} = \hat{S}_{2j+1}(x) + \frac{\partial W_{j+1}(x)}{\partial x}$$

and the two tractions to be matched are

$$\tau_z^{j+1}\left(x, \frac{-h_{j+1}}{2}\right) = Q_{13}^{j+1}\frac{\partial U_{j+1}(x)}{\partial x} + Q_{33}^{j+1}\hat{R}_{2j+1}(x) \tag{3.41}$$

$$\tau_{zx}^{j+1}\left(x, \frac{-h_{j+1}}{2}\right) = Q_{55}^{j+1}\left(\hat{S}_{2j+1}(x) + \frac{\partial W_{j+1}(x)}{\partial x}\right) \tag{3.42}$$

Equating Equations (3.40) and (3.42) yields

$$\tau_{zx}^{j}\left(x, \frac{h_j}{2}\right) = \tau_{zx}^{j+1}\left(x, \frac{-h_{j+1}}{2}\right)$$

$$Q_{55}^{j}\left(\hat{S}_{2j}(x) + \frac{\partial W_{j+1}(x)}{\partial x}\right) = Q_{55}^{j+1}\left(\hat{S}_{2j+1}(x) + \frac{\partial W_{j+1}(x)}{\partial x}\right)$$

$$\hat{S}_{2j}(x) = \alpha^j \hat{S}_{2j+1}(x) + \beta^j \frac{\partial W_{j+1}(x)}{\partial x} \tag{3.43}$$

where

$$\alpha^j = \frac{Q_{55}^{j+1}}{Q_{55}^j} \quad \text{and} \quad \beta^j = \frac{Q_{55}^{j+1}}{Q_{55}^j} - 1 \tag{3.44}$$

Equating (3.39) and (3.41) yields

$$\begin{aligned} \tau_z^j\left(x, \frac{h_j}{2}\right) &= \tau_z^{j+1}\left(x, \frac{-h_{j+1}}{2}\right) \\ Q_{13}^j \frac{\partial U_{j+1}(x)}{\partial x} + Q_{33}^j \hat{R}_{2j}(x) &= Q_{13}^{j+1} \frac{\partial U_{j+1}(x)}{\partial x} + Q_{33}^{j+1} \hat{R}_{2j+1}(x) \\ \hat{R}_{2j}(x) &= \gamma^j \hat{R}_{2j+1}(x) + \mu^j \frac{\partial U_{j+1}(x)}{\partial x} \end{aligned} \tag{3.45}$$

where

$$\gamma^j = \frac{Q_{33}^{j+1}}{Q_{33}^j} \quad \text{and} \quad \mu^j = \frac{Q_{13}^{j+1} - Q_{13}^j}{Q_{33}^j} \tag{3.46}$$

Equations (3.43) and (3.45) enforce continuity of the tractions τ_z and τ_{zx} across the element boundary by eliminating the *degrees of freedom* $\hat{S}_{2j}(x)$ and $\hat{R}_{2j}(x)$. Figure 3.2(b) shows this, and the displacement fields can be rewritten as

$$\begin{aligned} u_j(x, z_j) &= U_j(x)\,\phi_1^j(z_j) + S_j(x)\,\phi_2^j(z_j) \\ &\quad + U_{j+1}(x)\,\phi_3^j(z_j) + \phi_4^j(z_j)\left(\alpha^j S_{j+1}(x) + \beta^j \frac{\partial W_{j+1}(x)}{\partial x}\right) \end{aligned} \tag{3.47}$$

$$\begin{aligned} w_j(x, z_j) &= W_j(x)\,\phi_1^j(z_j) + R_j(x)\,\phi_2^j(z_j) \\ &\quad + W_{j+1}(x)\,\phi_3^j(z_j) + \phi_4^j(z_j)\left(\gamma^j R_{j+1}(x) + \mu^j \frac{\partial U_{j+1}(x)}{\partial x}\right) \end{aligned} \tag{3.48}$$

where the ($\hat{}$) designations have been dropped.

At this point, Lee and Liu choose sine and cosines for the functions of x and work the cylindrical bending problem. Instead, expand these functions in terms of nodal values (U, W, S, R) and their derivatives with respect to x (U', W', S', R') with Hermite cubic shape functions in the axial direction. Define a four-node "master" element shown in Figure 3.3 where $-1 \le \xi \le 1$ and $-1 \le \zeta \le 1$ and rewrite the Hermite cubic shape functions from Equation (3.36) in terms of ξ as

$$\begin{aligned} \psi_1(\xi) &= \frac{1}{4}\left(2 - 3\xi + \xi^3\right) \\ \psi_2(\xi) &= \frac{l_e}{8}\left(1 - \xi - \xi^2 + \xi^3\right) \\ \psi_3(\xi) &= \frac{1}{4}\left(2 + 3\xi - \xi^3\right) \\ \psi_4(\xi) &= \frac{l_e}{8}\left(-1 - \xi + \xi^2 + \xi^3\right) \end{aligned} \tag{3.49}$$

where l_e is the length of the element. Consider the j^{th} element through the thickness and the i^{th} element in the axial direction as shown in Figure 3.3.

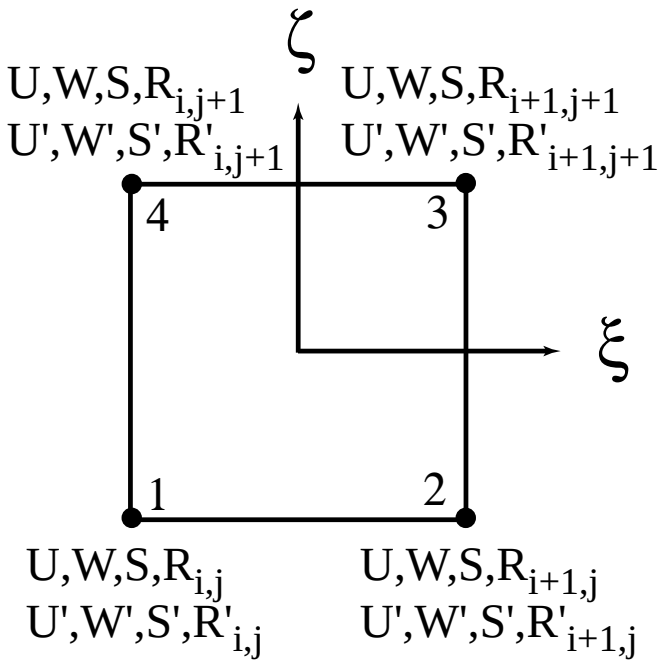

Figure 3.3: Degrees of freedom for the C^1 element

$$U_j(\xi) = U_{i,j}\psi_1(\xi) + U'_{i,j}\psi_2(\xi) + U_{i+1,j}\psi_3(\xi) + U'_{i+1,j}\psi_4(\xi) \tag{3.50}$$

$$W_j(\xi) = W_{i,j}\psi_1(\xi) + W'_{i,j}\psi_2(\xi) + W_{i+1,j}\psi_3(\xi) + W'_{i+1,j}\psi_4(\xi) \tag{3.51}$$

$$S_j(\xi) = S_{i,j}\psi_1(\xi) + S'_{i,j}\psi_2(\xi) + S_{i+1,j}\psi_3(\xi) + S'_{i+1,j}\psi_4(\xi) \tag{3.52}$$

$$R_j(\xi) = R_{i,j}\psi_1(\xi) + R'_{i,j}\psi_2(\xi) + R_{i+1,j}\psi_3(\xi) + R'_{i+1,j}\psi_4(\xi) \tag{3.53}$$

Substituting Equations (3.50) through (3.53) into Equations (3.47) and (3.48) yields the following displacement fields u^e and w^e over the element in Figure 3.3.

$$\begin{aligned} u^e(\xi,\zeta) = {} & U_{i,j}\psi_1(\xi)\,\phi_1(\zeta) + U'_{i,j}\psi_2(\xi)\,\phi_1(\zeta) + U_{i+1,j}\psi_3(\xi)\,\phi_1(\zeta) + U'_{i+1,j}\psi_4(\xi)\,\phi_1(\zeta) \\ & + S_{i,j}\psi_1(\xi)\,\phi_2(\zeta) + S'_{i,j}\psi_2(\xi)\,\phi_2(\zeta) + S_{i+1,j}\psi_3(\xi)\,\phi_2(\zeta) + S'_{i+1,j}\psi_4(\xi)\,\phi_2(\zeta) \\ & + U_{i,j+1}\psi_1(\xi)\,\phi_3(\zeta) + U'_{i,j+1}\psi_2(\xi)\,\phi_3(\zeta) + U_{i+1,j+1}\psi_3(\xi)\,\phi_3(\zeta) + U'_{i+1,j+1}\psi_4(\xi)\,\phi_3(\zeta) \\ & + \phi_4(\zeta)\left\{\alpha^j\left[S_{i,j+1}\psi_1(\xi) + S'_{i,j+1}\psi_2(\xi) + S_{i+1,j+1}\psi_3(\xi) + S'_{i+1,j+1}\psi_4(\xi)\right]\right. \\ & \left. + \beta^j\left[W_{i,j+1}\frac{d\psi_1(\xi)}{dx} + W'_{i,j+1}\frac{d\psi_2(\xi)}{dx} + W_{i+1,j+1}\frac{d\psi_3(\xi)}{dx} + W'_{i+1,j+1}\frac{d\psi_4(\xi)}{dx}\right]\right\} \end{aligned} \tag{3.54}$$

$$
\begin{aligned}
w^e(\xi,\zeta) = {} & W_{i,j}\psi_1(\xi)\,\phi_1(\zeta) + W'_{i,j}\psi_2(\xi)\,\phi_1(\zeta) + W_{i+1,j}\psi_3(\xi)\,\phi_1(\zeta) + W'_{i+1,j}\psi_4(\xi)\,\phi_1(\zeta) \\
& + R_{i,j}\psi_1(\xi)\,\phi_2(\zeta) + R'_{i,j}\psi_2(\xi)\,\phi_2(\zeta) + R_{i+1,j}\psi_3(\xi)\,\phi_2(\zeta) + R'_{i+1,j}\psi_4(\xi)\,\phi_2(\zeta) \\
& + W_{i,j+1}\psi_1(\xi)\,\phi_3(\zeta) + W'_{i,j+1}\psi_2(\xi)\,\phi_3(\zeta) + W_{i+1,j+1}\psi_3(\xi)\,\phi_3(\zeta) + W'_{i+1,j+1}\psi_4(\xi)\,\phi_3(\zeta) \\
& + \phi_4(\zeta)\left\{\gamma^j\left[R_{i,j+1}\psi_1(\xi) + R'_{i,j+1}\psi_2(\xi) + R_{i+1,j+1}\psi_3(\xi) + R'_{i+1,j+1}\psi_4(\xi)\right]\right. \\
& \qquad \left. + \mu^j\left[U_{i,j+1}\frac{d\psi_1(\xi)}{dx} + U'_{i,j+1}\frac{d\psi_2(\xi)}{dx} + U_{i+1,j+1}\frac{d\psi_3(\xi)}{dx} + U'_{i+1,j+1}\frac{d\psi_4(\xi)}{dx}\right]\right\}
\end{aligned}
\tag{3.55}
$$

Next form an element DOF vector $\{a\}$ and express the displacement fields as $u^e = \{N_u\}^T\{a\}$ and

$w^e = \{N_w\}^T \{a\}$, where

$$\{a\} = \begin{Bmatrix} U_{i,j} \\ U'_{i,j} \\ W_{i,j} \\ W'_{i,j} \\ S_{i,j} \\ S'_{i,j} \\ R_{i,j} \\ R'_{i,j} \\ U_{i+1,j} \\ U'_{i+1,j} \\ W_{i+1,j} \\ W'_{i+1,j} \\ S_{i+1,j} \\ S'_{i+1,j} \\ R_{i+1,j} \\ R'_{i+1,j} \\ U_{i+1,j+1} \\ U'_{i+1,j+1} \\ W_{i+1,j+1} \\ W'_{i+1,j+1} \\ S_{i+1,j+1} \\ S'_{i+1,j+1} \\ R_{i+1,j+1} \\ R'_{i+1,j+1} \\ U_{i,j+1} \\ U'_{i,j+1} \\ W_{i,j+1} \\ W'_{i,j+1} \\ S_{i,j+1} \\ S'_{i,j+1} \\ R_{i,j+1} \\ R'_{i,j+1} \end{Bmatrix}, \quad \{N_u\} = \begin{Bmatrix} \psi_1(\xi)\,\phi_1(\zeta) \\ \psi_2(\xi)\,\phi_1(\zeta) \\ 0 \\ 0 \\ \psi_1(\xi)\,\phi_2(\zeta) \\ \psi_2(\xi)\,\phi_2(\zeta) \\ 0 \\ 0 \\ \psi_3(\xi)\,\phi_1(\zeta) \\ \psi_4(\xi)\,\phi_1(\zeta) \\ 0 \\ 0 \\ \psi_3(\xi)\,\phi_2(\zeta) \\ \psi_4(\xi)\,\phi_2(\zeta) \\ 0 \\ 0 \\ \psi_3(\xi)\,\phi_3(\zeta) \\ \psi_4(\xi)\,\phi_3(\zeta) \\ \beta^j \frac{d\psi_3(\xi)}{dx}\phi_4(\zeta) \\ \beta^j \frac{d\psi_4(\xi)}{dx}\phi_4(\zeta) \\ \alpha^j \psi_3(\xi)\,\phi_4(\zeta) \\ \alpha^j \psi_4(\xi)\,\phi_4(\zeta) \\ 0 \\ 0 \\ \psi_1(\xi)\,\phi_3(\zeta) \\ \psi_2(\xi)\,\phi_3(\zeta) \\ \beta^j \frac{d\psi_1(\xi)}{dx}\phi_4(\zeta) \\ \beta^j \frac{d\psi_2(\xi)}{dx}\phi_4(\zeta) \\ \alpha^j \psi_1(\xi)\,\phi_4(\zeta) \\ \alpha^j \psi_2(\xi)\,\phi_4(\zeta) \\ 0 \\ 0 \end{Bmatrix}, \quad \{N_w\} = \begin{Bmatrix} 0 \\ 0 \\ \psi_1(\xi)\,\phi_1(\zeta) \\ \psi_2(\xi)\,\phi_1(\zeta) \\ 0 \\ 0 \\ \psi_1(\xi)\,\phi_2(\zeta) \\ \psi_2(\xi)\,\phi_2(\zeta) \\ 0 \\ 0 \\ \psi_3(\xi)\,\phi_1(\zeta) \\ \psi_4(\xi)\,\phi_1(\zeta) \\ 0 \\ 0 \\ \psi_3(\xi)\,\phi_2(\zeta) \\ \psi_4(\xi)\,\phi_2(\zeta) \\ \mu^j \frac{d\psi_3(\xi)}{dx}\phi_4(\zeta) \\ \mu^j \frac{d\psi_4(\xi)}{dx}\phi_4(\zeta) \\ \psi_3(\xi)\,\phi_3(\zeta) \\ \psi_4(\xi)\,\phi_3(\zeta) \\ 0 \\ 0 \\ \gamma^j \psi_3(\xi)\,\phi_4(\zeta) \\ \gamma^j \psi_4(\xi)\,\phi_4(\zeta) \\ \mu^j \frac{d\psi_1(\xi)}{dx}\phi_4(\zeta) \\ \mu^j \frac{d\psi_2(\xi)}{dx}\phi_4(\zeta) \\ \psi_1(\xi)\,\phi_3(\zeta) \\ \psi_2(\xi)\,\phi_3(\zeta) \\ 0 \\ 0 \\ \gamma^j \psi_1(\xi)\,\phi_4(\zeta) \\ \gamma^j \psi_2(\xi)\,\phi_4(\zeta) \end{Bmatrix} \tag{3.56}$$

Having defined the element DOF vector $\{a\}$ and the shape function vectors $\{N_u\}$ and $\{N_w\}$, the element mass and stiffness matrices follow directly from Equations (3.21), (3.27), and (3.29), where the constants α^j, β^j, γ^j, and μ^j must be calculated by Equations (3.44) and (3.46) at the time when the element stiffness matrices are formed. These are constants for layer j, so it is assumed that materials do not change from one element to the next in the in-plane direction. If a traction load

$q(x)$ were applied to the top surface, the potential energy from Equation (3.4) at the element level would be

$$V^e = -\int_{-1}^{1} q(\xi)\, w^e(\xi,1)\, \mathcal{J}\, d\xi = -\int_{-1}^{1} q(\xi)\, \{a\}^T \{N_w(\xi,1)\}\, \mathcal{J}\, d\xi = -\{a\}^T \{f^e\}, \tag{3.57}$$

where the element load vector $\{f^e\}$ is defined as

$$\{f^e\} = \int_{-1}^{1} q(\xi)\, \{N_w(\xi,1)\}\, \mathcal{J}\, d\xi = -\{u^e\}^T \{f^e\} \tag{3.58}$$

where the differential element of length dx is transformed to $\mathcal{J}d\xi = \frac{l_e}{2}d\xi$ and the vectors $\{N_w(\xi,1)\}$ and $\{a\}$ are given in Equations (3.56).

The kinetic energy and strain energy along with their variations can be copied from Equations (3.31) and (3.30). The potential energy due to the external traction and its variation at the system level are

$$V = -\{u\}^T \{f\} \quad \Longrightarrow \quad \delta V = -\{\delta u\}^T \{f\}, \tag{3.59}$$

where now $\{u\}$ is the global DOF vector. From Hamilton's principle this leads to

$$\{\delta u\}^T \left([M]\{\ddot{u}\} + [K]\{u\} - \{f\} \right) = 0, \tag{3.60}$$

and the only way to satisfy this for an arbitrary variation $\{\delta u\}$ is to have

$$[M]\{\ddot{u}\} + [K]\{u\} = \{f\} \tag{3.61}$$

3.3.2 Traction Continuity

The tractions between layers are matched in a functional sense through the definition of the displacement field (Equations (3.54) and (3.55)) and its associated constants (Equations (3.44) and (3.46)). The following equations are developed for matching external tractions at the upper surface, but everything presented applies to the lower surface as well with only minor changes in notation. At the upper boundary of the sandwich beam, the constants $(\alpha^j, \beta^j, \gamma^j, \mu^j)$ are taken to be (1,0,1,0),

and the displacement fields in Equations (3.47) and (3.48) simplify to

$$\begin{aligned} u_n(x,z_n) = {} & U_n(x)\,\phi_1^n(z_n) + S_n(x)\,\phi_2^n(z_n) \\ & + U_{n+1}(x)\,\phi_3^n(z_n) + S_{n+1}(x)\,\phi_4^n(z_n) \end{aligned} \tag{3.62}$$

and

$$\begin{aligned} w_n(x,z_n) = {} & W_n(x)\,\phi_1^n(z_n) + R_n(x)\,\phi_2^n(z_n) \\ & + W_{n+1}(x)\,\phi_3^n(z_n) + R_{n+1}(x)\,\phi_4^n(z_n) \end{aligned} \tag{3.63}$$

Similar to Equations (3.39) and (3.40), external tractions, zero or nonzero, are matched by the expressions

$$q_z(x) = \tau_z^n\left(x, \frac{h_n}{2}\right) = Q_{13}^n \frac{\partial U_{n+1}(x)}{\partial x} + Q_{33}^n R_{n+1}(x) \tag{3.64}$$

$$q_{zx}(x) = \tau_{zx}^n\left(x, \frac{h_n}{2}\right) = Q_{55}^n \left(\frac{\partial W_{n+1}(x)}{\partial x} + S_{n+1}(x)\right) \tag{3.65}$$

All of the material properties in the remainder of this section belong to the n^{th} layer, so the superscript n will be dropped for clarity. Expand the external tractions with the Hermite cubic shape functions over an element as

$$q_z^e(\xi) = q_{z(i)}\psi_1(\xi) + q'_{z(i)}\psi_2(\xi) + q_{z(i+1)}\psi_3(\xi) + q'_{z(i+1)}\psi_4(\xi) \tag{3.66}$$

$$q_{zx}^e(\xi) = q_{zx(i)}\psi_1(\xi) + q'_{zx(i)}\psi_2(\xi) + q_{zx(i+1)}\psi_3(\xi) + q'_{zx(i+1)}\psi_4(\xi) \tag{3.67}$$

where the primes indicate differentiation with respect to x. Next, rewrite Equation (3.64) as

$$\begin{Bmatrix} \psi_1(\xi) \\ \psi_2(\xi) \\ \psi_3(\xi) \\ \psi_4(\xi) \end{Bmatrix}^T \begin{Bmatrix} q_{z(i)} \\ q'_{z(i)} \\ q_{z(i+1)} \\ q'_{z(i+1)} \end{Bmatrix} = Q_{13}\frac{d}{dx} \begin{Bmatrix} \psi_1(\xi) \\ \psi_2(\xi) \\ \psi_3(\xi) \\ \psi_4(\xi) \end{Bmatrix}^T \begin{Bmatrix} U_{i,n+1} \\ U'_{i,n+1} \\ U_{i+1,n+1} \\ U'_{i+1,n+1} \end{Bmatrix} + Q_{33} \begin{Bmatrix} \psi_1(\xi) \\ \psi_2(\xi) \\ \psi_3(\xi) \\ \psi_4(\xi) \end{Bmatrix}^T \begin{Bmatrix} R_{i,n+1} \\ R'_{i,n+1} \\ R_{i+1,n+1} \\ R'_{i+1,n+1} \end{Bmatrix} \tag{3.68}$$

This equation does not yield relationships between degrees of freedom directly since the first term on the right-hand side is described by a different set of basis functions, i.e., $\frac{d}{dx}\{\Psi\}$, rather than $\{\Psi\}$ for the other two terms. However, there is a simple solution to this since the derivatives of the

Hermitian shape functions are within the span of the Hermitian shape functions themselves. Write the shape functions of Equation (3.49) as

$$\begin{Bmatrix} \psi_1(\xi) \\ \psi_2(\xi) \\ \psi_3(\xi) \\ \psi_4(\xi) \end{Bmatrix} = \frac{1}{8} \begin{bmatrix} 4 & -6 & 0 & 2 \\ l_e & -l_e & -l_e & l_e \\ 4 & 6 & 0 & -2 \\ -l_e & -l_e & l_e & l_e \end{bmatrix} \begin{Bmatrix} 1 \\ \xi \\ \xi^2 \\ \xi^3 \end{Bmatrix} = [N]\{b\}, \tag{3.69}$$

where as before l_e is the length of the element. Next differentiate with respect to x to get

$$\frac{d}{dx} \begin{Bmatrix} \psi_1(\xi) \\ \psi_2(\xi) \\ \psi_3(\xi) \\ \psi_4(\xi) \end{Bmatrix} = \frac{d\xi}{dx}\frac{d}{d\xi} \begin{Bmatrix} \psi_1(\xi) \\ \psi_2(\xi) \\ \psi_3(\xi) \\ \psi_4(\xi) \end{Bmatrix} = \frac{1}{4l_e} \begin{bmatrix} -6 & 0 & 6 & 0 \\ -l_e & -2l_e & 3l_e & 0 \\ 6 & 0 & -6 & 0 \\ -l_e & 2l_e & 3l_e & 0 \end{bmatrix} \begin{Bmatrix} 1 \\ \xi \\ \xi^2 \\ \xi^3 \end{Bmatrix} = [dN]\{b\} \tag{3.70}$$

Now seek some matrix $[A]$ that satisfies

$$\begin{Bmatrix} \psi_1(\xi) \\ \psi_2(\xi) \\ \psi_3(\xi) \\ \psi_4(\xi) \end{Bmatrix}^T [A] = \frac{d}{dx} \begin{Bmatrix} \psi_1(\xi) \\ \psi_2(\xi) \\ \psi_3(\xi) \\ \psi_4(\xi) \end{Bmatrix}^T \implies \begin{Bmatrix} \psi_1(\xi) \\ \psi_2(\xi) \\ \psi_3(\xi) \\ \psi_4(\xi) \end{Bmatrix}^T [A] - \frac{d}{dx} \begin{Bmatrix} \psi_1(\xi) \\ \psi_2(\xi) \\ \psi_3(\xi) \\ \psi_4(\xi) \end{Bmatrix}^T = 0 \tag{3.71}$$

Substitute Equations (3.69) and (3.70) into (3.71).

$$\{b\}^T [N]^T [A] - \{b\}^T [dN]^T = \{b\}^T \left([N]^T [A] - [dN]^T \right) = 0 \tag{3.72}$$

Since the finite element basis functions are linearly independent and the matrix $[N]$ is invertible and well-conditioned,

$$[A] = [N]^{-T} [dN]^T = \frac{1}{l_e^2} \begin{bmatrix} 0 & l_e^2 & 0 & 0 \\ -6 & -4l_e & 6 & -2l_e \\ 0 & 0 & 0 & l_e^2 \\ 6 & 2l_e & -6 & 4l_e \end{bmatrix}, \tag{3.73}$$

and Equation (3.68) can be rewritten

$$\begin{Bmatrix} \psi_1(\xi) \\ \psi_2(\xi) \\ \psi_3(\xi) \\ \psi_4(\xi) \end{Bmatrix}^T \left(\begin{Bmatrix} q_{z(i)} \\ q'_{z(i)} \\ q_{z(i+1)} \\ q'_{z(i+1)} \end{Bmatrix} - Q_{13} [A] \begin{Bmatrix} U_i \\ U'_i \\ U_{i+1} \\ U'_{i+1} \end{Bmatrix} - Q_{33} \begin{Bmatrix} R_i \\ R'_i \\ R_{i+1} \\ R'_{i+1} \end{Bmatrix} \right) = 0, \tag{3.74}$$

where the subscript $(n+1)$ has been dropped from the DOFs and the superscript n has been dropped from the material constants for clarity. It should be understood that the DOFs in Equation (3.74) are on the top surface of the sandwich and the material properties belong to the top layer. The bracketed term in Equation (3.74) yields the following four constraint equations between degrees of freedom on the element:

$$\begin{aligned}
R_i &= \frac{q_{z(i)}}{Q_{33}} - \frac{Q_{13}}{Q_{33}} U_i' \\
R_i' &= \frac{q_{z(i)}'}{Q_{33}} + \frac{Q_{13}}{Q_{33}} \left(\frac{6}{l_e^2} U_i + \frac{4}{l_e} U_i' - \frac{6}{l_e^2} U_{i+1} + \frac{2}{l_e} U_{i+1}' \right) \\
R_{i+1} &= \frac{q_{z(i+1)}}{Q_{33}} - \frac{Q_{13}}{Q_{33}} U_{i+1}' \\
R_{i+1}' &= \frac{q_{z(i+1)}'}{Q_{33}} + \frac{Q_{13}}{Q_{33}} \left(-\frac{6}{l_e^2} U_i - \frac{2}{l_e} U_i' + \frac{6}{l_e^2} U_{i+1} - \frac{4}{l_e} U_{i+1}' \right)
\end{aligned} \tag{3.75}$$

Similar steps for an external shear traction yields

$$\begin{Bmatrix} q_{zx(i)} \\ q_{zx(i)}' \\ q_{zx(i+1)} \\ q_{zx(i+1)}' \end{Bmatrix} - Q_{55} \left([A] \begin{Bmatrix} W_i \\ W_i' \\ W_{i+1} \\ W_{i+1}' \end{Bmatrix} - \begin{Bmatrix} S_i \\ S_i' \\ S_{i+1} \\ S_{i+1}' \end{Bmatrix} \right) = 0 \tag{3.76}$$

and the four constraint equations

$$\begin{aligned}
S_i &= \frac{q_{zx(i)}}{Q_{55}} - W_i' \\
S_i' &= \frac{q_{zx(i)}'}{Q_{55}} + \frac{6}{l_e^2} W_i + \frac{4}{l_e} W_i' - \frac{6}{l_e^2} W_{i+1} + \frac{2}{l_e} W_{i+1}' \\
S_{i+1} &= \frac{q_{zx(i+1)}}{Q_{55}} - W_{i+1}' \\
S_{i+1}' &= \frac{q_{zx(i+1)}'}{Q_{55}} - \frac{6}{l_e^2} W_i - \frac{2}{l_e} W_i' + \frac{6}{l_e^2} W_{i+1} - \frac{4}{l_e} W_{i+1}'
\end{aligned} \tag{3.77}$$

The first and third constraint relationships in Equations (3.75) and (3.77) allow the DOFs R_i, R_{i+1}, S_i, and S_{i+1} to be related to the external traction and displacements at just the corresponding nodes. However, the second and fourth constraint equation are more difficult because they depend on values at *both* surface nodes. Thus, the constraint equations are not independent from element to element along the surface. The finite element code solves this problem by assembling all the constraint equations and determining partitions of dependent and independent DOFs through linear

algebra. For example, include Equation (3.73) and rewrite the bracketed term in Equation (3.74) as

$$Q_{13}\begin{bmatrix} 0 & 1 & 0 & 0 \\ \frac{-6}{l_e^2} & \frac{-4}{l_e} & \frac{6}{l_e^2} & \frac{-2}{l_e} \\ 0 & 0 & 0 & 1 \\ \frac{6}{l_e^2} & \frac{2}{l_e} & \frac{-6}{l_e^2} & \frac{4}{l_e} \end{bmatrix}\begin{Bmatrix} U_i \\ U_i' \\ U_{i+1} \\ U_{i+1}' \end{Bmatrix} + Q_{33}\begin{Bmatrix} R_i \\ R_i' \\ R_{i+1} \\ R_{i+1}' \end{Bmatrix} = \begin{Bmatrix} q_{z(i)} \\ q_{z(i)}' \\ q_{z(i+1)} \\ q_{z(i+1)}' \end{Bmatrix} \tag{3.78}$$

or more compactly,

$$\begin{bmatrix} 0 & Q_{13} & Q_{33} & 0 & 0 & 0 & 0 & 0 \\ \frac{-6}{l_e^2}Q_{13} & \frac{-4}{l_e}Q_{13} & 0 & Q_{33} & \frac{6}{l_e^2}Q_{13} & \frac{-2}{l_e}Q_{13} & 0 & 0 \\ 0 & 0 & 0 & 0 & 0 & Q_{13} & Q_{33} & 0 \\ \frac{6}{l_e^2}Q_{13} & \frac{2}{l_e}Q_{13} & 0 & 0 & \frac{-6}{l_e^2}Q_{13} & \frac{4}{l_e}Q_{13} & 0 & Q_{33} \end{bmatrix}\begin{Bmatrix} U_i \\ U_i' \\ R_i \\ R_i' \\ U_{i+1} \\ U_{i+1}' \\ R_{i+1} \\ R_{i+1}' \end{Bmatrix} = \begin{Bmatrix} q_{z(i)} \\ q_{z(i)}' \\ q_{z(i+1)} \\ q_{z(i+1)}' \end{Bmatrix} \tag{3.79}$$

The analogous constraints from Equation (3.76) are

$$\begin{bmatrix} 0 & Q_{55} & Q_{55} & 0 & 0 & 0 & 0 & 0 \\ \frac{-6}{l_e^2}Q_{55} & \frac{-4}{l_e}Q_{55} & 0 & Q_{55} & \frac{6}{l_e^2}Q_{55} & \frac{-2}{l_e}Q_{55} & 0 & 0 \\ 0 & 0 & 0 & 0 & 0 & Q_{55} & Q_{55} & 0 \\ \frac{6}{l_e^2}Q_{55} & \frac{2}{l_e}Q_{55} & 0 & 0 & \frac{-6}{l_e^2}Q_{55} & \frac{4}{l_e}Q_{55} & 0 & Q_{55} \end{bmatrix}\begin{Bmatrix} W_i \\ W_i' \\ S_i \\ S_i' \\ W_{i+1} \\ W_{i+1}' \\ S_{i+1} \\ S_{i+1}' \end{Bmatrix} = \begin{Bmatrix} q_{zx(i)} \\ q_{zx(i)}' \\ q_{zx(i+1)} \\ q_{zx(i+1)}' \end{Bmatrix} \tag{3.80}$$

Equations (3.79) and (3.80) can be combined into a constraint *element* via

$$[C^e]\{u_b\} = \{q_{ext}^e\}, \tag{3.81}$$

where $[C^e]$ is the element constraint matrix, $\{u_b\}$ are the 16 DOFs on the element surface, and $\{q_{ext}^e\}$ is a vector of the external tractions and their derivatives. Transpose both sides for display

as

$$\begin{Bmatrix} U_i \\ U_i' \\ W_i \\ W_i' \\ R_i \\ R_i' \\ S_i \\ S_i' \\ U_{i+1} \\ U_{i+1}' \\ W_{i+1} \\ W_{i+1}' \\ R_{i+1} \\ R_{i+1}' \\ S_{i+1} \\ S_{i+1}' \end{Bmatrix}^T \begin{bmatrix} 0 & \frac{-6}{l_e^2}Q_{13} & 0 & 0 & 0 & \frac{6}{l_e^2}Q_{13} & 0 & 0 \\ Q_{13} & \frac{-4}{l_e}Q_{13} & 0 & 0 & 0 & \frac{2}{l_e}Q_{13} & 0 & 0 \\ 0 & 0 & 0 & \frac{-6}{l_e^2}Q_{55} & 0 & 0 & 0 & \frac{6}{l_e^2}Q_{55} \\ 0 & 0 & Q_{55} & \frac{-4}{l_e}Q_{55} & 0 & 0 & 0 & \frac{2}{l_e}Q_{55} \\ Q_{33} & 0 & 0 & 0 & 0 & 0 & 0 & 0 \\ 0 & Q_{33} & 0 & 0 & 0 & 0 & 0 & 0 \\ 0 & 0 & Q_{55} & 0 & 0 & 0 & 0 & 0 \\ 0 & 0 & 0 & Q_{55} & 0 & 0 & 0 & 0 \\ 0 & \frac{6}{l_e^2}Q_{13} & 0 & 0 & 0 & \frac{-6}{l_e^2}Q_{13} & 0 & 0 \\ 0 & \frac{-2}{l_e}Q_{13} & 0 & 0 & Q_{13} & \frac{4}{l_e}Q_{13} & 0 & 0 \\ 0 & 0 & 0 & \frac{6}{l_e^2}Q_{55} & 0 & 0 & 0 & \frac{-6}{l_e^2}Q_{55} \\ 0 & 0 & 0 & \frac{-2}{l_e}Q_{55} & 0 & 0 & Q_{55} & \frac{4}{l_e}Q_{55} \\ 0 & 0 & 0 & 0 & Q_{33} & 0 & 0 & 0 \\ 0 & 0 & 0 & 0 & 0 & Q_{33} & 0 & 0 \\ 0 & 0 & 0 & 0 & 0 & 0 & Q_{55} & 0 \\ 0 & 0 & 0 & 0 & 0 & 0 & 0 & Q_{55} \end{bmatrix} = \begin{Bmatrix} q_{z(i)} \\ q'_{z(i)} \\ q_{zx(i)} \\ q'_{zx(i)} \\ q_{z(i+1)} \\ q'_{z(i+1)} \\ q_{zx(i+1)} \\ q'_{zx(i+1)} \end{Bmatrix}^T \tag{3.82}$$

Equation (3.81) can be evaluated for all elements on the boundary and assembled into a global set of constraint equations. For computational purposes, one can 1) take advantage of the fact that constraint for shear and normal tractions address separate sets of boundary degrees of freedom, and 2) realize that the constraint equations for the upper surface are independent of those for the lower surface. The global set of constraint equations is underdetermined and can be partitioned as

$$\begin{bmatrix} C_i & C_d \end{bmatrix} \begin{Bmatrix} u_{bi} \\ u_{bd} \end{Bmatrix} = \{q_{ext}\} \tag{3.83}$$

where $[C_d]$ is a square, full-rank matrix with dimension equal to the number of dependent DOFs created by the constraint equations. Subscripts i and d have been added to identify independent and dependent partitions. Performing the multiplications,

$$[C_i]\{u_{bi}\} + [C_d]\{u_{bi}\} = \{q_{ext}\} \Longrightarrow \{u_{bi}\} = -[C_d]^{-1}[C_i]\{u_{bi}\} + [C_d]^{-1}\{q_{ext}\} \tag{3.84}$$

Finally, the end result is a coordinate transformation that enforces tractions at the upper and lower surfaces by reducing the number of DOFs in the problem from the full set of physical DOFs, u, to

a minimal set, u_m.

$$\begin{Bmatrix} u_f \\ u_{bi} \\ u_{bd} \end{Bmatrix} = \begin{bmatrix} I_f & \mathbf{0} \\ \mathbf{0} & I_{bi} \\ \mathbf{0} & -C_d^{-1}C_i \end{bmatrix} \begin{Bmatrix} u_f \\ u_{bi} \end{Bmatrix} + \begin{Bmatrix} \mathbf{0} \\ \mathbf{0} \\ C_d^{-1}q_{ext} \end{Bmatrix} \tag{3.85}$$

or

$$\{u\} = [E_{pm}]\{u_m\} + \{q_p\} \tag{3.86}$$

The final equations of motion result from substituting Equation (3.86) and its variation ($\{\delta u\} = [E_{pm}]\{\delta u_m\}$) into Equation (3.60) to get

$$\{\delta u_m\}^T \left(\left[\hat{M}\right]\{\ddot{u}_m\} + \left[\hat{K}\right]\{u_m\} - \left\{\hat{f}\right\} \right) = 0 \tag{3.87}$$

and

$$\left[\hat{M}\right]\{\ddot{u}_m\} + \left[\hat{K}\right]\{u_m\} = \left\{\hat{f}\right\} \tag{3.88}$$

where

$$\begin{aligned} \left[\hat{M}\right] &= [E_{pm}]^T [M] [E_{pm}] \\ \left[\hat{K}\right] &= [E_{pm}]^T [K] [E_{pm}] \\ \left\{\hat{f}\right\} &= [E_{pm}]^T \{f\} - [E_{pm}]^T [M] \{\ddot{q}_p\} - [E_{pm}]^T [K] \{q_p\} \end{aligned}$$

The presence of the external traction $\{q_p\}$ in the load vector $\hat{f}$ amounts to enforcing time-dependent displacements at certain degrees of freedom. The above derivation presents a new formulation for traction continuity following Lee and Liu's original formulation. It extends Lee and Liu's earlier results in that it is formulated as a 2-D element and can represent any arbitrary partial-coverage configuration.

3.4 Euler-Bernoulli Beams

3.4.1 Strain Energy

The Euler-Bernoulli beam is used widely in engineering as a good model for beams that are relatively long compared to their thickness. Their kinematics are an integral part of the MM theory,

and as such they are reviewed here. A fundamental assumption is that a material line initially perpendicular to the neutral axis of the beam remains perpendicular after deformation, as shown by lines A–B and A′–B′ in Figure 3.4. The kinematics are defined here with respect to a reference

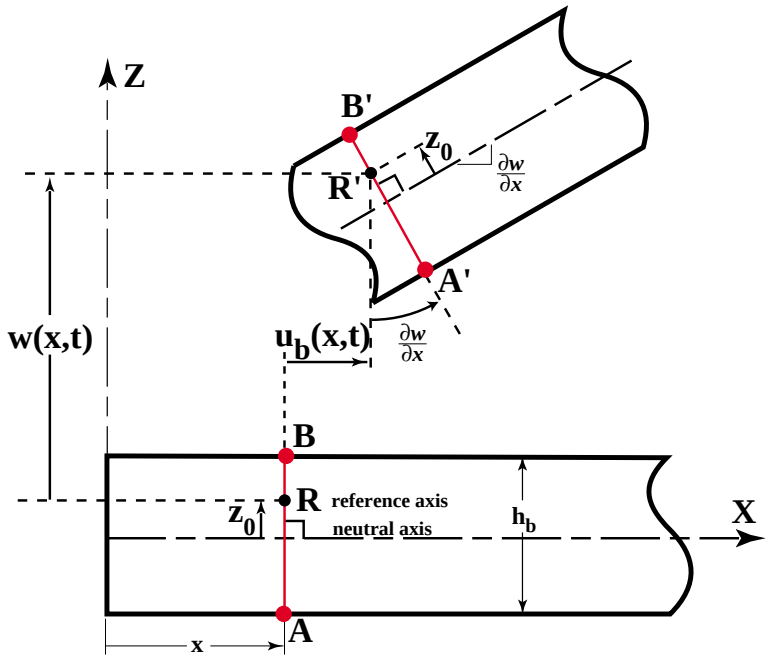

Figure 3.4: Displacement field for an Euler-Bernoulli beam with offset reference axis

axis, which in finite element analysis is a convenient way of moving the node points from the neutral axis to the surface of the beam for attachment with other elements. Most authors assume plane stress with respect to the out-of-plane y direction. The displacement field within the beam can be described by

$$u(x,z) = u_b(x) - (z - z_o)\,\frac{\partial w(x)}{\partial x} \tag{3.89a}$$

$$w(x,z) = w(x)\,, \tag{3.89b}$$

where u_b is the axial displacement measured at the reference axis and the coordinate z is always measured from the neutral axis of the beam. Dropping the function indications, the linear strains are

$$\epsilon_x = \frac{\partial u}{\partial x} = \frac{\partial u_b}{\partial x} - (z - z_o)\,\frac{\partial^2 w}{\partial x^2} \tag{3.90a}$$

$$\epsilon_z = \frac{\partial w}{\partial z} = 0 \tag{3.90b}$$

$$\gamma_{zx} = 2\epsilon_{zx} = \frac{\partial u}{\partial z} + \frac{\partial w}{\partial x} = 0 \tag{3.90c}$$

Using the assumption of plane stress in the y coordinate direction, the constitutive relationship for a linear isotropic elastic material is

$$\begin{Bmatrix} \sigma_x \\ \sigma_z \\ \tau_{zx} \end{Bmatrix} = \frac{E}{1-\nu^2} \begin{bmatrix} 1 & \nu & 0 \\ \nu & 1 & 0 \\ 0 & 0 & \frac{G(1-\nu^2)}{E} \end{bmatrix} \begin{Bmatrix} \epsilon_x \\ \epsilon_z \\ \gamma_{zx} \end{Bmatrix} \tag{3.91}$$

where E is Young's modulus, G is the shear modulus, and ν is Poisson's ratio. Immediately there is a problem if the zero transverse normal strains in Equation (3.90b) is taken too literally. From Equation (3.8), the strain energy density of a linear isotropic elastic material in terms of the six independent components of stress and strain is

$$W = \frac{1}{2}\sigma^T \epsilon \tag{3.92}$$

Substituting the strains from Equations (3.90) into Equations (3.91) and (3.92) yields

$$\begin{Bmatrix} \sigma_x \\ \sigma_z \\ \tau_{zx} \end{Bmatrix} = \begin{Bmatrix} \frac{E\epsilon_x}{1-\nu^2} \\ \frac{\nu E\epsilon_x}{1-\nu^2} \\ 0 \end{Bmatrix} \Longrightarrow W = \frac{1}{2} \begin{Bmatrix} \frac{E\epsilon_x}{1-\nu^2} \\ \frac{\nu E\epsilon_x}{1-\nu^2} \\ 0 \end{Bmatrix}^T \begin{Bmatrix} \epsilon_x \\ 0 \\ 0 \end{Bmatrix} = \frac{1}{2}\left(\frac{E}{1-\nu^2}\right)\epsilon_x^2, \tag{3.93}$$

where most any book on mechanics will give the strain energy density of an Euler beam as

$$W = \frac{1}{2}\sigma_x \epsilon_x = \frac{1}{2} E \epsilon_x^2 \tag{3.94}$$

Strictly speaking, imposition of zero transverse strain is in effect a constraint that stiffens the system. Another problem is the nonzero transverse normal stress (σ_z) in the first of Equations (3.93) in the absence of any direct stresses applied at the surfaces. Shames [90] points out that these problems are reconciled by using a constitutive law with Poisson's ratio equal to zero in what he refers to as a "*technical* or *engineering theory of beams.*" Another way to arrive at this strain energy is to assume the outer surfaces of the beam to be traction free, in which case the transverse

normal strain ϵ_z would be $-\nu\epsilon_x$, not zero. Substituting $\epsilon_z = -\nu\epsilon_x$ and $\gamma_{zx} = 0$ into Equations (3.91) yields

$$\begin{Bmatrix} \sigma_x \\ \sigma_z \\ \tau_{zx} \end{Bmatrix} = \frac{E}{1-\nu^2} \begin{bmatrix} 1 & \nu & 0 \\ \nu & 1 & 0 \\ 0 & 0 & \frac{G\left(1-\nu^2\right)}{E} \end{bmatrix} \begin{Bmatrix} \epsilon_x \\ -\nu\epsilon_x \\ 0 \end{Bmatrix} = \begin{Bmatrix} E\epsilon_x \\ (\nu-\nu)\,\epsilon_x \\ 0 \end{Bmatrix} = \begin{Bmatrix} E\epsilon_x \\ 0 \\ 0 \end{Bmatrix} \tag{3.95}$$

Alternately using the technical theory for beams with $\nu = 0$,

$$\begin{Bmatrix} \sigma_x \\ \sigma_z \\ \tau_{zx} \end{Bmatrix} = \begin{bmatrix} E & 0 & 0 \\ 0 & E & 0 \\ 0 & 0 & G \end{bmatrix} \begin{Bmatrix} \epsilon_x \\ 0 \\ 0 \end{Bmatrix} = \begin{Bmatrix} E\epsilon_x \\ 0 \\ 0 \end{Bmatrix} = \left[\hat{Q}\right] \{\epsilon\}, \tag{3.96}$$

where the reduced stiffness matrix $\left[\hat{Q}\right]$ includes the assumption that Poisson's ratio is zero. From Equation (3.92), the strain energy density is thus

$$W = \frac{1}{2} \begin{Bmatrix} E\epsilon_x \\ 0 \\ 0 \end{Bmatrix}^T \begin{Bmatrix} \epsilon_x \\ 0 \\ 0 \end{Bmatrix} = \frac{1}{2} E\epsilon_x^2, \tag{3.97}$$

This is a trivial point here, but it helps understand the effect of the MM assumptions on the VEM core.

The potential energy for the Euler beam comes from substituting Equation (3.90a) into Equation (3.94) and integrating over the volume of the beam.

$$\begin{aligned} U &= \int_\Omega W d\Omega = \frac{1}{2} \int_\Omega E\epsilon_x^2 d\Omega \\ &= \frac{1}{2} \int_0^L \int_{\frac{-h_b}{2}}^{\frac{h_b}{2}} E \left[\left(\frac{\partial u_b}{\partial x} \right)^2 - 2\left(z - z_o\right) \frac{\partial u_b}{\partial x} \frac{\partial^2 w}{\partial x^2} + \left(z - z_o\right)^2 \left(\frac{\partial^2 w}{\partial x^2} \right)^2 \right] dz\, dx \\ &= \frac{1}{2} \int_0^L E \left[h_b \left(\frac{\partial u_b}{\partial x} \right)^2 + 2 z_o h_b \frac{\partial u_b}{\partial x} \frac{\partial^2 w}{\partial x^2} + I_o \left(\frac{\partial^2 w}{\partial x^2} \right)^2 \right] dx \end{aligned} \tag{3.98}$$

where $A = h_b =$ cross-sectional area for unit width and $I_o = \bar{I} + A z_o^2$ is the moment of inertia about the offset axis via the parallel axis theorem. Equation (3.98) shows that the offset z_o introduces

coupling between the membrane and bending deformation of the beam. Setting the offset to zero yields the familiar expression for potential energy of an Euler-Bernoulli beam.

$$U = \frac{1}{2}\int_0^L EA\left(\frac{\partial u_b}{\partial x}\right)^2 dx + \frac{1}{2}\int_0^L EI\left(\frac{\partial^2 w}{\partial x^2}\right)^2 dx \tag{3.99}$$

for a unit-width beam of length L.

3.4.2 Kinetic Energy

The kinetic energy of the beam comes from substituting Equations (3.89a) and (3.89b) into Equation (3.2):

$$\begin{aligned} T &= \frac{1}{2}\int_\Omega \rho\left(\dot{u}^2 + \dot{w}^2\right) d\Omega \\ &= \frac{1}{2}\int_0^L \int_{\frac{-h_b}{2}}^{\frac{h_b}{2}} \rho\left[\left(\frac{\partial u_b}{\partial t}\right)^2 - 2\left(z - z_o\right)\frac{\partial u_b}{\partial t}\frac{\partial^2 w}{\partial x \partial t} + \left(z - z_o\right)^2\left(\frac{\partial^2 w}{\partial x \partial t}\right)^2 + \left(\frac{\partial w}{\partial t}\right)^2\right] dz\, dx \\ &= \frac{1}{2}\int_0^L \rho\left[h_b\left(\frac{\partial u_b}{\partial t}\right)^2 + 2h_b z_o \frac{\partial u_b}{\partial t}\frac{\partial^2 w}{\partial x \partial t} + I_o\left(\frac{\partial^2 w}{\partial x \partial t}\right)^2 + h_b\left(\frac{\partial w}{\partial t}\right)^2\right] dx \end{aligned} \tag{3.100}$$

where $I_o = \bar{I} + Az_o^2$ as in Equation (3.98). Setting the beam offset to zero yields the more standard expression

$$T = \frac{1}{2}\int_0^L \left[\rho A\left(\frac{\partial u_b}{\partial t}\right)^2 + \rho I\left(\frac{\partial^2 w}{\partial x \partial t}\right)^2 + \rho A\left(\frac{\partial w}{\partial t}\right)^2\right] dx \tag{3.101}$$

for the unit-width beam. Shames [90] points out that product of the rotatary inertia and square of the angular velocity $\left(I_o\left(\frac{\partial^2 w}{\partial x \partial t}\right)^2\right)$ is often neglected for low-order dynamics of thin beams.

3.4.3 Finite Element Implementation

A finite element discretization of an Euler-Bernoulli beam including offset and axial deformations is outlined in this section. As a convenience, map an element of the Euler beam from the original

domain ($0 \leq x \leq l_e$ and $\frac{-h_e}{2} \leq z \leq \frac{h_e}{2}$) to a master element ($-1 \leq \zeta \leq 1$ and $-1 \leq \xi \leq 1$) by using

$$\xi = \frac{2}{l_e}(x - x_1) - 1 \tag{3.102}$$

$$\zeta = \frac{2}{h_e} z \tag{3.103}$$

$$\tag{3.104}$$

as shown in Figure 3.5. Also defined on the figure are the element degrees of freedom (DOF) in

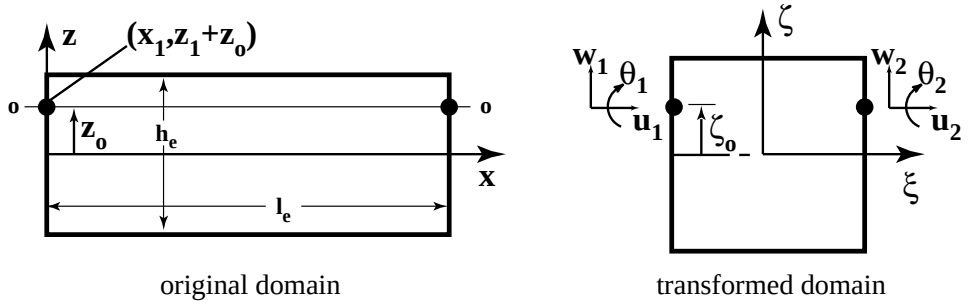

Figure 3.5: Euler beam with degrees of freedom

the vector $\{a\}$, where

$$\{a\} = \begin{Bmatrix} u_1 & w_1 & \theta_1 & u_2 & w_2 & \theta_2 \end{Bmatrix}^T, \tag{3.105}$$

where time-dependence is implied for all the DOFs. This is a 1-D element, so a mapping of the z coordinate is not necessary. However, to be consistent, map the z coordinate via $\zeta = \frac{2}{h_e} z$ and note that the offset ζ_o is now defined as $-1 \leq \zeta_o \leq 1$. Doing this, Equation (3.89a) becomes

$$u(x, \zeta) = u_b(x) - (\zeta - \zeta_o) \frac{h_b}{2} \frac{\partial w(x)}{\partial x} \tag{3.106}$$

The order of the derivatives dictates that the axial and transverse displacements can be discretized with Lagrange and Hermite cubic shape functions, respectively. Over a single element, write

$$u_b^e(x) = u_1 \, \phi_1(\xi) + u_2 \, \phi_2(\xi) \tag{3.107}$$

$$w^e(x) = w_1 \, \psi_1(\xi) + \theta_1 \, \psi_2(\xi) + w_2 \, \psi_3(\xi) + \theta_2 \, \psi_4(\xi) \tag{3.108}$$

where

$$\begin{aligned} \phi_1(\xi) &= \frac{1}{2}(1 - \xi) \\ \phi_2(\xi) &= \frac{1}{2}(1 + \xi) \end{aligned} \tag{3.109}$$

and the $\{\psi(\xi)\}$ were defined in Equation (3.49). Now the displacement field of Equation (3.106) can be written over an element as

$$\begin{aligned} u_b^e(\xi,\zeta) = u_1\,\phi_1(\xi) + & u_2\,\phi_2(\xi) \\ -(\zeta-\zeta_o)\,\frac{h_e}{2}\frac{2}{l_e}\Big[& w_1\frac{\partial\psi_1(\xi)}{\partial\xi} + \theta_1\frac{\partial\psi_2(\xi)}{\partial\xi} + \\ & w_2\frac{\partial\psi_3(\xi)}{\partial\xi} + \theta_2\frac{\partial\psi_4(\xi)}{\partial\xi}\Big] \end{aligned} \tag{3.110}$$

where $\frac{\partial x}{\partial\xi} = \frac{l_e}{2}$ is included to allow derivatives of the shape functions with respect to the transformed coordinate ξ. The axial displacement of Equation (3.110) and transverse displacement of Equation (3.108) can be written compactly as

$$u_b^e(\xi,\zeta) = \{N_u(\xi,\zeta)\}^T\,\{a\} \tag{3.111}$$

$$w_b^e(\xi,\zeta) = \{N_w(\xi,\zeta)\}^T\,\{a\} \tag{3.112}$$

where

$$\{N_u(\xi,\zeta)\} = \begin{Bmatrix} \phi_1(\xi) \\ (\zeta_o-\zeta)\,\frac{h_e}{l_e}\psi_1'(\xi) \\ (\zeta_o-\zeta)\,\frac{h_e}{l_e}\psi_2'(\xi) \\ \phi_2(\xi) \\ (\zeta_o-\zeta)\,\frac{h_e}{l_e}\psi_3'(\xi) \\ (\zeta_o-\zeta)\,\frac{h_e}{l_e}\psi_4'(\xi) \end{Bmatrix}, \qquad \{N_w(\xi)\} = \begin{Bmatrix} 0 \\ \psi_1(\xi) \\ \psi_2(\xi) \\ 0 \\ \psi_3(\xi) \\ \psi_4(\xi) \end{Bmatrix}, \tag{3.113}$$

and $()'$ denotes differentiation with respect to the transformed coordinate ξ. Dropping the function indications, the strains in Equation (3.90) can be written

$$\{\epsilon\} = \begin{Bmatrix} \epsilon_x \\ \epsilon_z \\ \gamma_{zx} \end{Bmatrix} = \begin{bmatrix} \frac{2}{l_e}\frac{\partial\{N_u\}^T}{\partial\xi} \\ \mathbf{0} \\ \frac{2}{h_e}\frac{\partial\{N_u\}^T}{\partial\zeta} + \frac{2}{l_e}\frac{\partial\{N_w\}^T}{\partial\xi} \end{bmatrix} \{a\} = [B]\,\{a\} \tag{3.114}$$

where $[B(\xi,\zeta)]$ is the strain-displacement matrix. Using the constitutive relationship from Equation (3.96) $\{\sigma\} = \left[\hat{Q}\right]\{\epsilon\} = \left[\hat{Q}\right][B(\xi,\zeta)]\,\{a\}$, the strain energy comes from integrating Equation (3.92) over the domain of an element.

$$U^e = \frac{1}{2}\int_{\Omega^e} \{\epsilon\}^T\,\{\sigma\}\,d\Omega^e = \frac{1}{2}\,\{a\}^T\,[k^e]\,\{a\} \tag{3.115}$$

The element stiffness matrix $[k^e]$ is

$$[k^e] = \int_{-1}^{1}\int_{-1}^{1} [B]^T \left[\hat{Q}\right] [B] \; \mathcal{J} \, d\xi \, d\zeta, \tag{3.116}$$

similar to Equation (3.27).

The kinetic energy over an element is found by substituting time derivatives of the discretized displacements of Equations (3.111) and (3.112) into Equation (3.2) and integrating over the domain of an element. Dropping the functional relationships and indicating differentiation with respect to time by $\dot{(\,)}$, the kinetic energy is

$$\begin{aligned} T &= \frac{1}{2}\int_{\Omega^e} \rho \left[\left(\{N_u\}^T \{\dot{a}\} \right)^T \left(\{N_u\}^T \{\dot{a}\} \right) + \left(\{N_w\}^T \{\dot{a}\} \right)^T \left(\{N_w\}^T \{\dot{a}\} \right) \right] d\Omega^e \\ &= \frac{1}{2} \{\dot{a}\}^T [m^e] \{\dot{a}\} \end{aligned} \tag{3.117}$$

where the element mass matrix is

$$[m^e] = \int_{-1}^{1}\int_{-1}^{1} \left[\{N_u\} \{N_u\}^T + \{N_w\} \{N_w\}^T \right] \mathcal{J} \, d\xi \, d\zeta \tag{3.118}$$

and ρ is the mass density.

3.5 Three-Layer Sandwich Beam With Mead and Markus Assumptions

The displacements dictated by the MM assumptions are shown in Figure 3.6. A fundamental assumption of the MM approach is that the material line B–C in the VEM remains straight after deformation, as shown by line B′–C′ in Figure 3.6. This in effect defines the axial deformation of any material position x inside the core as a linear interpolation of the displacements u_b' and u_c' on the surfaces of the facesheets (the base and constraining layers). The other important assumption is that all layers share a common transverse displacement. The strain energy for each layer in the sandwich is developed in the following sections.

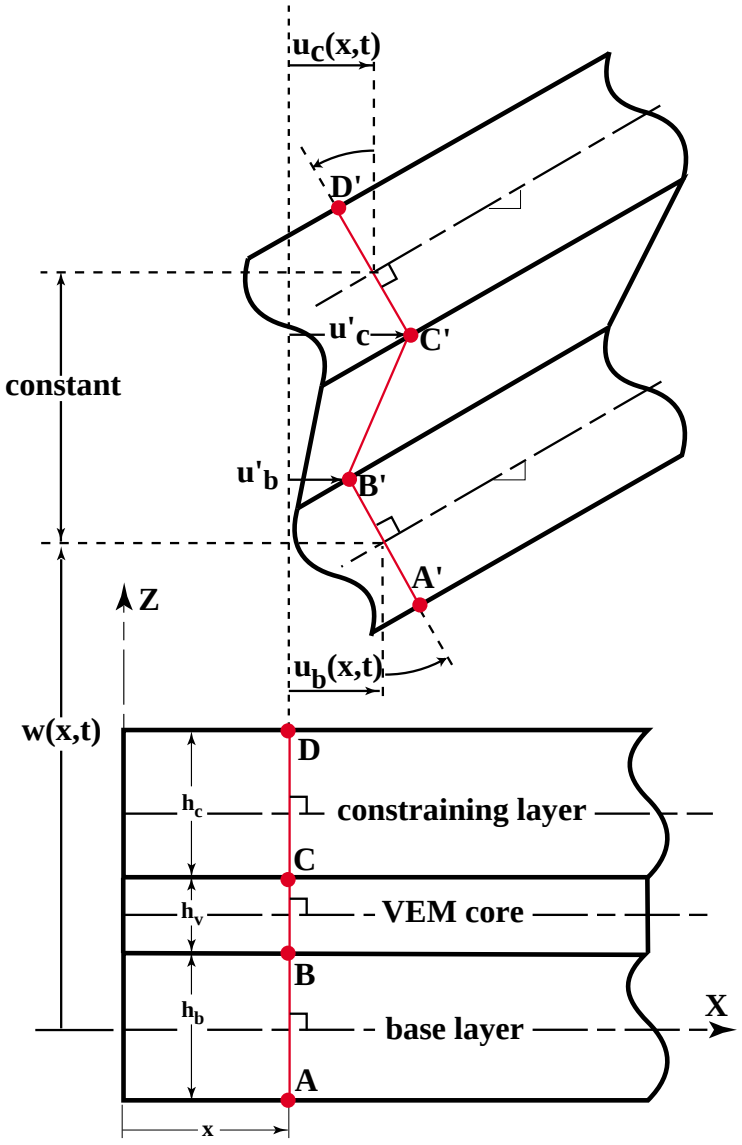

Figure 3.6: Displacement fields for Mead and Markus assumptions

3.5.1 Energy in the Facesheets

Strain Energy

The facesheets are Euler-Bernoulli beams with the nodes offset to the surfaces where the VEM attaches, though it is more common in the literature [62, 17] to assume the offset zero when calculating the energy. Inclusion of an offset is a convenience, not a necessity, and the total strain energy in the sandwich is not affected by the offset as long as the displacements at the surfaces of the facesheets are used in computing the strain energy in the core. From Equation (3.98), the strain energies in the base and constraining layers with the offsets set to zero are

$$U_b = \frac{1}{2}\int_0^L \left[E_b h_b \left(\frac{\partial u_b}{\partial x}\right)^2 + E_b I_b \left(\frac{\partial^2 w}{\partial x^2}\right)^2 \right] dx \tag{3.119}$$

$$U_c = \frac{1}{2}\int_0^L \left[E_c h_c \left(\frac{\partial u_c}{\partial x}\right)^2 + E_c I_c \left(\frac{\partial^2 w}{\partial x^2}\right)^2 \right] dx \tag{3.120}$$

Kinetic Energy

The kinetic energy of the facesheets follows directly from Equation (3.101).

$$T_b = \frac{1}{2}\int_0^L \left[\rho_b A_b \left(\frac{\partial u_b}{\partial t}\right)^2 + \rho_b I_b \left(\frac{\partial^2 w}{\partial x \partial t}\right)^2 + \rho_b A_b \left(\frac{\partial w}{\partial t}\right)^2 \right] dx \tag{3.121}$$

$$T_c = \frac{1}{2}\int_0^L \left[\rho_c A_c \left(\frac{\partial u_c}{\partial t}\right)^2 + \rho_c I_c \left(\frac{\partial^2 w}{\partial x \partial t}\right)^2 + \rho_c A_c \left(\frac{\partial w}{\partial t}\right)^2 \right] dx \tag{3.122}$$

3.5.2 Energy in the VEM Core

Strain Energy

The strain energy in the VEM core under the Mead and Markus assumptions is straightforward. Considering the assumption (MM) that a material line B–C in the VEM remains straight after deformation, as shown by line B′–C′ in Figure 3.6, the axial deformation of any material position

x inside the core as a linear interpolation of the displacements u_b' and u_c', which are defined by

$$u_b' = u_b - \left(\frac{h_b}{2} - z_{ob}\right)\frac{\partial w}{\partial x} \tag{3.123}$$

$$u_c' = u_c + \left(\frac{h_c}{2} - z_{oc}\right)\frac{\partial w}{\partial x}, \tag{3.124}$$

where z_{ob} and z_{oc} are offsets for the base and constraining layers, respectively, as shown in Figure 3.4 The resulting displacement field within the VEM is thus

$$u_v(x,z) = \frac{1}{2}\left(u_c' + u_b'\right) + \frac{z}{h_v}\left(u_c' - u_b'\right) \tag{3.125a}$$

$$w_v(x,z) = w(x) \tag{3.125b}$$

The corresponding linear strains are

$$\epsilon_x = \frac{1}{2}\left(\frac{\partial u_c'}{\partial x} + \frac{\partial u_b'}{\partial x}\right) + \frac{z}{h_v}\left(\frac{\partial u_c'}{\partial x} - \frac{\partial u_b'}{\partial x}\right) \tag{3.126a}$$

$$\epsilon_z = \frac{\partial w_v}{\partial z} = 0 \tag{3.126b}$$

$$\begin{aligned}\gamma_{zx} = 2\epsilon_{zx} &= \frac{\partial w_v}{\partial x} + \frac{\partial u_v}{\partial z} = \frac{\partial w}{\partial x} + \frac{1}{h_v}\left(u_c' - u_b'\right) \\ &= \frac{\partial w}{\partial x} + \frac{1}{h_v}\left[u_c - u_b + \frac{\partial w}{\partial x}\left(\frac{h_b}{2} + \frac{h_c}{2} - z_{ob} - z_{oc}\right)\right] \\ &= \frac{u_c - u_b}{h_v} + \frac{d}{h_v}\frac{\partial w}{\partial x}\end{aligned} \tag{3.126c}$$

where $d = \left(\frac{h_b}{2} + h_v + \frac{h_c}{2} - z_{ob} - z_{oc}\right)$, the distance between the reference lines of the undeformed facesheets. The zero transverse normal strain of Equation (3.126b) results from the assumption that all layers have a common transverse displacement. Similar to the Euler-Bernoulli beam in Section 3.4.1, this is artificial in the sense that the facesheets will have relative transverse deformations due to nonzero transverse normal strains caused by Poisson's ratio and axial strains in the VEM core. Taken literally, Equation (3.126b) imposes an extra constraint through the thickness, and this violates the intention of the MM assumptions. As with the Euler-Bernoulli beam, this constraint is avoided by choosing the constitutive relationship of Equation (3.96). Doing so, however, eliminates the possibility of calculating any transverse normal strains, eigenstrains (thermal, piezoelectric), or

stresses, but these quantities are deemed unimportant by choice of the MM assumptions in the first place. The strain energy in the VEM core is found by substituting the strains in Equation (3.126) in to Equations (3.96) and (3.92) and integrating over the domain of the beam:

$$U_v = \frac{1}{2}\int_{\Omega} \left(E\epsilon_x^2 + G\gamma_{zx}^2 \right) d\Omega. \tag{3.127}$$

Substituting Equations (3.123)–(3.126) into this expressions yields the strain energy in terms of the chosen displacement coordinates. This is done by authors who use energy to develop the equations of motion but approach the solution using non-FEM approximation techniques [29, 53, 47].

Kinetic Energy

The kinetic energy is a straightforward substitution of the displacements of Equations (3.123)–(3.125) into Equation (3.2). The algebra is simple for the finite element discretization as will be shown in Section 3.5.3.

3.5.3 Finite Element Implementation

It is straightforward to define an eight-degree-of-freedom element that imposes the Mead and Markus assumptions [17]. Just like the Euler-Bernoulli beam in Section 3.4.3, there are six degrees of freedom for the base layer, but there are only two for the constraining layer since its transverse displacement and rotations are not independent of the base layer's. Figure 3.7 shows the degrees of freedom in the vector

$$\{a\} = \begin{Bmatrix} u_1 & w_1 & \theta_1 & u_4 & u_2 & w_2 & \theta_2 & u_3 \end{Bmatrix}^T \tag{3.128}$$

The displacement fields of the three layers are completely described by these eight degrees of freedom.

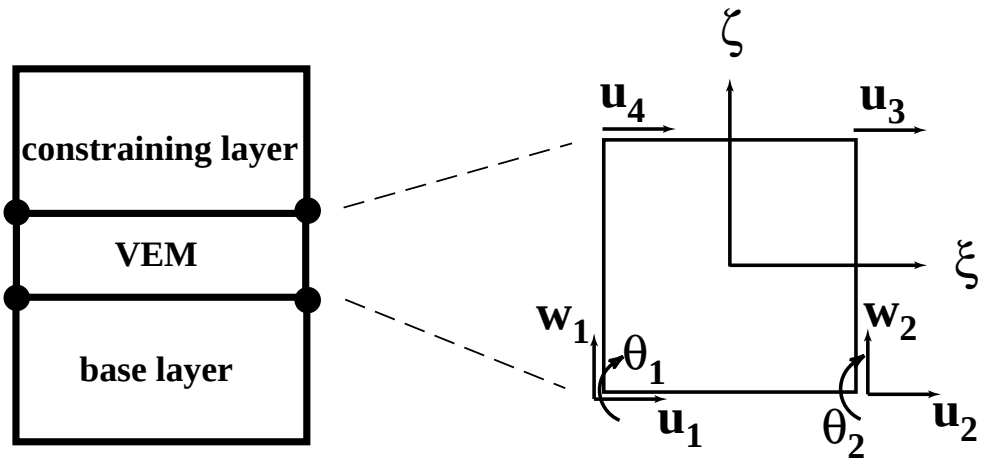

Figure 3.7: Degrees of freedom for the Mead and Markus model

Facesheets

The nodes are defined at the surfaces of the two facesheets, so similar to Equation (3.110) the displacement field in the core is

$$\begin{aligned} u_b^e(\xi,\zeta_b) &= u_1\,\phi_1(\xi) + u_2\,\phi_2(\xi) \\ &\quad - (\zeta_b - 1)\,\frac{h_b}{l_e}\left[w_1\frac{\partial\psi_1(\xi)}{\partial\xi} + \theta_1\frac{\partial\psi_2(\xi)}{\partial\xi}\right. \\ &\quad \left. + w_2\frac{\partial\psi_3(\xi)}{\partial\xi} + \theta_2\frac{\partial\psi_4(\xi)}{\partial\xi}\right], \end{aligned} \tag{3.129}$$

and the displacement field in the constraining layer is

$$\begin{aligned} u_c^e(\xi,\zeta_c) &= u_4\,\phi_1(\xi) + u_3\,\phi_2(\xi) \\ &\quad - (\zeta_c + 1)\,\frac{h_c}{l_e}\left[w_1\frac{\partial\psi_1(\xi)}{\partial\xi} + \theta_1\frac{\partial\psi_2(\xi)}{\partial\xi}\right. \\ &\quad \left. + w_2\frac{\partial\psi_3(\xi)}{\partial\xi} + \theta_2\frac{\partial\psi_4(\xi)}{\partial\xi}\right]. \end{aligned} \tag{3.130}$$

The strain energy in the base layer is developed from Equations (3.111)–(3.116) using an offset of $\zeta_o = +1$:

$$u_b^e = \{N_{ub}\}^T\{a\} \tag{3.131}$$

$$w^e = \{N_w\}^T\{a\} \tag{3.132}$$

where

$$\{N_{ub}\} = \begin{Bmatrix} \phi_1 \\ (1-\zeta_b)\frac{h_b}{l_e}\psi_1' \\ (1-\zeta_b)\frac{h_b}{l_e}\psi_2' \\ 0 \\ \phi_2 \\ (1-\zeta_b)\frac{h_b}{l_e}\psi_3' \\ (1-\zeta_b)\frac{h_b}{l_e}\psi_4' \\ 0 \end{Bmatrix} \quad \text{and} \quad \{N_w\} = \begin{Bmatrix} 0 \\ \psi_1 \\ \psi_2 \\ 0 \\ 0 \\ \psi_3 \\ \psi_4 \\ 0 \end{Bmatrix} \tag{3.133}$$

From here, the element stiffness matrix is obtained by replacing $\{N_u\}$ with $\{N_{ub}\}$ in Equations (3.114) and (3.116).

The strain energy in the constraining layer is similar to that of the base layer. Using an offset of $\zeta_o = -1$, the discretized displacement field is

$$u_c^e = \{N_{uc}\}^T \{a\} \tag{3.134}$$

where

$$\{N_{uc}\} = \begin{Bmatrix} 0 \\ -(1+\zeta_c)\frac{h_c}{l_e}\psi_1' \\ -(1+\zeta_c)\frac{h_c}{l_e}\psi_2' \\ \phi_1 \\ 0 \\ -(1+\zeta_c)\frac{h_c}{l_e}\psi_3' \\ -(1+\zeta_c)\frac{h_c}{l_e}\psi_4' \\ \phi_2 \end{Bmatrix} \tag{3.135}$$

Again, the element stiffness matrix comes from Equations (3.114) and (3.116) substituting $\{N_{uc}\}$ for $\{N_u\}$.

The kinetic energies for both layers using shape function vectors $\{N_{ub}\}$ and $\{N_{uc}\}$ follow directly from Equation (3.117). For the base layer, the element mass matrix is

$$[m_b^e] = \int_{-1}^{1}\int_{-1}^{1} \left[\{N_{ub}\}\{N_{ub}\}^T + \{N_w\}\{N_w\}^T\right] \mathcal{J}\, d\xi\, d\zeta_b, \tag{3.136}$$

and for the constraining layer the element mass matrix is

$$[m_c^e] = \int_{-1}^{1}\int_{-1}^{1} \left[\{N_{uc}\}\{N_{uc}\}^T + \{N_w\}\{N_w\}^T\right] \mathcal{J}\, d\xi\, d\zeta_c. \tag{3.137}$$

VEM core

The axial displacement field within the VEM is bilinear and can be described by

$$\begin{aligned} u_v(\xi,\zeta_v) = {} & u_1\,\phi_1(\xi)\,\Lambda_1(\zeta_v) + u_2\,\phi_2(\xi)\,\Lambda_1(\zeta_v) \\ & + u_3\,\phi_2(\xi)\,\Lambda_2(\zeta_v) + u_4\,\phi_1(\xi)\,\Lambda_2(\zeta_v)\,, \end{aligned} \tag{3.138}$$

or in matrix form,

$$u_v(\xi,\zeta_v) = \{N_{uv}(\xi,\zeta_v)\}^T\{a\} \tag{3.139}$$

where

$$\{N_{uv}(\xi,\zeta_v)\} = \begin{Bmatrix} \phi_1(\xi)\,\Lambda_1(\zeta_v) \\ 0 \\ 0 \\ \phi_1(\xi)\,\Lambda_2(\zeta_v) \\ \phi_2(\xi)\,\Lambda_1(\zeta_v) \\ 0 \\ 0 \\ \phi_2(\xi)\,\Lambda_2(\zeta_v) \end{Bmatrix} \tag{3.140}$$

and the DOF vector $\{a\}$ comes from Equation (3.128). Assuming the transverse displacement field can be discretized by Equations (3.108), (3.132), and (3.133), the strains can be computed by Equation (3.114) replacing $\{N_u\}$ with $\{N_{uv}\}$. The element stiffness matrix then comes from Equation (3.116), and the element mass matrix comes from Equation (3.118).

3.6 Miles-Reinhall Model

Miles and Reinhall [62] recognized the utility of a *floating* constraining layer, i.e., one that is not pinned or otherwise constrained at the boundaries along with the base layer. They use Euler-Bernoulli beams for the facesheets and assume a bilinear displacement field within the VEM core.

Their kinematics are similar to the MM kinematics except that the base and constraining layers have independent transverse displacements w_1 and w_3 as shown in Figure 3.8.

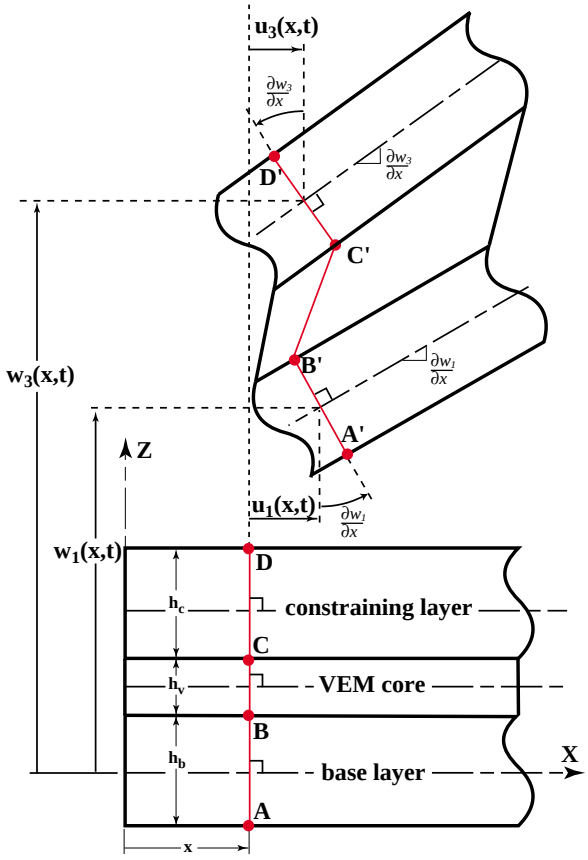

Figure 3.8: Kinematic assumptions used by Miles and Reinhall [62]

Miles and Reinhall derive equations of motion from Hamilton's principle using energy expressions for Euler-Bernoulli from Equations (3.99) and (3.101) (neglecting rotatary inertia on the later). They account for the kinetic energy of the core by applying half the VEM's mass to each facesheet in the facesheet's kinetic energy expressions. The authors calculate strain energy in the core due to shear and transverse normal strains assuming plane strain. The equations of motion are solved using the Ritz method and the authors investigate in various ways the effect of allowing the full-coverage constraining layer to "float." For their goal, they assumed the shear modulus of the VEM to be frequency-independent of the form $G_2^* = G_2\,(1+i)$. Additionally they assumed Young's modulus in the VEM to be $E_2 = 2.6\,G_2$, i.e., a Poisson's ratio of 0.3, and made the statement, "The actual Poisson's ratio will not differ significantly from this value."

The key differences between Miles and Reinhall's work and the approach presented here are that this work

1. shows that the error associated with the MM modeling are much more pronounced for partial than for full coverage constraining layers,
2. looks at the effect of displacement fields of higher order than linear,
3. uses more realistic VEM modeling (though this would not change any conclusions),
4. recognized and explores the consequences of uncertainty in Poisson's ratio for viscoelastic materials of engineering utility.

No attempt was made to reproduce Miles and Reinhall's mathematics, though it is described clearly in reference [62]. The Euler-Bernoulli facesheets and bilinear core are modeled correctly by the offset beam element in Section 3.4, and the bilinear core is just the four node, four-node C^0 element from Section 3.2.

Chapter 4

Implementation of Linear Viscoelasticity

Strategies for including VEM properties vary widely in accuracy and ease of use. If a viscoelastic coupon is excited with a sinusoidal force at a single frequency, the resulting displacement will have both in- and out-of-phase components, and thus the constitutive relationship is often characterized as complex as opposed to time dependent. With a "complex modulus" of the form

$$G^*(\omega) = G(\omega)\,(1 + i\,\eta(\omega)) \tag{4.1}$$

where $G(\omega)$ is the "storage modulus" and $\eta(\omega)$ is the loss factor, the response of a system to sinusoidal load can be determined at any single frequency. Examples of publications in the early literature assuming a complex modulus are [21] and [59]. Douglas and Yang [23] use a material with a shear modulus approximated by

$$G(\omega) = \left(1.42 \times 10^5\right) \exp\left[0.494 \ln\left(\frac{\omega}{2\pi}\right)\right] \quad [\mathrm{N/m^2}] \tag{4.2}$$

and loss factor of 1.46, and some authors were using this nearly 20 years later [14, 29].

The complex modulus approach dominated the literature until roughly 1981 when the modal strain energy method [40, 39], based on the above-referenced work by Ungar and Kerwin, became popular in industry. Using the modal strain energy (MSE) method, the modal loss factor for the j^{th} mode

is

$$\eta_j = \frac{\sum_{i=1}^{\#elem} \eta_i U_i^j}{\sum_{i=1}^{\#elem} U_i^j} \tag{4.3}$$

where

η_i = loss factor associated with i^{th} element at frequency of j^{th}mode,

U_i^j = strain energy in i^{th} element for the j^{th}mode

The material loss factor of most structural components is several orders of magnitude smaller than that of a viscoelastic material, so the modal loss factor is taken to be the VEM loss factor times the VEM's share of the system modal strain energy. The most appealing feature of this approach is that only real material properties, i.e., G in Equation (4.1), are used, and consequently the analysis is a standard real eigenvalue problem. This makes the MSE method an extremely valuable design tool, though it tends to overpredict damping and underpredict natural frequencies for high levels of system damping. Morganthaler [63] discusses this issue and suggests a scheme for correcting the predictions of damping.

There have been many publications in a broad class called "internal variable" methods, [28, 104, 110, 51] and no attempt is made here to present a detailed discussion of their relative merits. The method adopted in this dissertation models the VEM with Maxwell models as documented by A.R. Johnson *et al.* [34, 36, 35, 37], and it was chosen for its roots in polymer chemistry and rubber elasticity. Most of Johnson's earlier work (for example, [34, 36, 35]) address rubber elasticity from a continuum mechanics viewpoint, while the work in [37] formulates the viscoelasticity in a way that fits easily into conventional finite element analysis. It is this latter method that is discussed in the following sections. It should be pointed out that Yiu's [110, 111] work with Maxwell models is very similar to Johnson's for the linear cases, but Yiu in effect assumes the ratio of the two necessary material parameters to be constant.

Johnson uses strains as internal variables to represent the constitutive relationship of a Maxwell solid, as presented clearly in [37], and for brevity only key equations are reproduced here. Hooke's law for a linear elastic solid is written

$$\sigma_{ij} = C_{ijkl}\ \epsilon_{kl}, \tag{4.4}$$

and for a linear viscoelastic material subjected to an increment in strain this takes the form

$$\sigma_{ij}(t) = C_{ijkl}\,\Delta\epsilon_{kl} + \sigma^v_{ij}(t) = C_{ijkl}\,\Delta\epsilon_{kl} + C^v_{ijkl}(t)\;\Delta\epsilon_{kl}, \tag{4.5}$$

where $\sigma^v_{ij}(t)$ is the time-dependent stress due to the presence of a viscoelastic material and $C^v_{ijkl}(t)$ is that material's constitutive relationship. If one assumes a Maxwell model of the VEM, this time dependence can be approximated by a Prony series as

$$C^v_{ijkl}(t) = \sum_{n=1}^{N} C^n_{ijkl}\, e^{\frac{-t}{\tau_n}}, \tag{4.6}$$

the constitutive relationship becomes

$$\sigma_{ij}(t) = C_{ijkl}\,\Delta\epsilon_{kl} + \sum_{n=1}^{N} C^n_{ijkl}\, e^{\frac{-t}{\tau_n}}\,\Delta\epsilon_{kl}, \tag{4.7}$$

where $\tau_n \geq 0$ are retardation times for the Maxwell model of the viscoelastic material. From here, Johnson derives the equations for a Maxwell solid in differential form, and this results in a first-order differential equation for internal strains,

$$\frac{d\epsilon^n_{kl}}{dt} + \frac{\epsilon^n_{kl}}{\tau_n} = \frac{d\epsilon_{kl}}{dt} \quad \forall\ n, \tag{4.8}$$

and the constitutive relationship

$$\sigma_{ij}(t) = C_{ijkl}\,\epsilon_{kl}(t) + \sum_{n=1}^{N} C^n_{ijkl}\,\epsilon^n_{kl}(t)\,. \tag{4.9}$$

4.1 Time-Domain Implementation

A main attraction of internal variable (IV) methods is that they allow time-domain analyses using the time-dependent VEM properties. Some IV methods start with frequency-domain representations of the VEM properties and then come up with a realization in the time domain. The method based on Maxwell models is well-founded in viscoelasticity and leads to physical interpretations in both the time and frequency domains.

4.1.1 Predictor-Corrector Algorithm

Implementation of Equations (4.8) and (4.9) in a standard finite element analysis is straightforward. First write these in forms more familiar to engineers:

$$\frac{d\mathbf{e}^n}{dt} + \frac{\mathbf{e}^n}{\tau_n} = \frac{d\mathbf{e}}{dt} \quad \forall \ n \tag{4.10}$$

and

$$\mathbf{s}(t) = \mathbf{C}\,\mathbf{e}(t) + \sum_{n=1}^{N} \mathbf{C}^n\,\mathbf{e}^n(t), \tag{4.11}$$

where $\mathbf{s}, \mathbf{e},$ and $\mathbf{C}$ are the customary engineering stresses, strains, and elastic material properties. Vector $\mathbf{e}^n$ represents the internal variables and matrix $\mathbf{C}^n$ contains the viscoelastic material's time-dependent properties for n = 1,...,N, the number of terms in the Prony series of Equation (4.6). If the physical strains over an element are related to its degrees of freedom (DOFs) via $\mathbf{e} = \mathbf{Bu}$, the internal strains are similarly related to internal DOFs via $\mathbf{e}^n = \mathbf{Bu}^n$. These relationships allow Equation (4.10) to be written for any particular element affected by viscoelasticity in terms of physical and internal DOFs:

$$\frac{d\mathbf{u}^n}{dt} + \frac{\mathbf{u}^n}{\tau_n} = \frac{d\mathbf{u}}{dt} \quad \forall \ n. \tag{4.12}$$

It is key to remember that the true internal variables are the strains of Equation (4.10) and that the internal DOFs in Equation (4.12) are introduced as needed to represent the internal strains in the elements "touched" by a material with viscoelasticity. Johnson *et al.* [37] go through a variational formulation slightly altered by the presence of viscoelasticity and arrive at the following global equations of motion for a structure:

$$\mathbf{M}\ddot{\mathbf{U}}_g + \mathbf{K}_e\mathbf{U}_g = \mathbf{F}_m - \mathbf{F}_v \tag{4.13}$$

where mass $\mathbf{M}$, elastic stiffness $\mathbf{K}_e$, and mechanical load vector $\mathbf{F}_m$ are found by normal finite element procedures. The viscous load vector, $\mathbf{F}_v$, is the collection of the element viscous load vectors, $\mathbf{f}_v$, defined as

$$\mathbf{f}_v = \sum_{n=1}^{N} \mathbf{k}^n\mathbf{u}^n \tag{4.14}$$

for elements associated with viscoelastic properties. The element viscous stiffness matrix

$$\mathbf{k}^n = \int_{\Omega^e} \mathbf{B}^T\mathbf{C}^n\mathbf{B}\,d\Omega^e \quad \forall \ n \tag{4.15}$$

is created exactly as its counterpart element elastic stiffness matrix except the material properties for $\mathbf{C}^n$ come from the n^{th} term in the Prony series of Equation (4.6).

Equation (4.13) is not written in a form suitable for conventional time stepping scheme since only the mechanical load vector on the right-hand side is known for all time. Equation (4.14) shows that the viscous load vector at any time is a function of the internal DOFs at that time, and these internal DOFs have to satisfy both Equation (4.13) implicitly through the viscous load vector and Equation (4.12) explicitly. Johnson *et al.* [37] use the general approach, suitable for nonlinear problems as well, that requires iterating on the following procedure to go from some time t to the next time $t + \Delta t$.

1. form the right-hand side of (4.13) by assembling $\mathbf{f}_m(t + \Delta t)$ and $\mathbf{f}_v(t)$ (note that $\mathbf{f}_v(t + \Delta t)$ is unknown since $\mathbf{u}^n(t + \Delta t)$ is unknown);
2. solve for a candidate $\mathbf{U}_g(t + \Delta t)$ using an implicit Newmark algorithm;
3. use this along with $\mathbf{U}_g(t)$ and $\mathbf{u}^n(t)$ to find $\mathbf{u}^n(t + \Delta t)$ using a simple trapezoidal algorithm on Equation (4.12);
4. plug $\mathbf{u}^n(t + \Delta t)$ into Equation (4.14) to find $\mathbf{f}_v(t + \Delta t)$ and then update the right-hand side of Equation (4.13);
5. loop back to step 2 and repeat until $\mathbf{U}_g(t + \Delta t)$ converges.

For the linear problems addressed in the current work, this process requires only a few iterations.

4.1.2 Noniterative Augmented Forms

The iterative approach presented in the previous section is well suited for the problems generally addressed by Johnson *et al.* [37], but the extra computations are unnecessary for the linear problems presented in this dissertation. The iteration can be avoided by augmenting the vector of physical DOFs with the internal DOFs. A similar approach was taken by Yiu [110, 111]. There must be enough internal DOFs to create N (see Equation (4.6)) internal strains for each viscoelastic element in the model. Thus n_v viscoelastic elements with n_{DOF} degrees of freedom per element

would require the addition of $N \times n_v \times n_{DOF}$ internal DOF to the problem. The motivation for minimizing the number of terms in the Prony series should now be clear.

Development of the equations of motion for the augmented system begins by rewriting Equation (4.14) as

$$\mathbf{f}_v = \sum_{n=1}^{N} \mathbf{k}^n \mathbf{u}^n = \left[\begin{array}{c|c|c|c|c} \mathbf{k}^1 & \mathbf{k}^2 & \cdots & \mathbf{k}^N \end{array} \right] \left\{ \begin{array}{c} \mathbf{u}^1 \\ \hline \mathbf{u}^2 \\ \hline \vdots \\ \hline \mathbf{u}^N \end{array} \right\} = \mathbf{k}^v \mathbf{u}^v, \tag{4.16}$$

where $\mathbf{k}^v$ contains the element stiffness matrix evaluated with each of the N terms in the Prony series and $\mathbf{u}^v$ is all the internal DOFs for the particular element. The element viscous stiffness matrices can then be assembled at the system level, and Equation (4.13) can be rewritten as

$$\mathbf{M}\ddot{\mathbf{U}}_g + \mathbf{K}_e \mathbf{U}_g + \mathbf{K}_v \mathbf{U}_v = \mathbf{F}_m, \tag{4.17}$$

where $\mathbf{U}_g$ is all physical DOFs and $\mathbf{U}_v$ is all internal DOFs. It should be stressed that the internal DOFs in $\mathbf{U}_v$ are independent from element to element, and this can be seen by careful examination of Equation (4.16) and (4.17). Next recognize that the side constraint of Equation (4.12) can be enforced at the system level by the equation

$$\dot{\mathbf{U}}_v + [\mathbf{I}/\tau]\, \mathbf{U}_v = [\mathbf{I}_{vg}]\, \dot{\mathbf{U}}_g, \tag{4.18}$$

where the entries in diagonal matrix $[\mathbf{I}/\tau]$ and pointer matrix $[\mathbf{I}_{vg}]$ (links physical and internal DOFs) are placed so to enforce Equation (4.12). Equations (4.17) and (4.18) can now be combined in a second-order form as

$$\begin{bmatrix} \mathbf{M} & \mathbf{0} \\ \mathbf{0} & \mathbf{0} \end{bmatrix} \begin{Bmatrix} \ddot{\mathbf{U}}_g \\ \ddot{\mathbf{U}}_v \end{Bmatrix} + \begin{bmatrix} \mathbf{0} & \mathbf{0} \\ -\mathbf{I}_{vg} & \mathbf{I} \end{bmatrix} \begin{Bmatrix} \dot{\mathbf{U}}_g \\ \dot{\mathbf{U}}_v \end{Bmatrix} + \begin{bmatrix} \mathbf{K}_e & \mathbf{K}_v \\ \mathbf{0} & \mathbf{I}/\tau \end{bmatrix} \begin{Bmatrix} \mathbf{U}_g \\ \mathbf{U}_v \end{Bmatrix} = \begin{Bmatrix} \mathbf{F}_m \\ \mathbf{0} \end{Bmatrix}. \tag{4.19}$$

Defining the nodal velocities $\mathbf{V}_g = \dot{\mathbf{U}}_g$, it is now an easy step to write this in a first order form as

$$\begin{bmatrix} \mathbf{I} & \mathbf{0} & \mathbf{0} \\ \mathbf{0} & \mathbf{M} & \mathbf{0} \\ \mathbf{0} & \mathbf{0} & \mathbf{I} \end{bmatrix} \begin{Bmatrix} \dot{\mathbf{U}}_g \\ \dot{\mathbf{V}}_g \\ \dot{\mathbf{U}}_v \end{Bmatrix} + \begin{bmatrix} \mathbf{0} & -\mathbf{I} & \mathbf{0} \\ \mathbf{K}_e & \mathbf{0} & \mathbf{K}_v \\ \mathbf{0} & -\mathbf{I}_{vg} & \mathbf{I}/\tau \end{bmatrix} \begin{Bmatrix} \mathbf{U}_g \\ \mathbf{V}_g \\ \mathbf{U}_v \end{Bmatrix} = \begin{Bmatrix} \mathbf{0} \\ \mathbf{F}_m \\ \mathbf{0} \end{Bmatrix}. \tag{4.20}$$

Finally, this can be expressed in standard first-order form as

$$\frac{d}{dt}\begin{Bmatrix}\mathbf{U}_g\\ \mathbf{V}_g\\ \mathbf{U}_v\end{Bmatrix} = \begin{bmatrix}\mathbf{0} & \mathbf{I} & \mathbf{0}\\ -\mathbf{M^{-1}K}_e & \mathbf{0} & -\mathbf{M^{-1}K}_v\\ \mathbf{0} & \mathbf{I}_{vg} & -\mathbf{I}/\tau\end{bmatrix}\begin{Bmatrix}\mathbf{U}_g\\ \mathbf{V}_g\\ \mathbf{U}_v\end{Bmatrix} + \begin{Bmatrix}\mathbf{0}\\ \mathbf{M^{-1}F}_m\\ \mathbf{0}\end{Bmatrix}. \tag{4.21}$$

4.2 Frequency-Domain Implementation

If modal loss is the only objective of an analysis, it is much more efficient to cast the equations of motion in the frequency domain and estimate damping from a frequency-response function. The viscoelastic correspondence principle [50] provides the justification for transforming the equations of motion from the time to the frequency domain. Paraphrasing Findley [26], the correspondence principle lays out the following steps for a linear analysis:

1. solve the boundary-value problem using elastic properties,
2. take the Laplace transform of the elastic solution,
3. replace the appropriate elastic moduli by the Laplace transform of the viscoelastic modulus,
4. solve for the desired quantities in the Laplace domain, and
5. transform back to get the corresponding time-domain solutions.

As a first step, rewrite the constitutive relationship of Equations (4.5) and (4.6) for the planar problem as

$$\sigma_i(t) = Q_{ij}\,\Delta\epsilon_j + \sum_{n=1}^{N} Q_{ij}^n\, e^{\frac{-t}{\tau_n}}\,\Delta\epsilon_j, \tag{4.22}$$

where the reduced stiffness Q_{ij} is used for the planar problems studied here. In engineering practice, only the shear modulus is measured for viscoelastic materials, so in order to make use of data available express the constitutive relationship in terms of the shear modulus and Poisson's ratio. Poisson's ratio, in the absence of multi-axial material testing, will be assumed constant in this work. Making the substitution $E = 2\,(1+\nu)\,G$ in Equation (3.91), Q_{ij} becomes a reduced stiffness

matrix of the form

$$[Q] = \frac{2G}{1-\nu}\begin{bmatrix} 1 & \nu & 0 \\ \nu & 1 & 0 \\ 0 & 0 & \frac{1-\nu}{2} \end{bmatrix} \tag{4.23}$$

Since Poisson's ratio is taken to be constant, the time dependence of the constitutive relationship of Equation (4.7) is represented by the time-dependent *relaxation* shear modulus

$$G(t) = G_e + \sum_{n=1}^{N} G^n \, e^{\frac{-t}{\tau_n}} \tag{4.24}$$

where G_e is the elastic (instantaneous) portion of the modulus. The relaxation shear modulus satisfies the relationship

$$\sigma(t) = G(t) \; \epsilon_0, \tag{4.25}$$

where ϵ_0 is a step in strain at $t = 0$. The Boltzmann superposition principle [26] gives the time-dependent stress for a time-dependent strain to be

$$\sigma(t) = G_e \, \epsilon(t) + \int_0^t G(t-\alpha) \, \frac{\partial \epsilon(\alpha)}{\partial \alpha} \, d\alpha \tag{4.26}$$

The Laplace transform of Equation (4.26) is

$$\sigma(s) = G(s) \; s \, \epsilon(s) \, , \tag{4.27}$$

and the Laplace transform of Equation (4.24) is

$$G(s) = \frac{G_e}{s} + \sum_{n=1}^{N} \frac{G^n \tau_n}{1 + s \, \tau_n}. \tag{4.28}$$

The viscoelastic modulus that satisfies $\bar{\sigma}(s) = G(s) \, \bar{\epsilon}(s)$ is

$$\hat{G}(s) = sG(s) = G_e + \sum_{n=1}^{N} \frac{G^n s \, \tau_n}{1 + s \, \tau_n} \tag{4.29}$$

The constitutive relationship from Equation (4.23) can now be written in the Laplace domain as

$$[Q(s)] = \left(G_e + \sum_{n=1}^{N} \frac{G^n s \, \tau_n}{1 + s \, \tau_n} \right) \frac{2}{1-\nu} \begin{bmatrix} 1 & \nu & 0 \\ \nu & 1 & 0 \\ 0 & 0 & \frac{1-\nu}{2} \end{bmatrix}, \tag{4.30}$$

and any finite element stiffness matrix from Sections 3.2, 3.3, 3.4.3, or 3.5.3 can be split into elastic and viscous components:

$$[K(s)] = [K_e] + \sum_{n=1}^{N} \frac{G^n s\,\tau_n}{1 + s\,\tau_n} [K_v^n] \tag{4.31}$$

The equations of motions derived in the earlier sections were in the general form

$$\mathbf{M}\ddot{\mathbf{U}}(t) + \mathbf{K}(t)\,\mathbf{U} = \mathbf{f}(t) \tag{4.32}$$

By the viscoelastic correspondence principle take the Laplace transform assuming zero initial conditions to get

$$\left[s^2\,\mathbf{M} + \mathbf{K}(s)\right]\mathbf{U}(s) = \mathbf{f}(s) \tag{4.33}$$

Substituting Equation (4.31) into Equation (4.33) yields the transfer function between the finite element degrees of freedom and any general force vector

$$\mathbf{H}(s) = \left[s^2\mathbf{M} + \mathbf{K_e} + \sum_{n=1}^{N} \frac{\mathbf{K}_v^n s\,\tau_n}{1 + s\,\tau_n}\right]^{-1}, \tag{4.34}$$

or equivalently in the frequency domain ($s = i\omega$),

$$\mathbf{H}(i\omega) = \left[-\omega^2\mathbf{M} + \mathbf{K_e} + \sum_{n=1}^{N} \frac{\mathbf{K}_v^n\, i\omega\,\tau_n}{1 + i\omega\,\tau_n}\right]^{-1} \tag{4.35}$$

4.3 Material Constants for ISD 112

Equation 4.24 defines the Maxwell model of the time-dependent shear modulus, but the question remains as to how to determine the constants G_e and G^n. The complex shear modulus G^* is obtained by making the substitution $s = i\omega$ in Equation (4.29).

$$G^*(\omega) = \hat{G}(s)\Big|_{s=i\omega} = G_e + \sum_{n=1}^{N} \frac{G^n i\omega\tau_n}{1 + i\omega\tau_n} = G'(\omega) + i\,G''(\omega), \tag{4.36}$$

where the real (G') and imaginary (G'') components are

$$G'(\omega) = G_e + \sum_{n=1}^{N} \frac{G^n\omega^2\tau_n^2}{1 + \omega^2\tau_n^2} \quad \text{and} \quad G''(\omega) = \sum_{n=1}^{N} \frac{G^n\omega\tau_n}{1 + \omega^2\tau_n^2}. \tag{4.37}$$

The viscoelastic material used in these analyses was 3M's ISD 112, and raw test data for the shear modulus was provided by CSA Engineering, Inc., of Palo Alto, CA. The shear modulus was calculated by measuring the applied force and resulting displacement on a shear specimen of the material at a discrete set of temperatures[8]. The principle of time-temperature superposition [25] implies that viscoelastic properties at measured at one temperature can be related to that at another temperature through only a shift in the time scale. Call this shift factor α_T, and, from Reference [25], multiply each τ_n in Equation (4.37) by α_T. Because of the form of the equations, this produces the same result as multiplying each each ω by α_T. Thus, G' measured at a frequency ω at some temperature T is equivalent to G' measured at frequency $\alpha_T\omega$ and at reference temperature T_0. The shift relationship holds applies to G'' in an analogous manner. Ferry mentions that there is an additional factor for thermal expansion involved, but it is very close to unity.

Figure 4.1 shows the raw data shifted to room temperature. Obviously there is some amount of

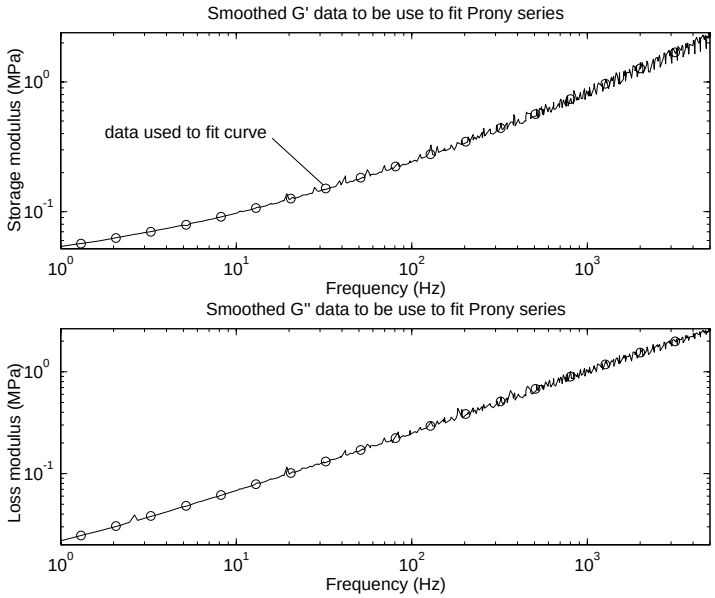

Figure 4.1: Subset of temperature-shifted data on which fit performed

scatter in the data, particularly at the higher frequencies. The data were smoothed simply by only using 20 points spaced evenly over the frequency range, as shown in Figure 4.1. I then used routine `constr` (constrained optimization) in MATLAB to minimize the error between these 20 points and G' and G'' from Equation (4.37) with the constants the optimization routine determines. The

general goal of the optimization it to minimize for all $\mathbf{X}$ some function $f(\mathbf{X})$ such that $\mathbf{G}(\mathbf{X}) \leq 0$, where $\mathbf{X}$ is a vector containing the values of G and τ from Equation (4.37). The constraint $\mathbf{G}(\mathbf{X})$ is merely that all the constants are positive, the error function $f(\mathbf{X})$ is just the 2-norm of the differences between the raw and calculated G' and G'' plus the product of all the shear moduli. This last product was an effort to *encourage* the optimization routine to eliminate terms if possible, i.e., make one of the $G^n = 0$, since terms are costly in time-domain representations. Figures 4.2, 4.3, and 4.4 show 6-, 5-, and 3-term fits of the data. Since the analyses using these actual properties were done in the frequency domain, the 6-term fit was used as opposed to fits with fewer terms since the computational penalty was not large (see Section 4.2). The actual values for the six-

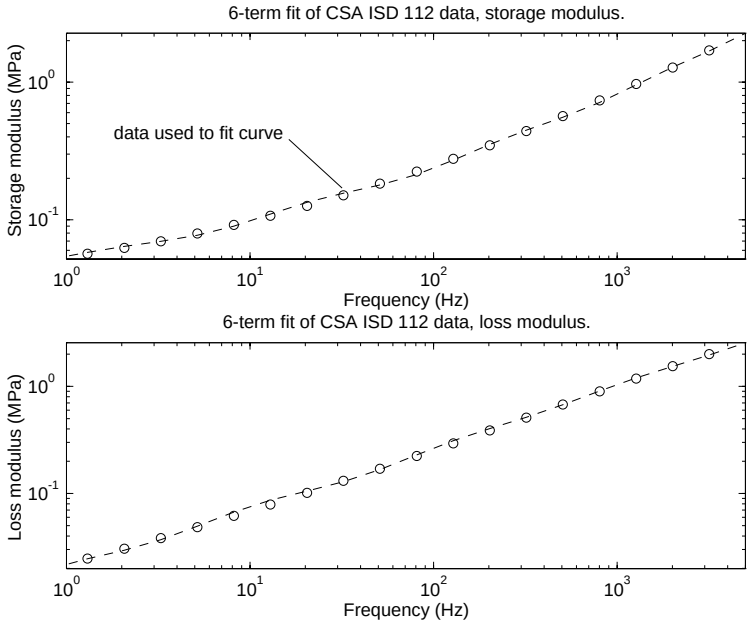

Figure 4.2: Six-term representation of CSA data for the shear modulus of ISD 112

term fit are given in Table 4.1. Note that there are six terms in the fit, only five of which are time dependent.

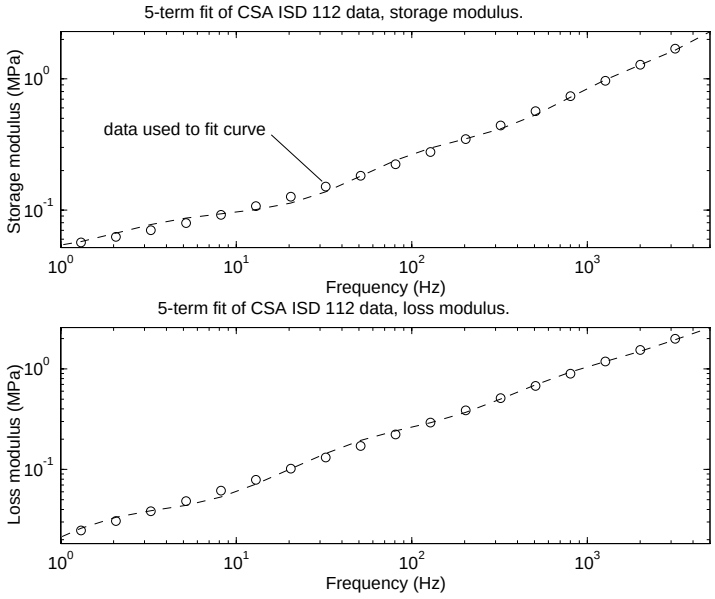

Figure 4.3: Five-term representation of CSA data for the shear modulus of ISD 112

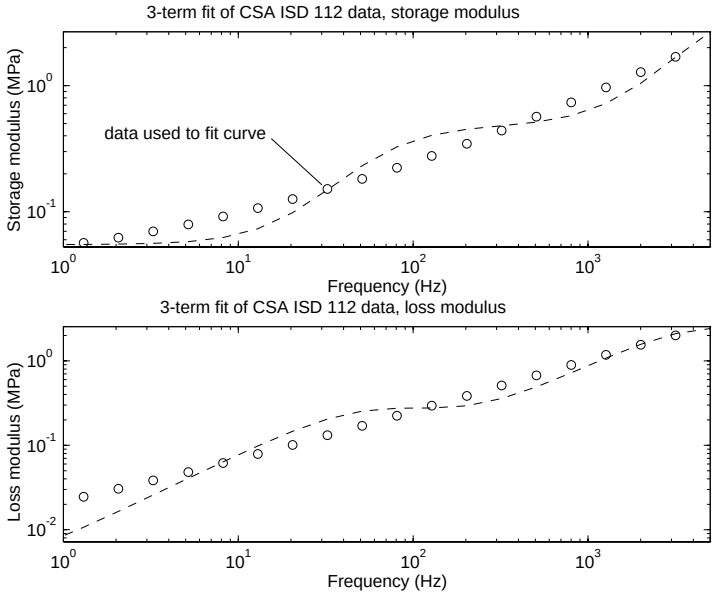

Figure 4.4: Three-term representation of CSA data for the shear modulus of ISD 112

Table 4.1: Constants used in six-term fit of ISD 112

n	G^n (psi)	τ_n
elastic	6.57	∞
1	5.09	5.5871 e-1
2	20.23	3.2035 e-2
3	58.61	3.0153 e-3
4	174.35	4.5824 e-4
5	1098.7	5.9317 e-5

Chapter 5

Comparison of Damping Predictions From Various Modeling Approaches

The principle design variables for a damping design as listed in Section 1.1.2 are

1. the thickness of the VEM,
2. the modulus of the VEM (frequency and temperature dependent!),
3. the location of the VEM,
4. the thickness of the constraining layer, and
5. the modulus of the constraining layer, i.e., the type of material.

In theory these can be pieced together in an infinite number of ways to maximize the damping added to a structure, but in practice the options are fewer. As for the VEM, for instance, the engineer will have to choose from perhaps a dozen materials easily obtainable, and these materials will only be available in discrete thicknesses. The location of an add-on damping treatment is often limited by interference with surrounding structure. Finally, there is often a conflict between increasing the thickness of the constraining layer to increase performance and minimizing the weight added to the structure. The point of this argument is that it is unrealistic to think that by plotting tens of thousands of combinations of the above design variables an engineer will be able to read this (or any other) document and produce a design without analysis. Therefore a set of eight cases

are investigated to identify modeling trends and to raise questions in the mind of the engineer performing the damping design.

The analysis set of sandwich beams consists of the eight possible combinations of two base beam lengths, two viscoelastic material thicknesses, and two constraining layer thicknesses. The dimensions are summarized in Table 5.1. The lengths are reported later in terms of the aspect ratio of the

Table 5.1: Dimensions of test cases for study of full-coverage damping treatments

		thickness (inches)		
case	length	base	VEM	constr
1	5.0†	0.125	0.005	0.125
2	5.0	0.125	0.050	0.125
3	5.0	0.125	0.005	0.010
4	5.0	0.125	0.050	0.010
5	20.0	0.125	0.005	0.125
6	20.0	0.125	0.050	0.125
7	20.0	0.125	0.005	0.010
8	20.0	0.125	0.050	0.010

† all dimensions are inches

0.125-inch-thick base layer, so the first four cases have aspect ratios of 40 and the last four are 160. The thicknesses are listed in mili-inches (mils) as base/VEM/constraining layers, e.g., 125/5/125 for case 1. ISD 112, manufactured by 3M, was chosen as the viscoelastic material for the study. Besides being widely used in academia and industry, it is easy to apply, properties are readily available, and 3M is willing to give away free samples for research. The VEM thicknesses of 5 and 50 mils where chosen to represent one thin and one relatively thick VEM layer. The 10-mil-thick constraining layer (CL) was chosen to be weak in bending relative to the 125-mil-thick base layer. The 125-mil-thick CL was chosen to match the thickness of the base layer. A "rule of thumb" for damping designs (also see [67, 82]) is that the optimum stiffness of a CL is the same as that of the base layer. All the elastic members from this point onward are unit-width aluminum.

Next, anticipate the applicability of the Mead and Markus (MM) assumptions to the sandwich beam comprising of the 125-mil-thick base beam and the eight combinations of VEM and constraining layer from Table 5.1. Central to the MM model is the assumption that the constraining layer

has the same transverse displacements as the base layer. This condition is best enforced by the combination of a stiff VEM and a weak constraining layer. Additionally, it is easier to bend a long beam than a short one, so cases 5–8 should adhere better to MM than the corresponding cases 1–4. Within each set of four cases, the combination of thin VEM and thin constraining layer (cases 3 and 7) should be best represented by the MM assumptions, and the combination of thick VEM and thick CL (cases 2 and 6) should be the worst.

The first step , before analyzing the test cases of Table 5.1, in assessing the accuracy of different sets of modeling assumptions is determining which is correct, as outlined in Section 1.2. A good vehicle for exploring questions of element type, mesh resolution, and element aspect ratio is Pagano's 1969 elasticity solution [76] for a simply supported beam in cylindrical bending, shown in Figure 5.1. Though a statics problem, the deformed shape is the same as the fundamental mode of a pinned-end

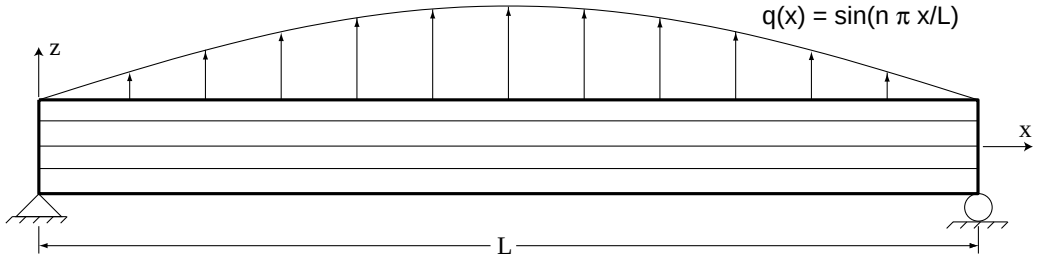

Figure 5.1: Pinned-end beam in cylindrical bending analyzed by Pagano [76]

beam and similar to that of a free-free beam, so the distribution of strain energy between layers should be representative. The goal of this first exercise is to choose an element type and rough resolution that can be used for the more general studies that follow.

5.1 Cylindrical Bending

Pagano [76] does a plane-strain problem in which he separates the stress fields into unknown functions of z and harmonic functions of x (see Figure 5.1) corresponding to the loading function and its spatial derivative. One effect of this is that the transverse displacements are zero for all layers at the ends, but there are no other artificial constraints on the relative transverse displacements of different layers.

Pagano chooses the following material constants to simulate a stiff graphite/epoxy material:

$$E_L = 25 \times 10^6 \text{ psi } (172 \text{ GPa}) \qquad E_T = 10^6 \text{ psi } (6.9 \text{ GPa})$$

$$G_{LT} = 0.5 \times 10^6 \text{ psi } (3.5 \text{ GPa}) \qquad G_{TT} = 0.2 \times 10^6 \text{ psi } (1.4 \text{ GPa})$$

$$\nu_{LT} = \nu_{TT} = 0.25$$

First reproduce Pagano's symmetric three-ply laminate of equal-thickness layers where the L direction corresponds to the x axis (Figure 5.1) for the outer two layers and the T direction is parallel to x in the middle layer. To better match Pagano's assumed solutions in the x direction, nodes at the ends of the C^0 meshes were restrained against transverse (z) deformation and those on the centerline with respect to the length were restrained against axial motion. Similar boundary conditions were applied to the C^1 mesh, though boundary conditions were needed for rotations at the ends and middle also. Tables 5.2 through 5.4 give a comparison of the strain energy in each layer and the displacements at the beam's center for beams with aspect ratios of 4, 40, and 400. Listed with Pagano's closed-form solution are FEA solutions for the C^1 element (C1-32) of Section 3.3 and C^0 elements with 20, 16, 12, 8, and 4 nodes (C0-20, C0-16, C0-12, C0-8, and C0-4). In order to be consistent with damped three-layer sandwich beams, the bottom layer is labeled "BL" for base layer, the middle "VEM" for viscoelastic material, and the top "CL" for constraining layer. The figures show that the higher order C^0 finite element models predict the closed-form energy distributions with only modest element resolution, though accuracy drops off slightly for the C0-8 element and dramatically for the C0-4 element at these levels of resolution.

Pagano's results show that as the aspect ratio of the beam gets shorter, the gradients in the shear stress get more severe near material boundaries [76]. Thus it is reasonable that the meshes, e.g., C0-20 and C0-16, converge more quickly for the beam aspect ratio of 40 in Table 5.3 than for the aspect ratio of 4 in Table 5.2. This trend in convergence is not, however, monotonic, since the same element resolution for the beam aspect ratio of 400 in Table 5.4 do not match Pagano's results as well as either of the shorter beams. Counteracting the smoothing of the stress gradients are errors due to high *element* aspect ratios. Even though the strain energy predictions aren't as good, the errors are very small when put in perspective with uncertainties in the viscoelastic material properties. Note from Table 5.4 that the error between the percent strain energy in the VEM predicted using C0-12 and C0-16 elements and Pagano's elasticity solution are less that 2%

for huge element aspect ratios of 1200. Closer analysis did not reveal why the higher order C0-20 element was 5.5% off, and this is especially puzzling when considering that the same element with aspect ratio 600 was only 0.36% different from elasticity solution. In any case, the higher order C^0 elements perform well for this composite sandwich beam at even large element aspect ratios.

Tables 5.2 through 5.4 show that only a modest number of higher order elements are needed to predict the distribution of strain energy well for this set of material properties. Even elements with aspect ratios over 1000 worked well, but predictably the errors were smallest for the highest order elements. The C1-32 element with traction continuity at the layer boundaries does about as well as the higher order C^0 elements with the same number of DOFs. It is interesting to note that mesh of the C0-16 elements results in between two and three times the number of system DOFs as the same mesh with C1-32 elements, even though both elements have 32 degrees of freedom. This is due to the C1-32 element having 8 DOFs at each of 4 nodes and the C0-16 element having 2 DOFs at each of 16 nodes. Each of the 4 nodes on the C1-32 element can connect to as many as 3 other elements in a regular rectangular mesh, whereas 12 of the 16 nodes on the C0-16 element are on the sides and therefore can attach to either 0 or 1 other elements. Consequently, many more DOFs are eliminated during the assembly process on the C^1 element.

The mismatch in material properties experienced with the three-layer composite sandwich ($0°/90°/0°$) is small compared to that of most sandwich damping treatments. To test the effect of this, Tables 5.5, 5.6, and 5.7 are strain energies for the same three beam aspect ratios for a sandwich comprised of aluminum facesheets and a soft viscoelastic core, all of equal thickness. The viscoelastic material was modeled as an isotropic material with shear modulus 50 psi and Poisson's ratio 0.49. This shear modulus is at the low end of those used for analyses later in this section.

On the average the predictions of MSE distributions are better for the viscoelastic sandwich beam than for the composite beam. In particular note the difference in results predicted by the C1-32 and C0-8 elements for the beam aspect ratio of 400. The higher order C^0 still perform well, and the C0-4 element still performs poorly. Results presented in the coming sections will imply that this poor performance is more due to inaccurate modeling the elastic rather than the viscoelastic elements. An important point here is that the C0-12. C0-16, and C0-20 elements all predict the VEM strain energy well with element aspect ratios greater than 1000. This is consistent with

Table 5.2: Comparison with Pagano's closed-form results for various elements modeling a three-layer composite-material beam with aspect ratio 4

		aspect	# elements		% strain energy		
element	DOF	ratio	axial	0°/90°/0°†	0° (bottom)	90°	0° (top)
Pagano	∞	n/a	∞	∞	25.6032243	45.4133374	28.9834383
C1-32	66	3	4	1/1/1	25.6877204	45.2443473	29.0679323
	94	6	4	1/2/1	25.6757935	45.2753527	29.0488538
	146	1.5	8	1/1/1	25.6870575	45.2455229	29.0674196
	150	6	4	2/2/2	25.6058743	45.4090255	28.9851002
	206	12	4	2/4/2	25.6055439	45.4100283	28.9844278
	206	3	8	1/2/1	25.6751571	45.2764622	29.0483808
	326	3	8	2/2/2	25.6055097	45.4096941	28.9847962
C0-20	240	3	4	1/1/1	25.5994881	45.4210347	28.9794772
	307	6	4	1/2/1	25.5995176	45.4210482	28.9794343
	441	6	4	2/2/2	25.6033665	45.4129646	28.9836689
	496	1.5	8	1/1/1	25.6024016	45.4150296	28.9825689
	575	12	4	2/4/2	25.6033617	45.4129753	28.9836630
	635	3	8	1/2/1	25.6024146	45.4150241	28.9825613
	913	3	8	2/2/2	25.6032585	45.4132517	28.9834898
C0-16	187	3	4	1/1/1	25.5995884	45.4208099	28.9796016
	239	6	4	1/2/1	25.5996146	45.4208307	28.9795547
	343	6	4	2/2/2	25.6033677	45.4129617	28.9836706
	387	1.5	8	1/1/1	25.6024968	45.4148171	28.9826861
	447	12	4	2/4/2	25.6033629	45.4129725	28.9836646
	495	3	8	1/2/1	25.6025092	45.4148131	28.9826778
	711	3	8	2/2/2	25.6032590	45.4132505	28.9834905
C0-12	134	3	4	1/1/1	25.5981307	45.4238318	28.9780376
	171	6	4	1/2/1	25.5981558	45.4238543	28.9779899
	245	6	4	2/2/2	25.6034124	45.4128413	28.9837463
	278	1.5	8	1/1/1	25.6011129	45.4177059	28.9811812
	319	12	4	2/4/2	25.6034080	45.4128513	28.9837407
	355	3	8	1/2/1	25.6011249	45.4177024	28.9811728
	509	3	8	2/2/2	25.6032593	45.4132463	28.9834945
C0-8	81	3	4	1/1/1	25.9232715	44.6942475	29.3824809
	103	6	4	1/2/1	25.9231387	44.6945463	29.3823150
	147	6	4	2/2/2	25.6336701	45.3414726	29.0248573
	169	1.5	8	1/1/1	25.9156290	44.7152533	29.3691177
	191	12	4	2/4/2	25.6336550	45.3415051	29.0248400
	215	3	8	1/2/1	25.9154785	44.7155437	29.3689778
	307	3	8	2/2/2	25.6243764	45.3657914	29.0098322
C0-4	28	3	4	1/1/1	25.8049144	44.4033156	29.7917700
	35	6	4	1/2/1	25.7836307	44.4305262	29.7858431
	49	6	4	2/2/2	26.7094974	42.4820813	30.8084214
	60	1.5	8	1/1/1	24.9358806	46.6615416	28.4025778
	63	12	4	2/4/2	26.7036341	42.4897621	30.8066038
	75	3	8	1/2/1	24.9124673	46.6934189	28.3941138
	105	3	8	2/2/2	25.8799669	44.6607069	29.4593262

† number of elements through thickness of each of the three layers

Table 5.3: Comparison with Pagano's closed-form results for various elements modeling a three-layer composite-material beam with aspect ratio 40

		aspect	# elements		% strain energy		
element	DOF	ratio	axial	0°/90°/0°†	0° (bottom)	90°	0° (top)
Pagano	∞	n/a	∞	∞	48.07669008	3.9007400	48.0225610
C1-32	66	30	4	1/1/1	48.0695660	3.9149881	48.0154459
	94	60	4	1/2/1	48.0694592	3.9152031	48.0153377
	146	15	8	1/1/1	48.0767218	3.9006779	48.0226004
	150	60	4	2/2/2	48.0694486	3.9152225	48.0153290
	206	120	4	2/4/2	48.0694370	3.9152459	48.0153171
	206	30	4	1/2/1	48.0767073	3.9007078	48.0225850
	326	30	8	2/2/2	48.0766385	3.9008432	48.0225183
C0-20	240	30	4	1/1/1	48.0766838	3.9007527	48.0225635
	307	60	4	1/2/1	48.0766861	3.9007480	48.0225659
	441	60	4	2/2/2	48.0766885	3.9007429	48.0225686
	496	15	8	1/1/1	48.0766897	3.9007409	48.0225695
	575	120	4	2/4/2	48.0766891	3.9007420	48.0225689
	635	30	8	1/2/1	48.0766897	3.9007406	48.0225696
	913	30	8	2/2/2	48.0766901	3.9007400	48.0225700
C0-16	187	30	4	1/1/1	48.0766815	3.9007573	48.0225612
	239	60	4	1/2/1	48.0766839	3.9007524	48.0225637
	343	60	4	2/2/2	48.0766867	3.9007468	48.0225665
	387	15	8	1/1/1	48.0766897	3.9007408	48.0225695
	447	120	4	2/4/2	48.0766873	3.9007457	48.0225670
	495	30	8	1/2/1	48.0766898	3.9007405	48.0225697
	711	30	8	2/2/2	48.0766902	3.9007400	48.0225699
C0-12	134	30	4	1/1/1	48.0758446	3.9024309	48.0217245
	171	60	4	1/2/1	48.0758464	3.9024272	48.0217263
	245	60	4	2/2/2	48.0758758	3.9023684	48.0217558
	278	15	8	1/1/1	48.0766779	3.9007644	48.0225577
	319	120	4	2/4/2	48.0758763	3.9023674	48.0217564
	355	30	8	1/2/1	48.0766780	3.9007641	48.0225579
	509	30	8	2/2/2	48.0766786	3.9007629	48.0225585
C0-8	81	30	4	1/1/1	47.8690482	4.3159971	47.8149547
	103	60	4	1/2/1	47.8690272	4.3160393	47.8149336
	147	60	4	2/2/2	47.8801576	4.2937801	47.8260623
	169	15	8	1/1/1	48.0634704	3.9271766	48.0093530
	191	120	4	2/4/2	47.8801502	4.2937948	47.8260550
	215	30	8	1/2/1	48.0634737	3.9271700	48.0093563
	307	30	8	2/2/2	48.0642404	3.9256369	48.0101228
C0-4	28	30	4	1/1/1	43.8992544	12.2491882	43.8515574
	35	60	4	1/2/1	43.9003627	12.2469665	43.8526708
	49	60	4	2/2/2	43.8986076	12.2502633	43.8511291
	60	15	8	1/1/1	46.1010998	7.8506852	46.0482150
	63	120	4	2/4/2	43.8988859	12.2497054	43.8514087
	75	30	8	1/2/1	46.1036325	7.8456149	46.0507526
	105	30	8	2/2/2	46.1031838	7.8463058	46.0505105

† number of elements through thickness of each of the three layers

Table 5.4: Comparison with Pagano's closed-form results for various elements modeling a three-layer composite-material beam with aspect ratio 400

		aspect	# elements		% strain energy		
element	DOF	ratio	axial	0°/90°/0°†	0° (bottom)	90°	0° (top)
Pagano	∞	n/a	∞	∞	49.9036712	0.1932481	49.9030806
C1-32	66	300	4	1/1/1	48.9281203	2.1443555	48.9275242
	94	600	4	1/2/1	48.9224457	2.1557241	48.9218302
	146	150	8	1/1/1	49.8927845	0.2150178	49.8921978
	150	600	4	2/2/2	48.9466480	2.1072857	48.9460663
	206	1200	4	2/4/2	48.9458756	2.1088769	48.9452476
	206	300	8	1/2/1	49.8927120	0.2151672	49.8921208
	326	300	8	2/2/2	49.8930127	0.2146062	49.8923811
C0-20	240	300	4	1/1/1	49.9037763	0.1932630	49.9029608
	307	600	4	1/2/1	49.9033008	0.1939450	49.9027543
	441	600	4	2/2/2	49.9037297	0.1935276	49.9027427
	496	150	8	1/1/1	49.9036123	0.1933283	49.9030594
	575	1200	4	2/4/2	49.9090660	0.1824990	49.9084350
	635	300	8	1/2/1	49.9040387	0.1917179	49.9042434
	913	300	8	2/2/2	49.9045664	0.1907283	49.9047053
C0-16	187	300	4	1/1/1	49.9033678	0.1938559	49.9027763
	239	600	4	1/2/1	49.9028002	0.1947135	49.9024864
	343	600	4	2/2/2	49.9034329	0.1940813	49.9024859
	387	150	8	1/1/1	49.9035545	0.1933836	49.9030619
	447	1200	4	2/4/2	49.9030242	0.1956720	49.9013039
	495	300	8	1/2/1	49.9033136	0.1936665	49.9030199
	711	300	8	2/2/2	49.9033736	0.1933533	49.9032731
C0-12	134	300	4	1/1/1	49.9028272	0.1949244	49.9022484
	171	600	4	1/2/1	49.9025340	0.1955232	49.9019428
	245	600	4	2/2/2	49.9023936	0.1956286	49.9019778
	278	150	8	1/1/1	49.9034683	0.1936320	49.9028997
	319	1200	4	2/4/2	49.9017741	0.1968320	49.9013940
	355	300	8	1/2/1	49.9036458	0.1933010	49.9030532
	509	300	8	2/2/2	49.9036354	0.1932219	49.9031427
C0-8	81	300	4	1/1/1	49.8288035	0.3430025	49.8281940
	103	600	4	1/2/1	49.8288915	0.3428234	49.8282851
	147	600	4	2/2/2	49.8291970	0.3423426	49.8284604
	169	150	8	1/1/1	49.8382485	0.3241324	49.8376190
	191	1200	4	2/4/2	49.8289179	0.3427920	49.8282901
	215	300	8	1/2/1	49.8382575	0.3240668	49.8376757
	307	300	8	2/2/2	49.8391752	0.3223255	49.8384994
C0-4	28	300	4	1/1/1	41.7136962	16.5731334	41.7131704
	35	600	4	1/2/1	41.7137124	16.5731009	41.7131867
	49	600	4	2/2/2	41.7137025	16.5731208	41.7131767
	60	150	8	1/1/1	41.8587295	16.2831171	41.8581534
	63	1200	4	2/4/2	41.7137063	16.5731131	41.7131806
	75	300	8	1/2/1	41.8588042	16.2829677	41.8582281
	105	300	8	2/2/2	41.8587569	16.2830621	41.8581810

† number of elements through thickness of each of the three layers

Table 5.5: Comparison with Pagano's closed-form results for various elements modeling a three-layer viscoelastic sandwich beam with aspect ratio 4

		aspect	# elements		% strain energy		
element	DOF	ratio	axial	B/V/C†	BL	VEM	CL
Pagano	∞	n/a	∞	∞	7.2378412	16.4122110	76.3499478
C1-32	66	3	4	1/1/1	7.2302724	16.4058486	76.3638790
	94	6	4	1/2/1	7.2302758	16.4059494	76.3637748
	146	1.5	8	1/1/1	7.2376463	16.4121112	76.3502425
	150	6	4	2/2/2	7.2314579	16.4065725	76.3619696
	206	12	4	2/4/2	7.2314679	16.4067098	76.3618223
	206	3	8	1/2/1	7.2376433	16.4121086	76.3502481
	326	3	8	2/2/2	7.2377599	16.4121574	76.3500827
C0-20	240	3	4	1/1/1	7.2724713	16.4261471	76.3013816
	307	6	4	1/2/1	7.2377058	16.4121348	76.3501595
	441	6	4	2/2/2	7.2385935	16.4125108	76.3488958
	496	1.5	8	1/1/1	7.2463471	16.4156529	76.3380000
	575	12	4	2/4/2	7.2375587	16.4120897	76.3503516
	635	3	8	1/2/1	7.2379799	16.4122661	76.3497540
	913	3	8	2/2/2	7.2380371	16.4122903	76.3496727
C0-16	187	3	4	1/1/1	7.2724692	16.4261474	76.3013834
	239	6	4	1/2/1	7.2377041	16.4121341	76.3501618
	343	6	4	2/2/2	7.2385908	16.4125097	76.3488995
	387	1.5	8	1/1/1	7.2463472	16.4156530	76.3379998
	447	12	4	2/4/2	7.2375570	16.4120890	76.3503540
	495	3	8	1/2/1	7.2379799	16.4122661	76.3497540
	711	3	8	2/2/2	7.2380371	16.4122902	76.3496727
C0-12	134	3	4	1/1/1	7.2718728	16.4259000	76.3022272
	171	6	4	1/2/1	7.2370821	16.4118712	76.3510467
	245	6	4	2/2/2	7.2377424	16.4121508	76.3501068
	278	1.5	8	1/1/1	7.2463183	16.4156409	76.3380408
	319	12	4	2/4/2	7.2367114	16.4117315	76.3515571
	355	3	8	1/2/1	7.2379439	16.4122508	76.3498053
	509	3	8	2/2/2	7.2380209	16.4122834	76.3496957
C0-8	81	3	4	1/1/1	7.1545303	16.3744600	76.4710096
	103	6	4	1/2/1	7.0325134	16.3226778	76.6448088
	147	6	4	2/2/2	7.0548427	16.3326789	76.6124784
	169	1.5	8	1/1/1	7.3096707	16.4404480	76.2498814
	191	12	4	2/4/2	7.0479915	16.3297103	76.6222982
	215	3	8	1/2/1	7.2080088	16.3994296	76.3925617
	307	3	8	2/2/2	7.2275081	16.4077262	76.3647657
C0-4	28	3	4	1/1/1	1.0298741	8.6327096	90.3374163
	35	6	4	1/2/1	0.7638025	7.6197933	91.6164042
	49	6	4	2/2/2	0.8266980	7.8808841	91.2924179
	60	1.5	8	1/1/1	3.7119747	13.8426592	82.4453662
	63	12	4	2/4/2	0.7608863	7.6094090	91.6297047
	75	3	8	1/2/1	2.8632798	12.7414399	84.3952804
	105	3	8	2/2/2	3.3853050	13.4618889	83.1528061

† number of elements through thickness in the Base, VEM, and Constraining layers

Table 5.6: Comparison with Pagano's closed-form results for various elements modeling a three-layer viscoelastic sandwich beam with aspect ratio 40

		aspect	# elements		% strain energy		
element	DOF	ratio	axial	B/V/C†	BL	VEM	CL
Pagano	∞	n/a	∞	∞	43.4004538	13.1835138	43.4160325
C1-32	66	30	4	1/1/1	41.9680737	12.9725810	45.0593453
	94	60	4	1/2/1	42.0694631	13.1907264	44.7398105
	146	15	8	1/1/1	43.3858878	13.1776569	43.4364553
	150	60	4	2/2/2	42.1453859	13.1654371	44.6891771
	206	120	4	2/4/2	42.2933754	13.4298715	44.2767532
	206	30	8	1/2/1	43.3860904	13.1781551	43.4357545
	326	30	8	2/2/2	43.3871964	13.1783880	43.4344157
C0-20	240	30	4	1/1/1	43.4012875	13.1818416	43.4168709
	307	60	4	1/2/1	43.4012898	13.1818383	43.4168719
	441	60	4	2/2/2	43.4007054	13.1830196	43.4162750
	496	15	8	1/1/1	43.4005008	13.1834205	43.4160788
	575	120	4	2/4/2	43.4007280	13.1830215	43.4162505
	635	30	8	1/2/1	43.4004933	13.1834192	43.4160875
	913	30	8	2/2/2	43.4004493	13.1835024	43.4160484
C0-16	187	30	4	1/1/1	43.4013003	13.1818181	43.4168816
	239	60	4	1/2/1	43.4012975	13.1818147	43.4168877
	343	60	4	2/2/2	43.4007416	13.1829717	43.4162867
	387	15	8	1/1/1	43.4005025	13.1834177	43.4160798
	447	120	4	2/4/2	43.4007479	13.1829736	43.4162785
	495	30	8	1/2/1	43.4004956	13.1834154	43.4160890
	711	30	8	2/2/2	43.4004633	13.1834842	43.4160526
C0-12	134	30	4	1/1/1	43.4033836	13.1776445	43.4189720
	171	60	4	1/2/1	43.4033845	13.1776441	43.4189715
	245	60	4	2/2/2	43.4033193	13.1777657	43.4189150
	278	15	8	1/1/1	43.4006180	13.1831839	43.4161981
	319	120	4	2/4/2	43.4033187	13.1777644	43.4189170
	355	30	8	1/2/1	43.4006188	13.1831839	43.4161973
	509	30	8	2/2/2	43.4006122	13.1831912	43.4161966
C0-8	81	30	4	1/1/1	43.7712223	12.4407719	43.7880059
	103	60	4	1/2/1	43.7712572	12.4407013	43.7880415
	147	60	4	2/2/2	43.7569582	12.4693505	43.7736913
	169	15	8	1/1/1	43.4890079	13.0061327	43.5048594
	191	120	4	2/4/2	43.7569713	12.4693241	43.7737046
	215	30	8	1/2/1	43.4890099	13.0061282	43.5048619
	307	30	8	2/2/2	43.4879762	13.0082020	43.5038218
C0-4	28	30	4	1/1/1	45.9171426	2.7007241	51.3821334
	35	60	4	1/2/1	45.9092209	2.7057843	51.3849948
	49	60	4	2/2/2	45.9117493	2.7041875	51.3840631
	60	15	8	1/1/1	48.9023300	0.8583714	50.2392986
	63	120	4	2/4/2	45.9097657	2.7054547	51.3847797
	75	30	8	1/2/1	48.9003115	0.8596388	50.2400497
	105	30	8	2/2/2	48.9029865	0.8582707	50.2387428

† number of elements through thickness in the Base, VEM, and Constraining layers

Table 5.7: Comparison with Pagano's closed-form results for various elements modeling a three-layer viscoelastic sandwich beam with aspect ratio 400

		aspect	# elements		% strain energy		
element	DOF	ratio	axial	B/V/C†	BL	VEM	CL
Pagano	∞	n/a	∞	∞	31.0555344	37.8896838	31.0547819
C1-32	66	300	4	1/1/1	29.2102126	40.9236742	29.8661132
	94	600	4	1/2/1	30.0539920	39.7036945	30.2423135
	146	150	8	1/1/1	30.9637221	37.9311218	31.1051562
	150	600	4	2/2/2	30.0583599	39.6839568	30.2576833
	206	1200	4	2/4/2	30.5375744	38.8747242	30.5877014
	206	300	8	1/2/1	30.9953668	37.9494157	31.0552175
	326	300	8	2/2/2	30.9967663	37.9437387	31.0594950
C0-20	240	300	4	1/1/1	31.0476175	37.9164580	31.0359245
	307	600	4	1/2/1	31.0329832	37.9000139	31.0670029
	441	600	4	2/2/2	31.0081694	37.9370293	31.0548013
	496	150	8	1/1/1	31.0411082	37.9187080	31.0401838
	575	1200	4	2/4/2	30.9955582	37.9317475	31.0726943
	635	300	8	1/2/1	31.0293450	37.9031770	31.0674780
	913	300	8	2/2/2	30.9985801	37.9574146	31.0440054
C0-16	187	300	4	1/1/1	31.0632122	37.8762341	31.0605538
	239	600	4	1/2/1	31.0657372	37.8753258	31.0589370
	343	600	4	2/2/2	31.0832010	37.8602571	31.0565419
	387	150	8	1/1/1	31.0524730	37.8981823	31.0493447
	447	1200	4	2/4/2	31.0856677	37.8593347	31.0549976
	495	300	8	1/2/1	31.0478387	37.8941041	31.0580572
	711	300	8	2/2/2	31.0650732	37.8606518	31.0742751
C0-12	134	300	4	1/1/1	31.0553352	37.8902623	31.0544025
	171	600	4	1/2/1	31.0547314	37.8907292	31.0545395
	245	600	4	2/2/2	31.0589405	37.8774808	31.0635787
	278	150	8	1/1/1	31.0580508	37.8849934	31.0569559
	319	1200	4	2/4/2	31.0637001	37.8764495	31.0598503
	355	300	8	1/2/1	31.0580480	37.8855529	31.0563992
	509	300	8	2/2/2	31.0490532	37.8955498	31.0553971
C0-8	81	300	4	1/1/1	31.1818886	37.6386839	31.1794275
	103	600	4	1/2/1	31.1813461	37.6384320	31.1802220
	147	600	4	2/2/2	31.1726505	37.6542800	31.1730696
	169	150	8	1/1/1	31.0959198	37.8101773	31.0939029
	191	1200	4	2/4/2	31.1748405	37.6523367	31.1728228
	215	300	8	1/2/1	31.0950154	37.8104382	31.0945464
	307	300	8	2/2/2	31.0935190	37.8134593	31.0930217
C0-4	28	300	4	1/1/1	49.9521093	0.0389739	50.0089168
	35	600	4	1/2/1	49.9521084	0.0389745	50.0089171
	49	600	4	2/2/2	49.9521086	0.0389744	50.0089171
	60	150	8	1/1/1	49.9705929	0.0462291	49.9831780
	63	1200	4	2/4/2	49.9521083	0.0389745	50.0089172
	75	300	8	1/2/1	49.9705927	0.0462291	49.9831782
	105	300	8	2/2/2	49.9705928	0.0462301	49.9831771

† number of elements through thickness in the Base, VEM, and Constraining layers

Kluesener's [44] finding in 1984 that accurate damping predictions are possible with element aspect ratios as high as 1000.

The C^1 element would be attractive if it yielded better or equal accuracy for fewer DOFs than the C^0 elements, but the results show that the element performs about as well only with the same number of DOFs. The process of enforcing traction continuity requires enforcing constraints by removing degrees of freedom, as in Equation (3.86), and this is a time-consuming operation. Even worse is the complexity added by matching time-dependent tractions in the presence of viscoelasticity. For these reasons, the C0-20 element is used in the remainder of the dissertation as the standard against which other modeling assumptions are judged.

5.2 Passive Constrained-Layer Damping

This study is divided into analysis of full- and partial-coverage simply supported sandwich beams. A full-coverage, three-layer, viscoelastic sandwich is very similar to the second cylindrical bending problem addressed in Section 5.1. The differences are the viscoelastic material is 3M's ISD 112, and only the base layer is pinned at the ends (the CL floats). Based on the conclusions from the previous section, the C0-20 element is used as a baseline against which to compare the Mead/Markus assumptions of Section 3.5 and the Miles/Reinhall modeling approach of Section 3.6.

5.2.1 Estimation of Modal Damping

The first step was to establish an economical indicator of how accurately damping is predicted. Four common approaches to estimating damping are

1. determine and integrate the work done by damping forces over a cycle,
2. determine the fraction of system strain energy in the viscoelastic material,
3. represent the viscoelasticity in the frequency domain and "fit" a single-degree-of-freedom oscillator to the peak of interest in a frequency-response function, or
4. represent the viscoelasticity in the time domain and extract the damping from complex eigenvalues.

Item 1 is most fundamental definition of damping [20] of an oscillator under a harmonic excitation:

$$\eta = \frac{W}{2\pi V}, \tag{5.1}$$

where

$$\begin{aligned} \eta &= \text{loss factor } = 2\zeta, \\ W &= \text{energy loss in a cycle, and} \\ V &= \text{peak potential energy stored in the system during that cycle.} \end{aligned}$$

Ungar and Kerwin in 1962 [105] made a good case for using the distribution of strain energy in Item 2 as an indicator, but the definition given by Equation (5.1) persisted in the literature until the modal strain energy (MSE) method [40] came into wide use in the early 1980's. The main appeal of the MSE method was that damping predictions come from the real eigenvectors calculated using only the real part of the VEM shear modulus.

Representing viscoelasticity in the time domain normally requires augmenting the system with "internal" or "dissipation" DOFs [104, 28, 37, 111], and this creates a potentially large system as shown in Equation (4.21). The damping for any particular mode can be found from the complex eigenvalue [60], but finding this eigenvalue is complicated by superfluous modes of the internal DOFs [107, 92, 108, 111, 47, 89, 77]. Alternatively a frequency-response function (FRF) of the system can be expressed as in Equation (4.35), and the frequency and damping can be estimated by fitting [56] a single-degree-of-freedom system to a peak, but at the cost of solving a system of equations (not augmented) for a set of frequencies in the vicinity of the peak of interest. Both of these approaches bear a substantial computational cost.

The objective in this section is to do a set trade studies looking at different full and partial coverage combinations of base, viscoelastic, and constraining layers, and this task would be much simpler if modal strain energy was a good indicator of modeling accuracy. Test this by comparing damping predicted by the MSE method using the only the real part of the shear modulus and by curve-fitting an FRF using the six-term representation from Table 4.1 and Equations (4.37). The test base beam is 5.0 x 1.0 x 0.125 with a damping treatment covering the middle 25% of the beam as shown in Figure 5.2. This case was chosen since the MM predictions match the higher order predictions well for two of the cases and poorly for the other two. The four test cases are the four combinations of

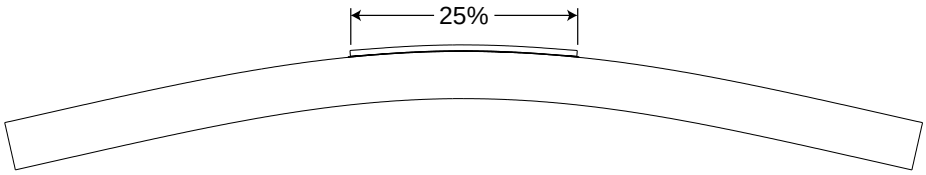

Figure 5.2: Fundamental mode of beam with 25%-coverage damping treatment

constraining layer thicknesses of 0.010 and 0.125 inches and VEM thicknesses of 0.005 and 0.050 inches. Figure 5.3 shows the loss for the first mode is predicted poorly for cases 1 and 2 (with respect to the higher order elements) and well for cases 3 and 4. The point of this figure is that accuracy, or inaccuracy as the case may be, predicted with the full viscoelasticity model is mirrored by the modal strain energy. A side point here is that the MSE method works very well for cases 3 and 4, where the damping levels are low, but it overpredicts in cases 1 and 2 where the levels of damping are higher. This is to be expected, as discussed by Morgenthaler [63]. Even though the real-valued MSE analysis overpredicts the higher levels of damping, the accuracy of predictions using the MM assumptions with respect to higher order analyses are well represented. Having established this, many of the studies presented subsequently will take advantage of the simplicity that a real-valued analysis provides.

5.2.2 Full-Coverage Damping Treatments

Covering the entire surface of the beam with a damping treatment is the most straight-forward approach, though studies cited in Section 5.2.3 have shown that partial coverage can be better. In many practical situations, full coverage is a luxury prevented by various restrictions (space, weight, managers). Nonetheless, the configuration is worth studying, especially since the modeling assumptions proposed by Kerwin and later the MM model were developed for such structures.

The beams analyzed were simply supported (base layer only!), and, without loss of generality, only one symmetric half was analyzed. At this point I switch from Pagano's plane strain assumption to plane stress in order to compare with experiments discussed in Chapter 6. The change in boundary conditions means that Pagano's test cases no longer apply, so the question becomes "what should be used at the baseline result?" The strategy adopted was to demonstrate convergence of meshes

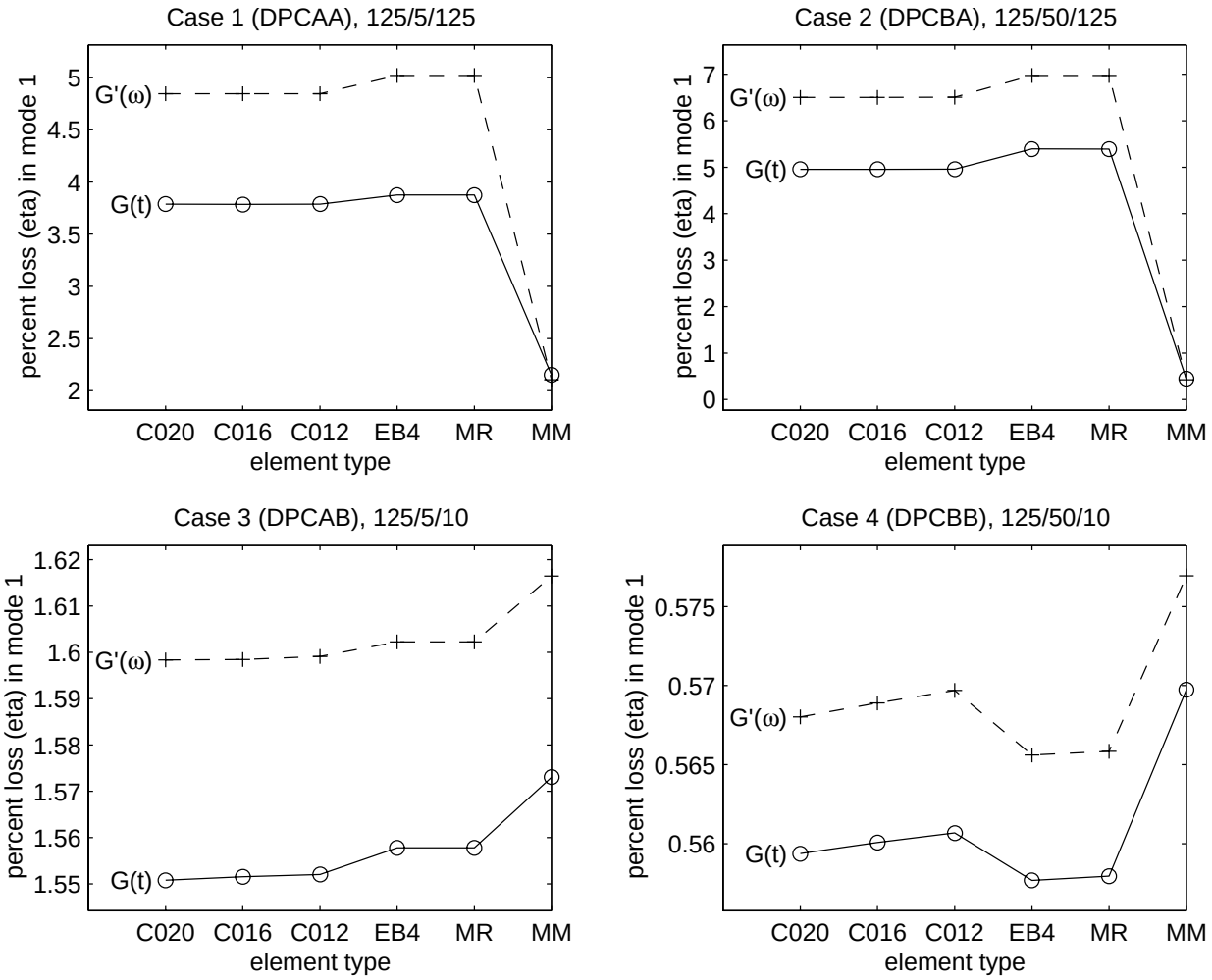

Figure 5.3: Predictions of modal loss by real and complex analyses for 5-inch-long beam with 25% coverage

using the C0-20 higher order element and use that as a bases for comparisons. Figure 5.4 is a plot of the modal strain energy (MSE) in mode 1 versus number of degrees of freedom for cases 1 – 4 in Table 5.1. The four modeling approaches studied are listed in Table 5.8. A dashed line is drawn

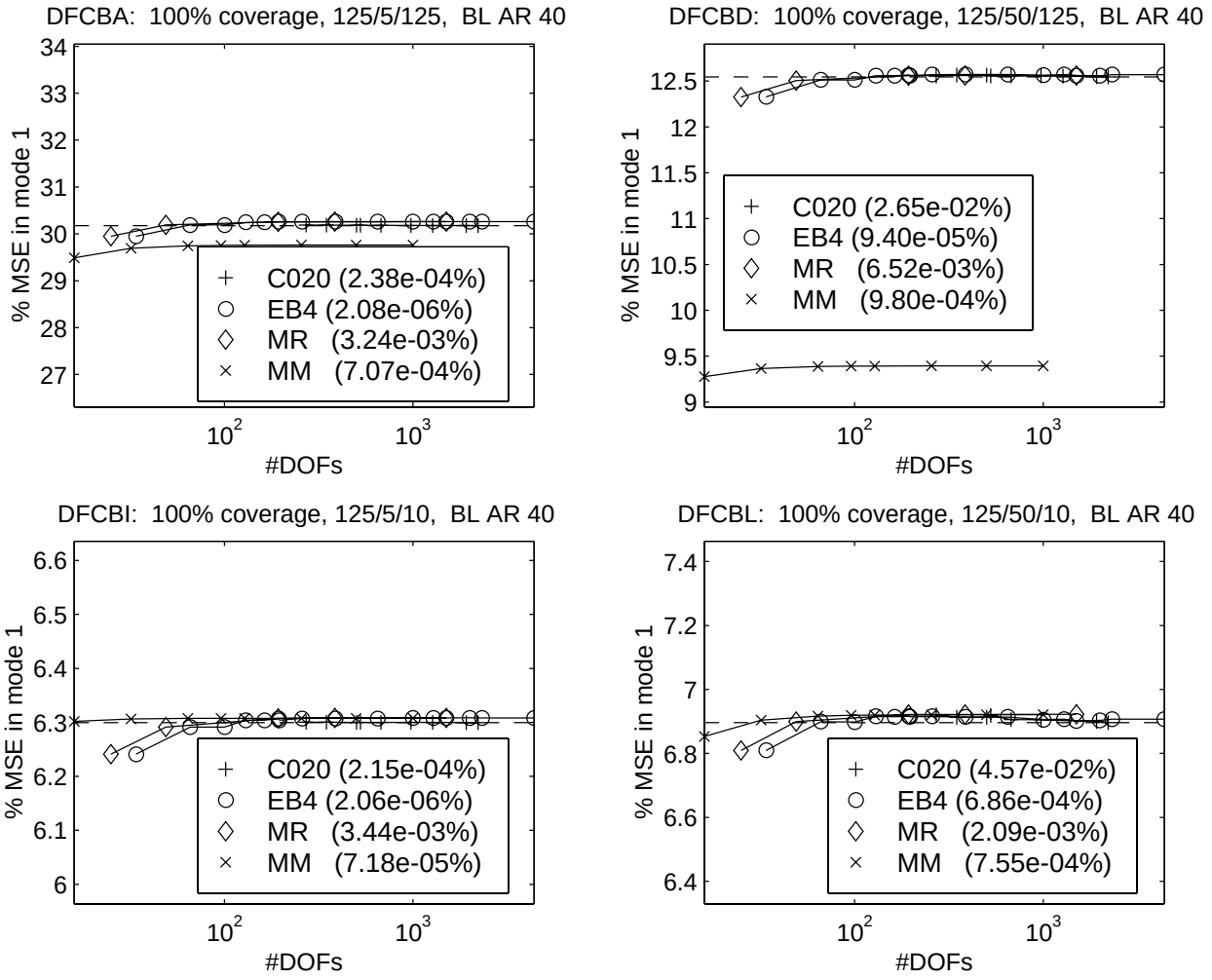

Figure 5.4: Convergence of MSE in mode 1 of 5-inch-long beams using MM and higher order elements

at the "converged" value of the C0-20 mesh, and the percent change over the last two refinements is given for each element in the legend. The key observations from these four plots are

1. all of the meshes have converged to within "engineering" accuracy based on percent changes on the order of 10^{-2} or small for successive mesh refinements,

2. the EB4 prediction are very good for a relatively low number of DOFs,

Table 5.8: Modeling approaches studied for full and partial coverage

label	description
C020	all layers modeled with the 20-node C^0 element
EB4	Euler-Beam facesheets and multiple C0-4 elements through VEM thickness
MR	Miles/Reinhall: EB facesheets; single C0-4 through VEM thickness
MM	Mead/Markus: EB facesheets with equal transverse displacements and a single C0-4 element through the VEM thickness

3. the MR predictions as as good as EB4 (more than one element through the VEM thickness),

4. the MM predictions are very good for relatively thin CLs, and

5. the MM predictions are much better for the thick CL with thin VEM that for the same CL with thick VEM.

These results are as expected. Figure 5.5 is a similar plot for longer beams (cases 5–8), and it shows that the MM assumptions are very good for the four cases shown here. This also is expected since it is structures like these for which the MM assumptions were designed to be accurate.

Poisson's ratio was assumed to be 0.49 in the VEMs reported above, but this is only an engineering guess. Next investigate the effect that uncertainty in Poisson's ratio has on these predictions. The meshes used for each element have converged to within reasonable engineering accuracy. Figures 5.6 and 5.7 give the modal strain energy in the first mode versus Poisson's ratio in the VEM for the two lengths of beams. The legend on each graph gives the percentage change in the MSE between assumptions of 0.3 and 0.4999. The effects are more pronounced for the shorter beam in Figure 5.6, where the variation is at most 6.5% for case DFC2. As expected, all of the cases show that the MSE predictions change very little under the MM assumptions because the strain field within the VEM is primarily shear since the facesheets are constrained to remain parallel to one another. The fact that they change at all under the MM assumptions is due to differences in calculating Young's modulus from the shear modulus using $E = 2\,(1+\nu)\,G$. The results for the longer beam (Figure 5.7) show the variation with Poisson's ratio to be negligible for the cases studied. This is intuitive since long, full-coverage beams tend to be well represented by the MM assumptions, and as such the VEM strain must be dominated by shear.

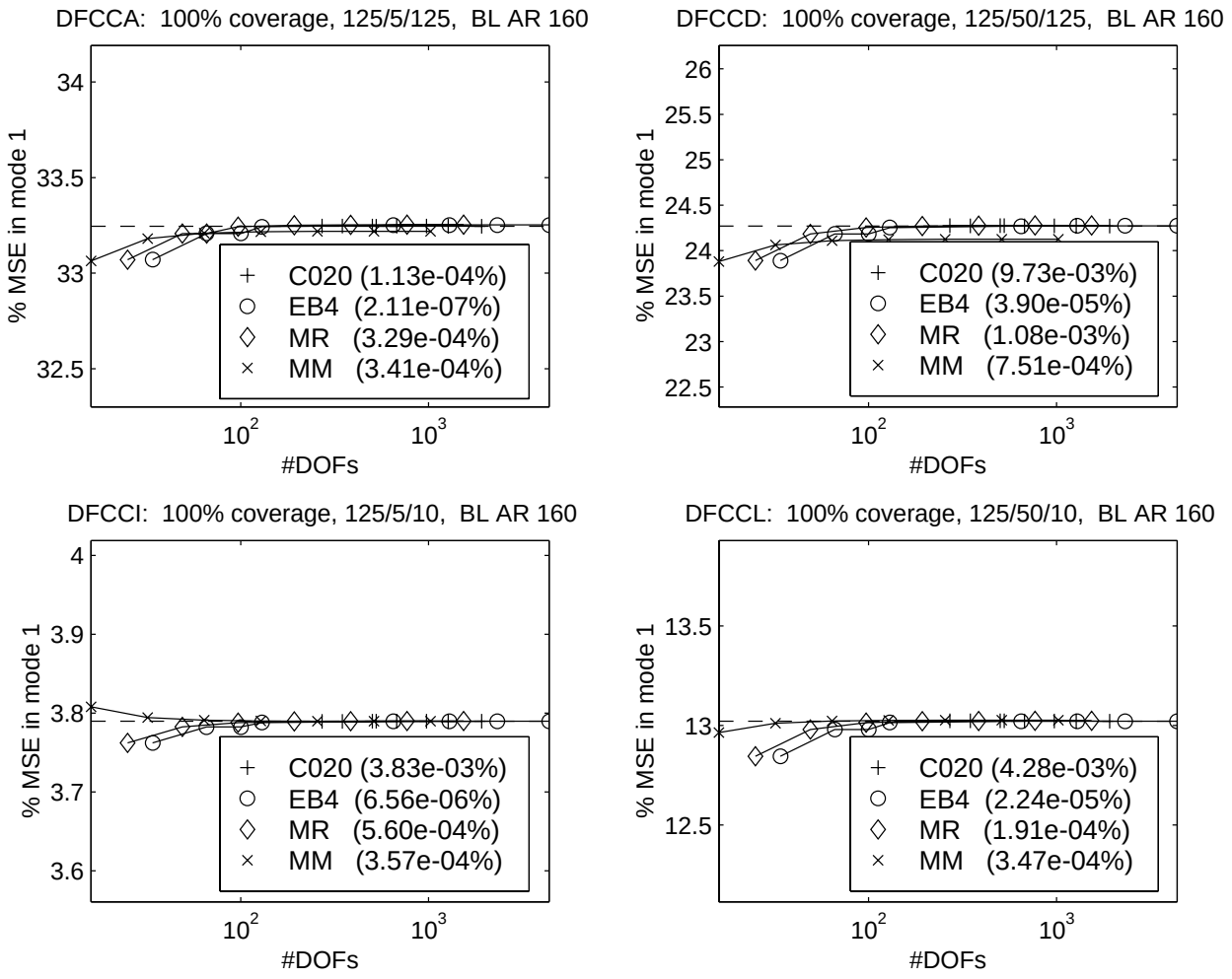

Figure 5.5: Convergence of MSE in mode 1 of 20-inch-long beams using MM and higher order elements

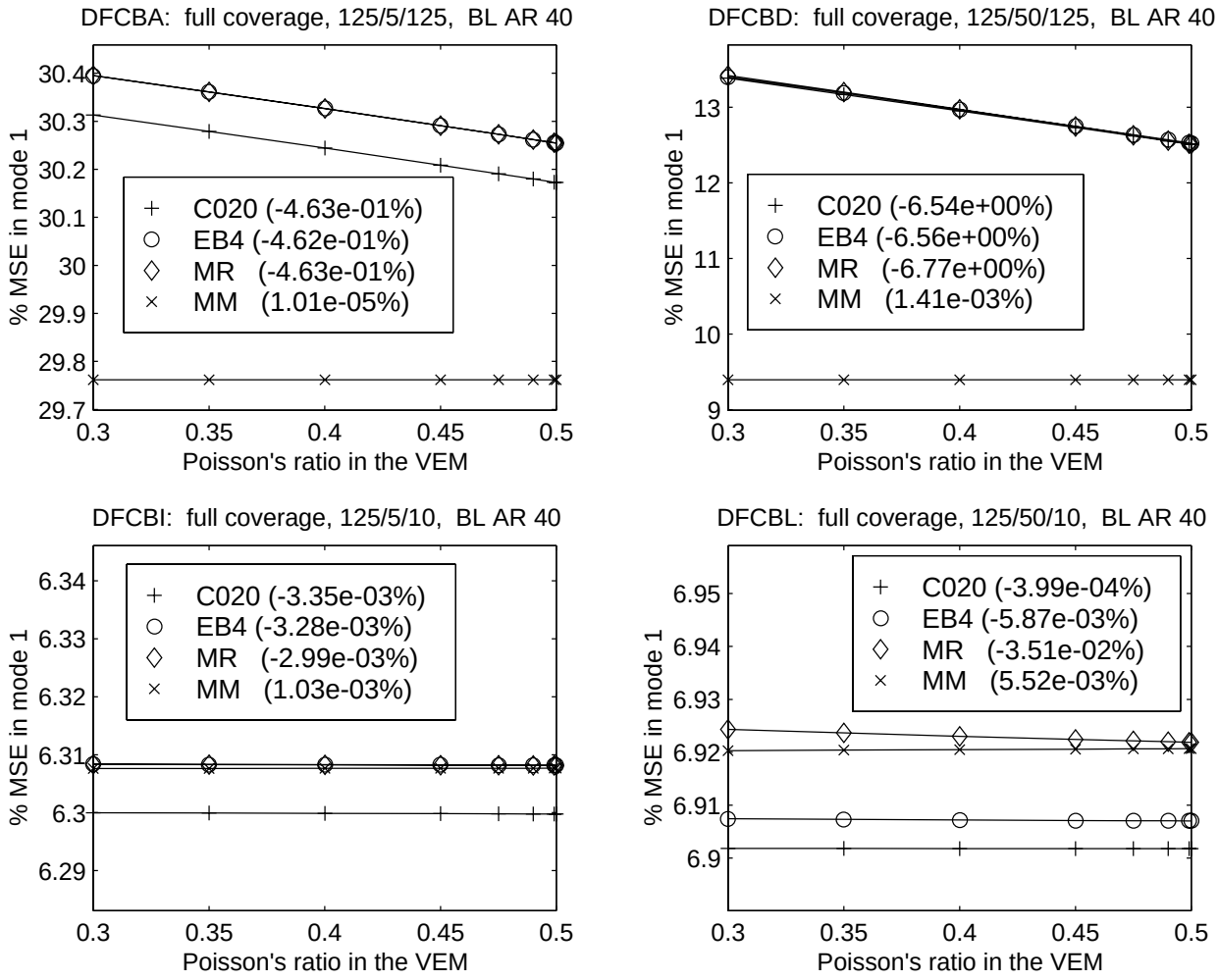

Figure 5.6: Variation with Poisson's ratio of predictions of MSE in mode 1 of 5-inch-long beams using MM and higher order elements

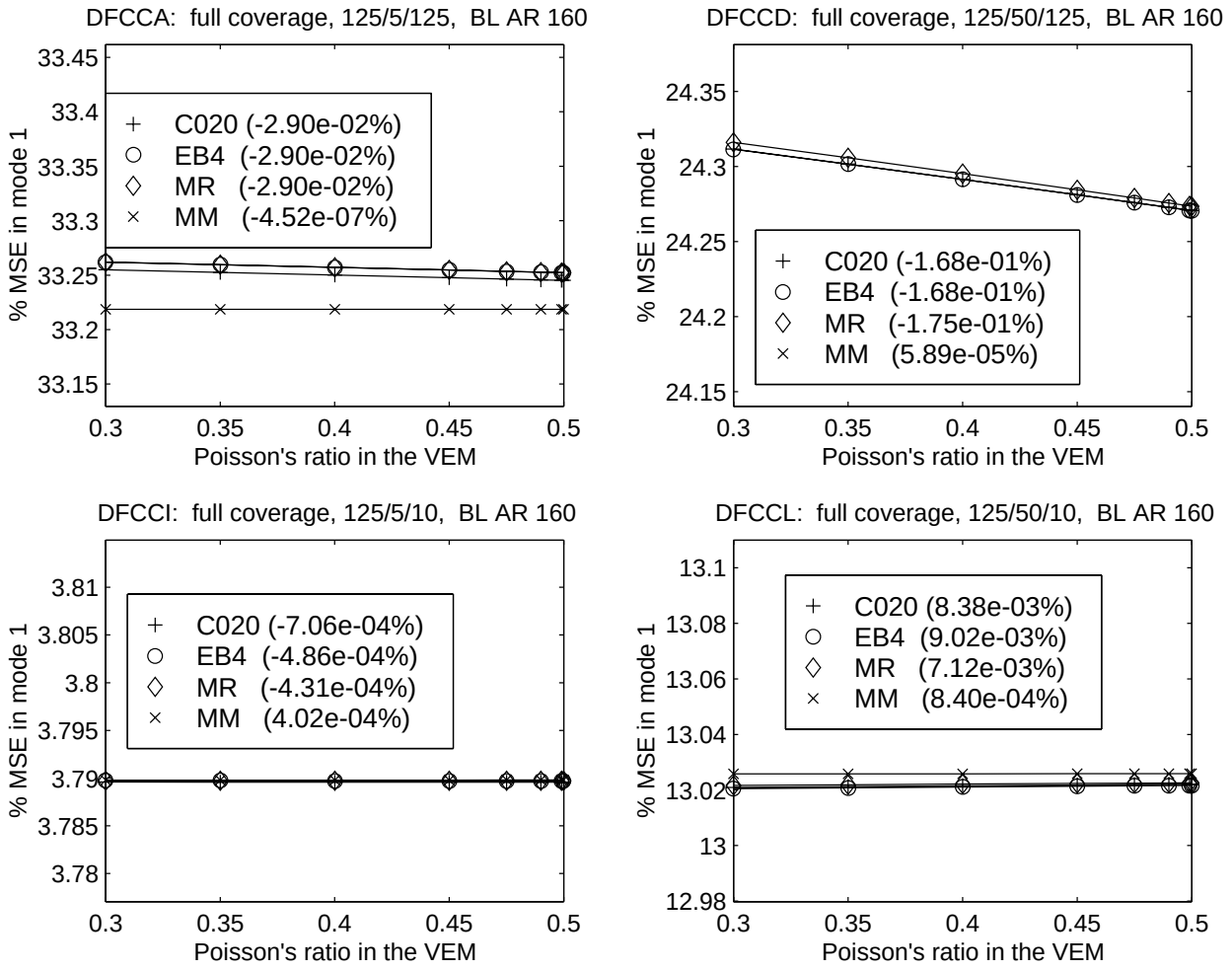

Figure 5.7: Variation with Poisson's ratio of predictions of MSE in mode 1 of 20-inch-long beams using MM and higher order elements

5.2.3 Partial-Coverage Damping Treatments

There are many situations in industry where the engineer's challenge is to maximize the damping added to a structure when given only a partial "footprint," i.e., area of host structure available for a damping treatment. Several researchers have reported optimal partial-coverage configurations that outperform full-coverage treatments in some situations, as summarized in Section 2.1.2. However, if the space available for the damping treatment is fixed a priori, the designer can only work with the VEM and constraining layer to maximize damping added. Figure 5.8 shows the percentage of modal strain energy in the first mode of a 5-inch-long, 0.125-inch-thick (unit width), aluminum beam with 5 mils of the VEM ISD 112 plotted against the ratio of the thicknesses of the base and constraining layers for full and partial coverage. Modal strain energy is maximized for the full-

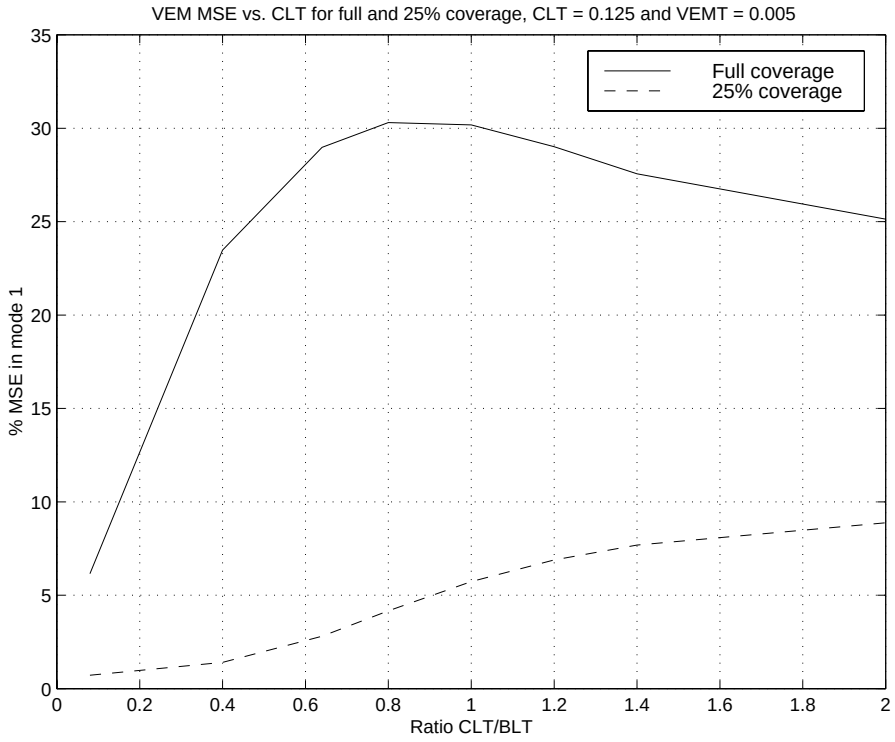

Figure 5.8: Example variation of MSE in first mode for full- and 25%-coverage damping treatments

coverage case when the constraining layer is approximately the same thickness as the base layer. This well-known "rule of thumb" for damping designers has been documented by Nashif *et al.* [67] and Rao [82]. The other line is for a 25% partial-coverage treatment as shown in Figure 5.2, and

the results suggest that the stiffer constraining layer the better the damping treatments. Obviously it is would not be physical (or linear) to let the thickness of the constraining layer become many times thicker that the base layer, but the point is there is not some optimum thickness much less than the thickness of the base layer.

The test cases of Table 5.1 were analyzed with varying percentages of coverage of the base beam. The partial coverage is symmetric about the center of the beam, so only half of each beam is analyzed. Figure 5.9 is both a summary and preview of the data presented in this section. The graphs show the percent difference between what converged meshes of MM and C0-20 elements predict for the VEM strain energy in the first mode. The values at 100% match the data presented

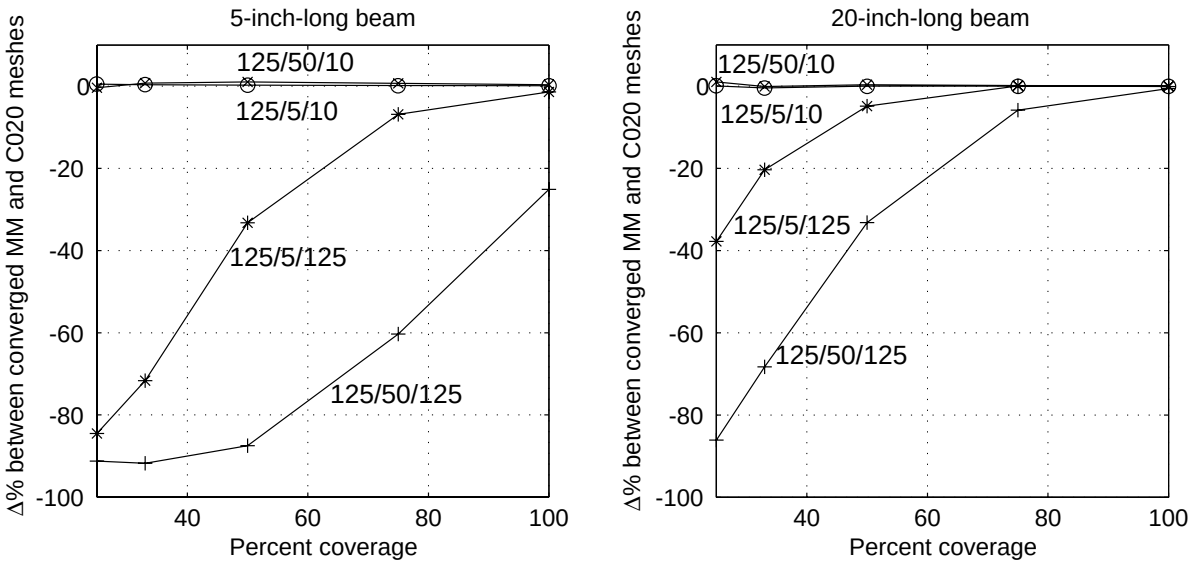

Figure 5.9: Error in Mead-Markus predictions vs. percent coverage for eight beam geometries

in Figures 5.4 and 5.5 for full coverage. The trends shown for full coverage are repeated here — the MM assumptions are best for flexible (thin) constraining layers on a stiff (thin) VEM and worst for stiff (thick) constraining layers on a soft (thick) VEM. Additionally, observe that for the 125-mil-thick constraining layers the error in the MM predictions increases dramatically as the percent coverage decreases. The performance for the MR and EB4 meshes is summarized in Figures 5.10 and 5.11. The trend is similar to the MM results, but the errors are much smaller. In fact, both the MR and EB4 mesh strategies predict essentially the same modal strain energy in the VEM core that the higher order C0-20 predicts. The EB4 meshes differ from the MR meshes only in that

there are typically between 2 and 8 elements through the VEM thickness instead of just 1.

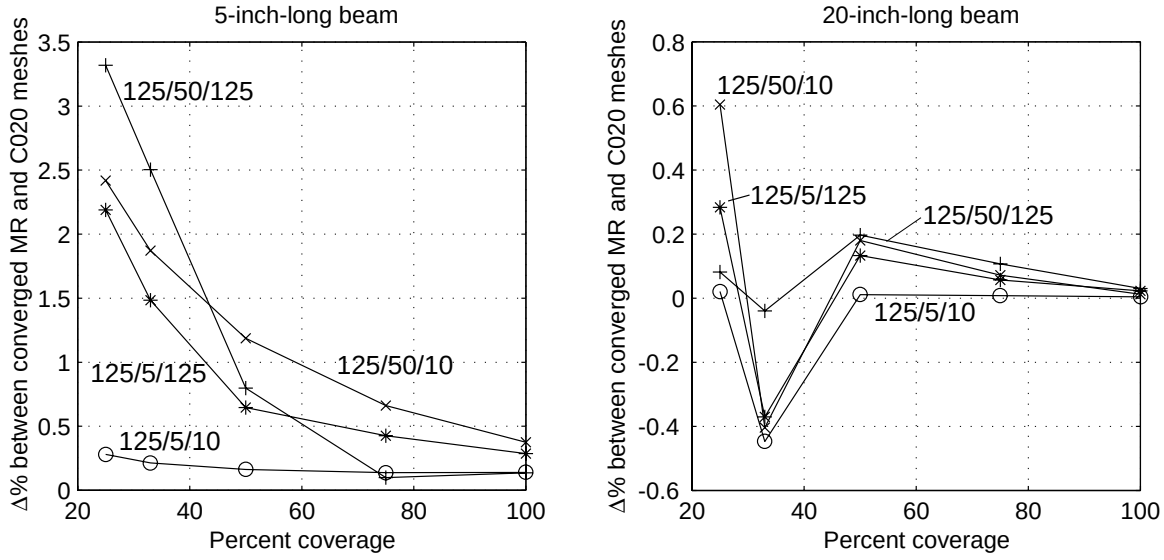

Figure 5.10: Error in Miles-Reinhall predictions vs. percent coverage for eight beam geometries

The meshes for the partial coverage treatments converged with success similar to those for the full coverage treatments, as typified by Figures 5.12 and 5.13.

Overall, the trends and conclusions for partial coverage are similar to those for the full-coverage cases:

- the MM assumptions work best for long, thin constraining layers on thin layers of viscoelastic,
- the EB4 and MR implementations are very good, and
- the meshes using the higher order C0-20 elements offer no discernible advantage over the EB4 and MR approaches.

The consequences of uncertain Poisson's ratio (ν) are more pronounced for the partial-coverage cases than for the full-coverage. Figures 5.6 and 5.7 shows that the MSE in the VEM essentially varies linearly with Poisson's ratio. Thus it is sufficient to plot the percentage difference between the VEM MSE predicted for $\nu = 0.3$ and $\nu = 0.4999$, as shown in Figure 5.14 for the standard test cases. The values for 100% (full) coverage in the plot correspond to the percent variations shown

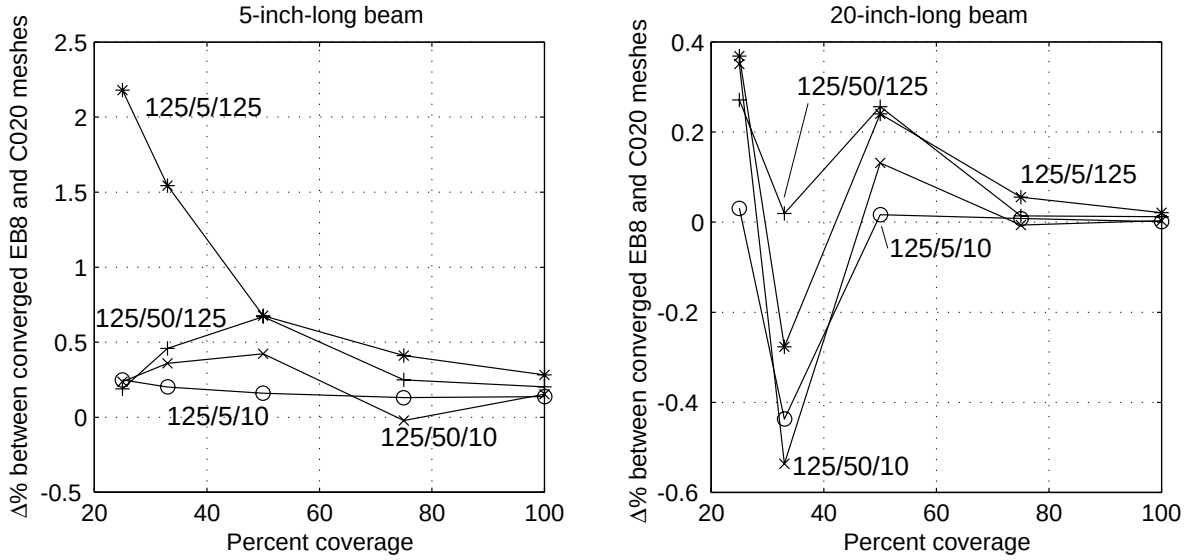

Figure 5.11: Error in EB4 predictions vs. percent coverage for eight beam geometries

in Figures 5.6 and 5.7 for the C0-20 element. The interesting point is how much variation with Poisson's ratio is seen in the MSE predictions as the coverage decreases. For the 5-inch-long beam, the 125/50/125 case has two zero crossings, implying that there are two percentages of coverage for which the sandwich is insensitive to changes in Poisson's ratio. To understand this better, break down the strain energy by the strain components as follows. From Equations (3.9) and (3.22), the strain energy over an element is for the planar problem is

$$\begin{aligned} U^e &= \frac{1}{2}\int_{\Omega^e} \{\epsilon\}^T [Q] \{\epsilon\} \, d\Omega^e \\ &= \frac{1}{2}\int_{\Omega^e} \begin{Bmatrix} \epsilon_1 \\ \epsilon_3 \\ \gamma_{31} \end{Bmatrix}^T \begin{bmatrix} Q_{11} & Q_{13} & 0 \\ Q_{13} & Q_{33} & 0 \\ 0 & 0 & Q_{55} \end{bmatrix} \begin{Bmatrix} \epsilon_1 \\ \epsilon_3 \\ \gamma_{31} \end{Bmatrix} d\Omega^e \end{aligned} \tag{5.2}$$

From Equation (3.21) subdivide the strain-displacement matrix $[B]$ as

$$\{\epsilon\} = [B]\{a\} = \begin{bmatrix} -B_1- \\ -B_3- \\ -B_5- \end{bmatrix} \{a\} \tag{5.3}$$

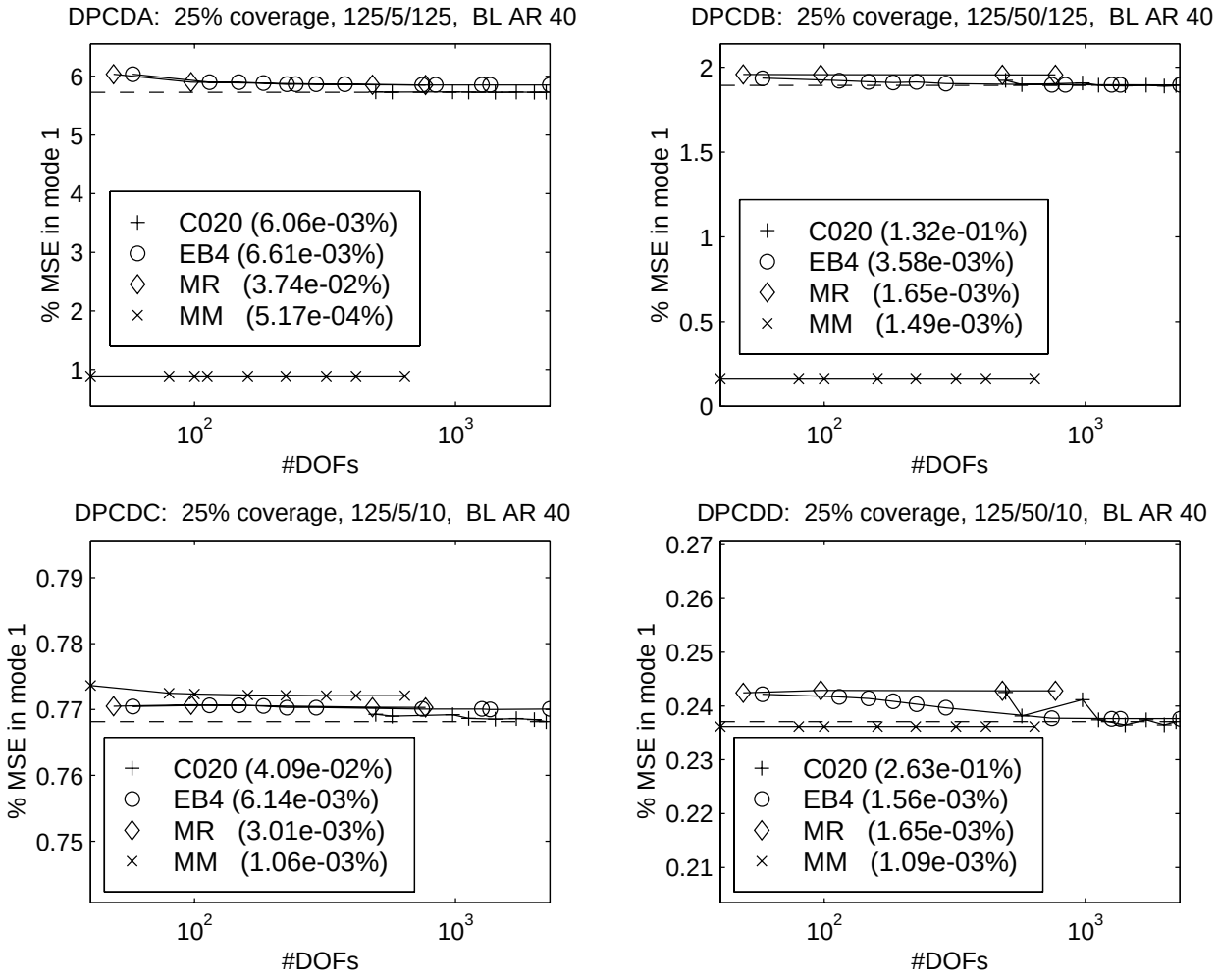

Figure 5.12: Convergence of VEM MSE for 25% coverage of the 5-inch-long beam

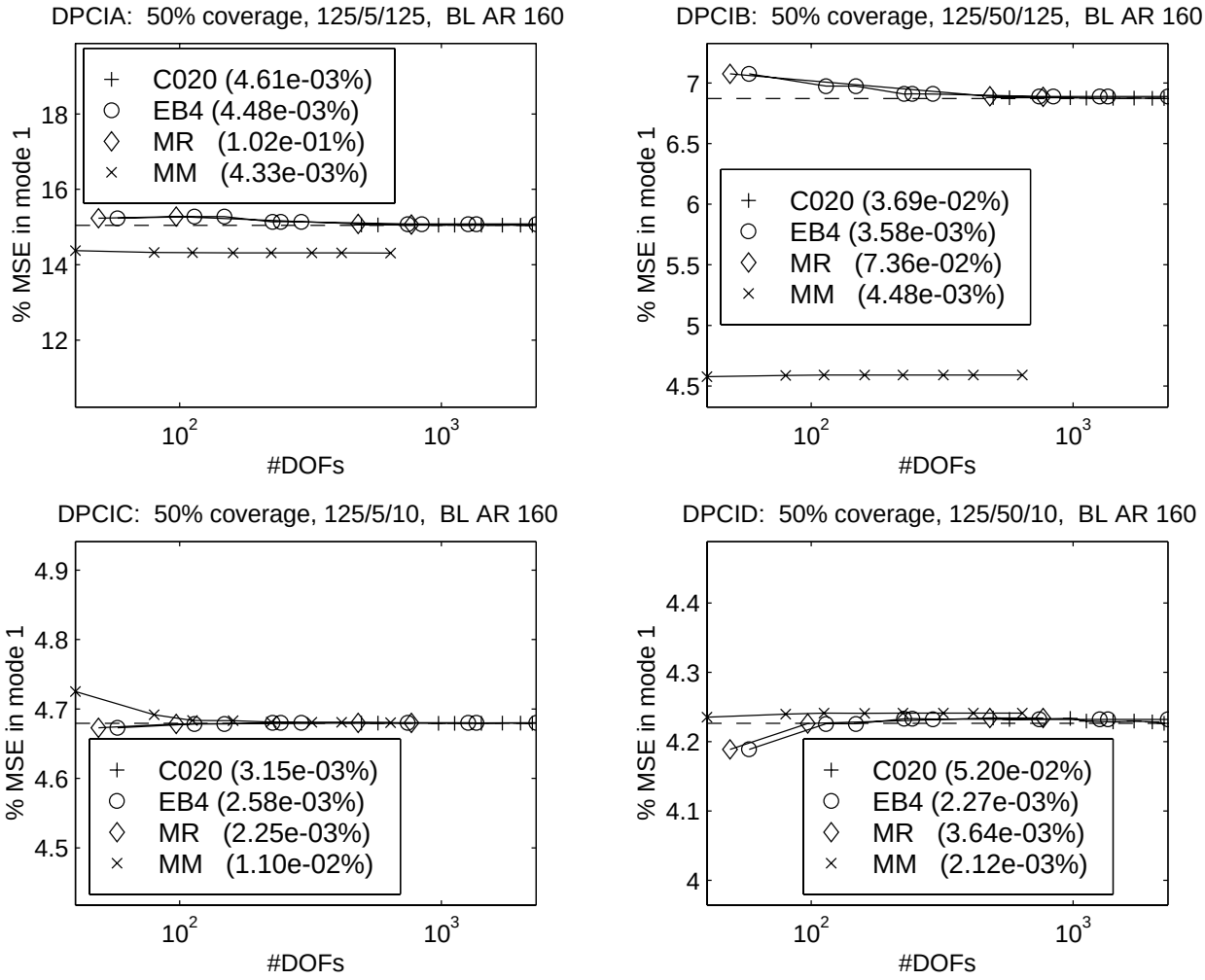

Figure 5.13: Convergence of VEM MSE for 50% coverage of the 20-inch-long beam

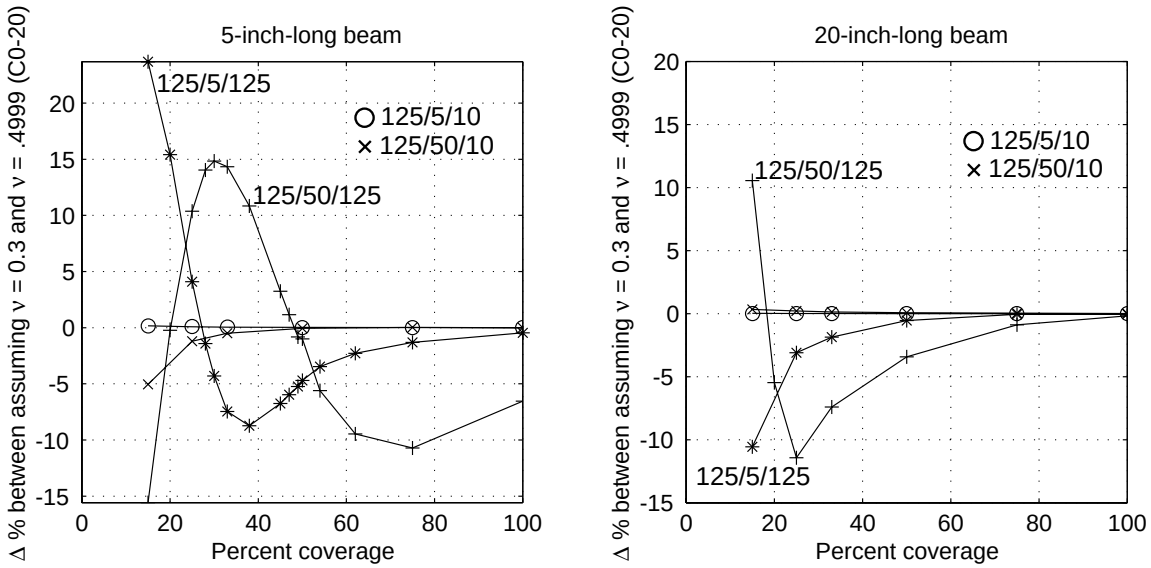

Figure 5.14: Difference in MSE predicted with C0-20 element assuming Poisson's ratio $\nu = 0.3$ and $\nu = 0.4999$ vs. percent coverage

Substituting Equation (5.3) into (5.2) yields

$$\begin{aligned} U^e &= \frac{1}{2}\{a\}^T \left[\int_{\Omega^e} \left(B_1^T Q_{11} B_1 + 2B_1^T Q_{13} B_3 + B_3^T Q_{33} B_3 + B_5^T Q_{55} B_5\right) d\Omega^e\right] \{a\} \\ &= \{a\}^T \left[k_{11}^e + k_{13}^e + k_{33}^e + k_{55}^e\right] \{a\} \\ &= U_{11}^e + U_{13}^e + U_{33}^e + U_{55}^e \end{aligned} \tag{5.4}$$

These represent a breakdown of strain energy by strain component. Note that the second term is not necessarily positive definite, while the sum of all the strain energy components is. Figures 5.15 through 5.18 show the various subcomponent of the VEM MSE versus percent coverage calculated assuming Poisson's ratios of 0.3 and 0.4999. The VEM MSE is dominated by shear strain, labeled SE55, and transverse normal (i.e., through the thickness) strain, labeled SE33. One would expect beams where the strain energy is dominated by shear strain to be insensitive to the Poisson's ratio used to calculate the "other" material property. What's more, such a situation should be well represented by the MM assumptions. This can been seen especially for the thin-CL cases for the long beam. The MM assumptions breakdown in the thick-CL cases where the dominant component of the total MSE switches from transverse normal to shear as coverages goes from 0 to 100 percent. The components of the MSE are nearly the same for either value of Poisson's ratio, and this helps

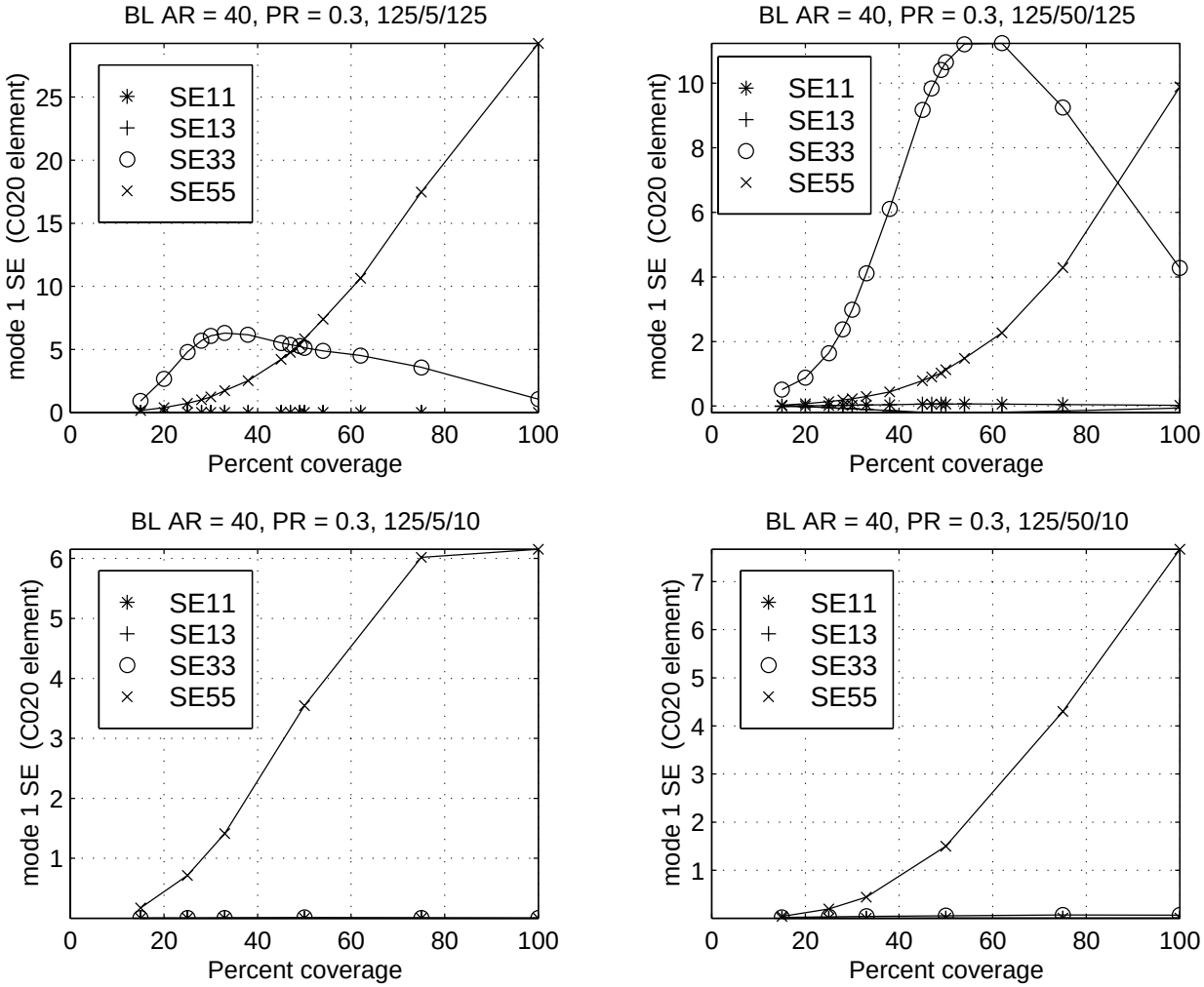

Figure 5.15: MSE components in mode 1 vs. percent coverage 5-inch-long beam and $\nu = 0.3$

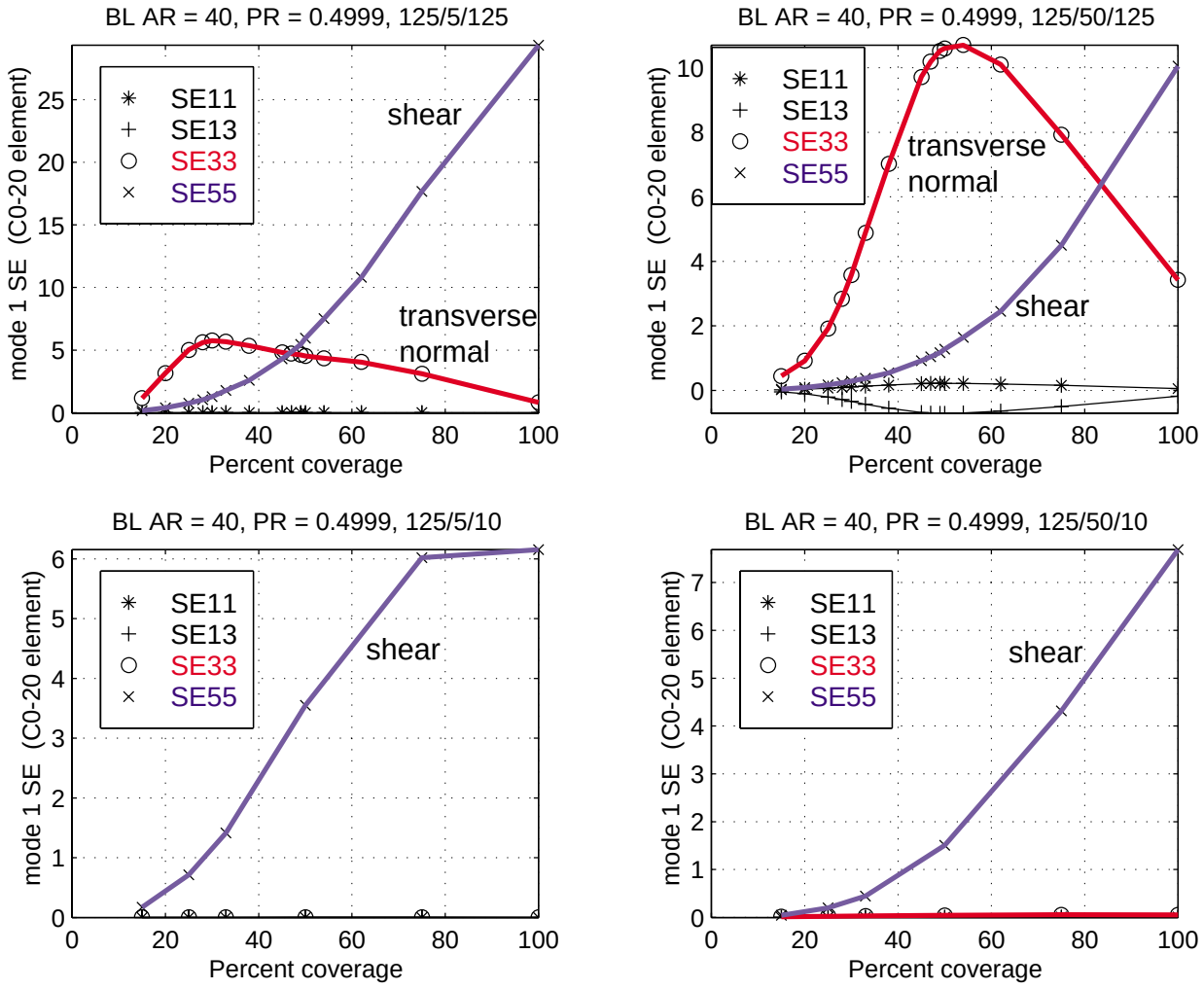

Figure 5.16: MSE components in mode 1 vs. percent coverage 5-inch-long beam and $\nu = 0.4999$

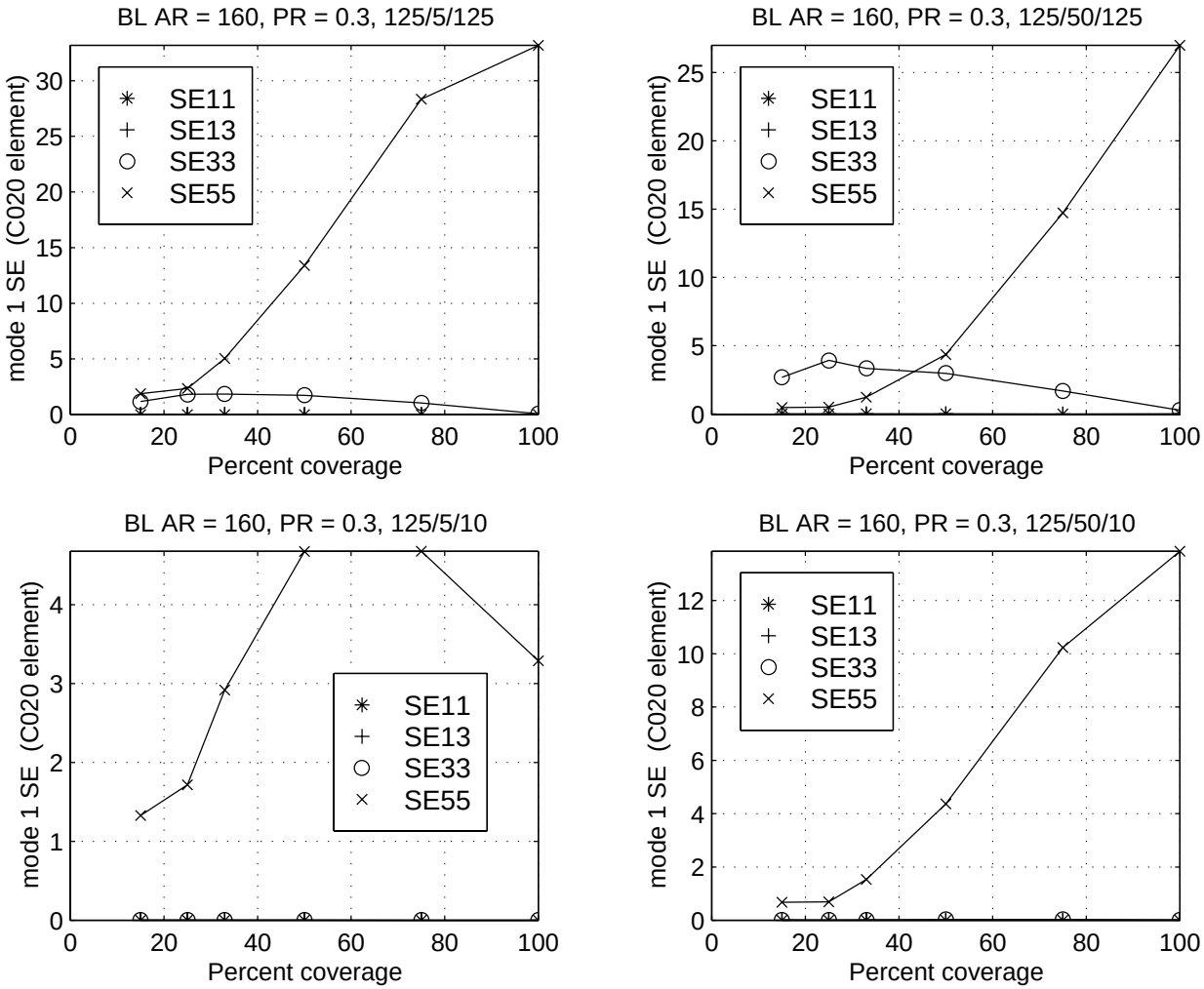

Figure 5.17: MSE components in mode 1 vs. percent coverage 20-inch-long beam and $\nu = 0.3$

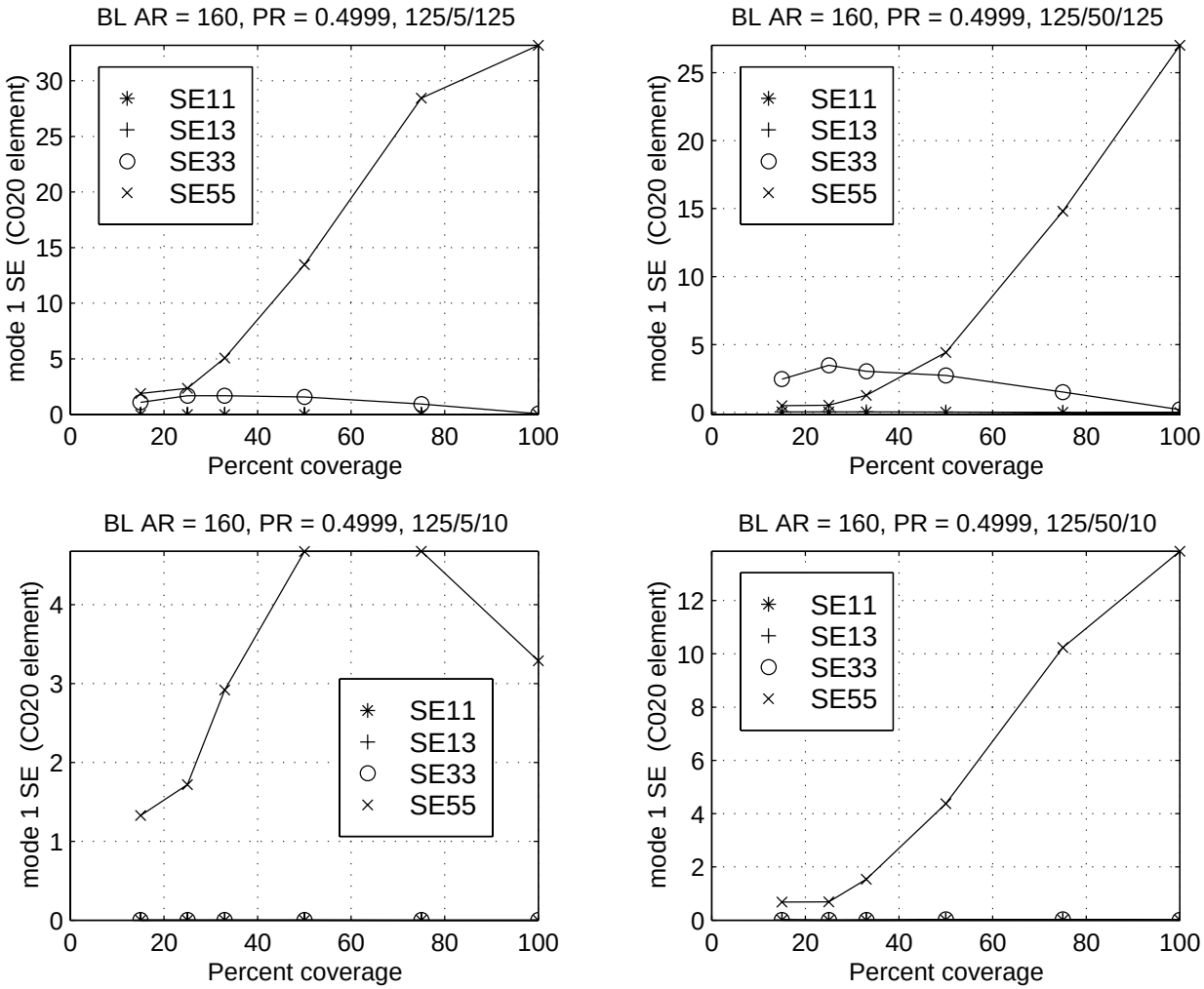

Figure 5.18: MSE components in mode 1 vs. percent coverage 20-inch-long beam and $\nu = 0.4999$

show that the zero crossings in Figure 5.14 are not critical values where suddenly transverse normal effects are negligible. Rather they are merely situations where the MSE components for ν=0.3 and ν=0.4999 add to the same number.

Figure 5.14 shows the effect of varying Poisson's ratio as predicted with the higher order C0-20 element. Figures 5.19 and 5.20 show that the lower order EB4 and MR modeling approaches predict essentially the same results. The MM model, predictably, presents a different result as shown in

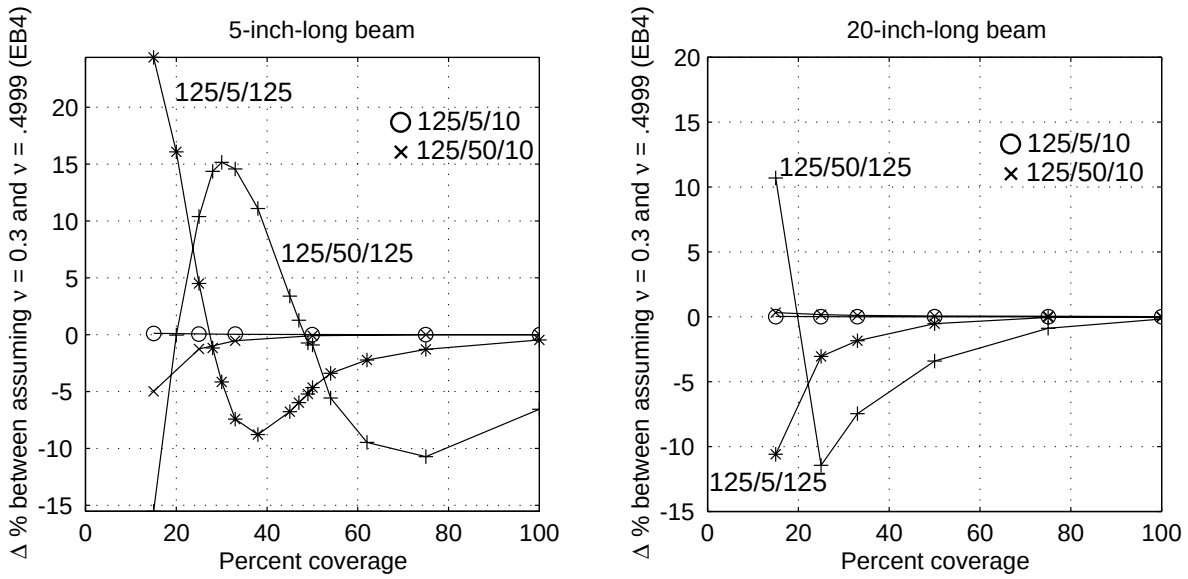

Figure 5.19: Difference in MSE predicted with EB4 element assuming Poisson's ratio $\nu = 0.3$ and $\nu = 0.4999$ vs. percent coverage

Figure 5.21. The contention throughout this analysis has been that the VEM shear modulus is the quantity available from tests, so Young's modulus is inferred by assuming Poisson's ratio. The fact that there is any variation at all with Poisson's ratio in Figure 5.21 is due to the effect of a changing Young's modulus on the strain energy in the 1-1 direction, and Figures 5.15 through 5.18 show the component to have little influence.

Much of the data has been relative, so conclude this section by looking at the actual magnitudes of MSE predicted (see Figure 5.22). The general trend for the cases studied here is more coverage is better, but again there are many publications that report maximizing damping for less than full coverage (see Section 2.1.2). The point here is not which option is better; the point is what level of analysis is needed when partial coverage is the only option.

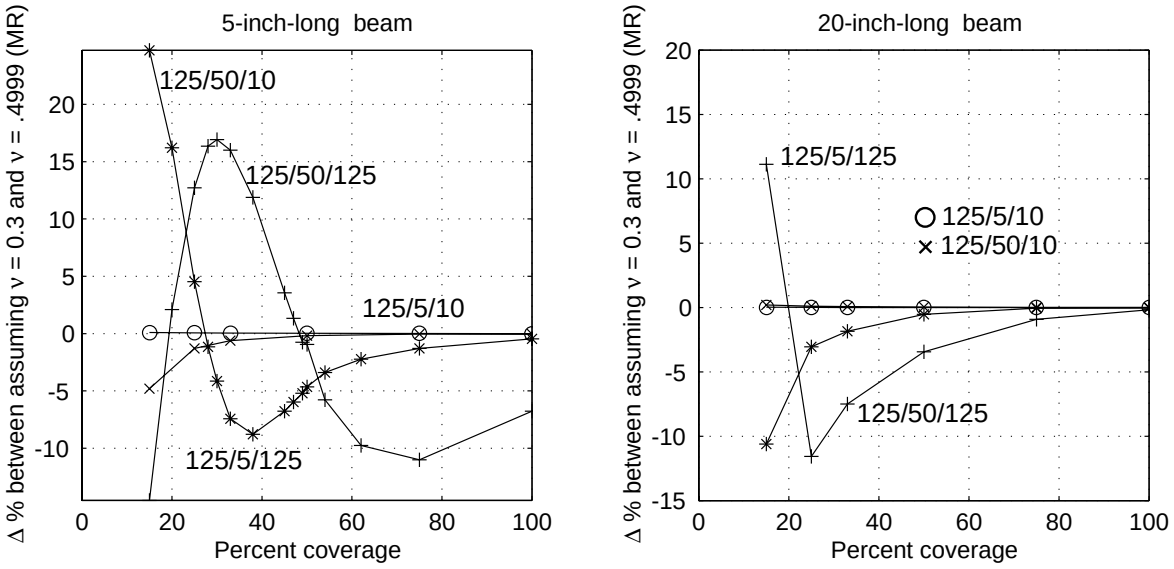

Figure 5.20: Difference in MSE predicted with Miles-Reinhall element assuming Poisson's ratio ν = 0.3 and $\nu = 0.4999$ vs. percent coverage

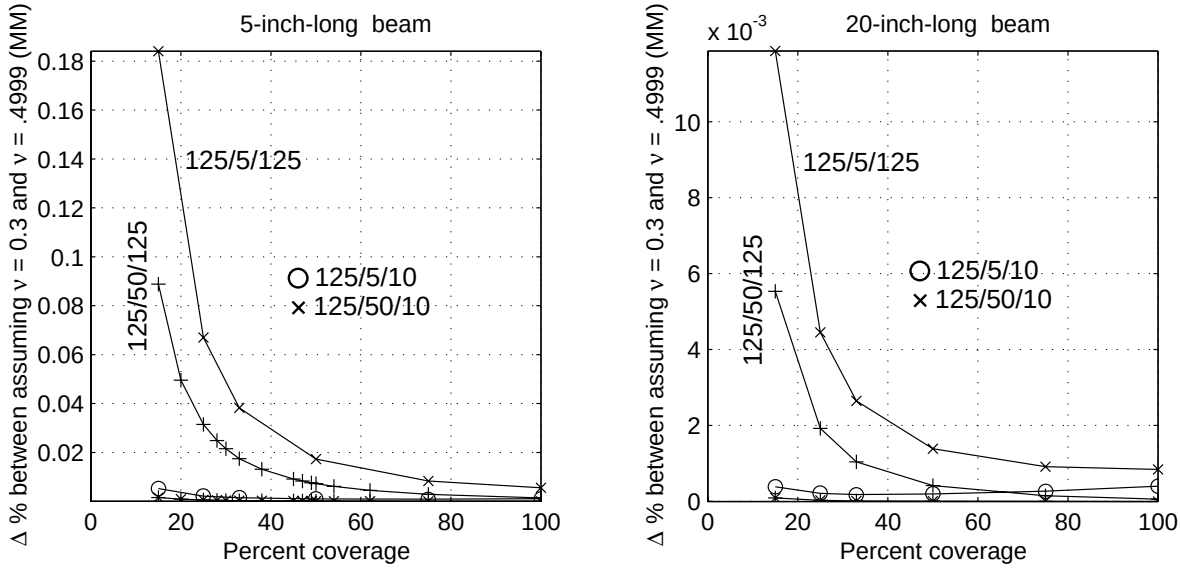

Figure 5.21: Difference in MSE predicted with Mead-Markus element assuming Poisson's ratio ν = 0.3 and $\nu = 0.4999$ vs. percent coverage

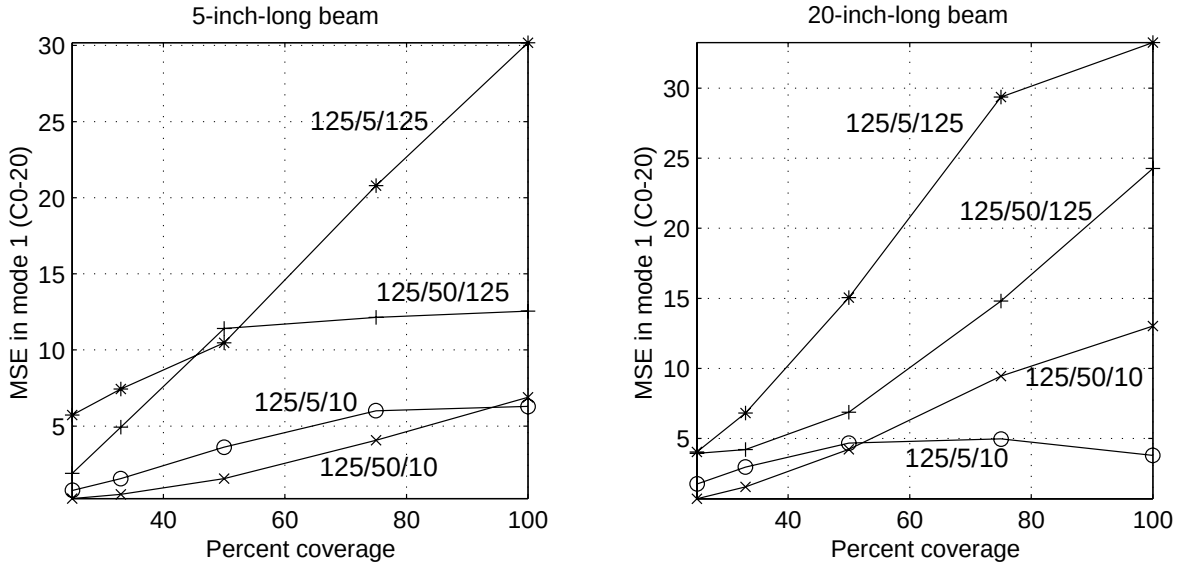

Figure 5.22: Modal strain energy predicted for mode 1 vs. percent coverage using C0-20 elements

5.3 Active Constrained-Layer Damping

The purpose of the constraining layer is to *direct* strain energy into the viscoelastic layer where it can be dissipated. Plump and Hubbard [79] introduced the idea of increasing this energy with an active constraining layer. Most of the publications in this area use a piezoelectric crystal (PZT) as the constraining layer. The typical PZT is thin, on the order of 10 mils thick, so when used as a purely passive constraining layer its performance should be similar to that of the 10-mil-thick aluminum constraining layer in Section 5.2. By the same reasoning, one would expect the Mead and Markus (MM) model to predict the damping accurately for most cases. Of the eight sets of thickness geometries listed in Table 5.1, only the 10-mil-thick constraining layer on the 5-inch-long beam are presented, since they were shown previously to be the worse-case scenarios. One key question to be answered in this section is whether these trends for a passive constraining layer hold for an *active* constraining layer. The second key question is whether PZT actuation effects the ability of the MM assumptions to predict the closed-loop damping.

A voltage applied to a PZT induces a strain, and strains due to PZT actuation, temperature change, crystal growth, shrinkage and so on are treated as initial strains in the finite element formulation. Calling these *eigenstrains* ϵ_0, the constitutive relationship for a linear elastic material can be written

[112]

$$\{\sigma\} = [Q]\left(\{\epsilon\} - \{\epsilon_0\}\right) \tag{5.5}$$

Next write Equation (3.10) in matrix form and combine with Equation (5.5).

$$\begin{aligned}\delta U &= \int_{\Omega} \{\delta\epsilon\}^T \{\sigma\}\, d\Omega = \int_{\Omega} \{\delta\epsilon\}^T [Q]\left(\{\epsilon\} - \{\epsilon_0\}\right) d\Omega \\ &= \int_{\Omega} \left(\{\delta\epsilon\}^T [Q]\{\epsilon\} - \{\delta\epsilon\}^T [Q]\{\epsilon_0\}\right) d\Omega \end{aligned} \tag{5.6}$$

Substituting the finite element strain-displacement relationship from, for instance, Equation 3.21, the variation in strain energy over an element can be written

$$\delta U^e = \left\{\delta u_p^e\right\}^T \underbrace{\int_{\Omega^e} [B]^T [Q][B]\, d\Omega^e}_{k^e} \left\{u_p^e\right\} - \left\{\delta u_p^e\right\}^T \underbrace{\int_{\Omega^e} [B]^T [Q]\{\epsilon_0\}\, d\Omega^e}_{f_{pzt}^e}, \tag{5.7}$$

where k^e is the element stiffness matrix as in Equation (3.27) and f_{pzt}^e is the PZT load vector.

The presence of eigenstrains makes the use of strain energy as an indicator of damping problematic. (strain energy is no longer positive definite). This means that the time-dependent properties of the viscoelastic material must be included to determine the damping. The two straightforward choices for determining closed-loop damping are either estimating parameters from a closed-loop frequency-response function (FRF) or solving a complex eigenvalue (CEV) problem. The models needed to do these operations differ greatly in size, however.

A CEV solution requires that the full system be augmented with internal variables in first-order form of Equation (4.21), and from this the damping in the first mode can be found from the corresponding complex eigenvalue. In addition to doubling the size of the physical system, an internal DOF must be added for each physical DOF connected to a VEM element for each term in the Prony series describing the VEM. If N is the number of DOFs in the physical system, N_v is the number of VEM DOFs, and n_p is number of terms in the prony series, the augmented system size is $2N + n_p N_v$. This provides good motivation for describing the VEM with as few terms as possible. A subtle computational issue in finding the desired complex eigenvalue is all the dummy eigenvalues introduced by the internal variables. Yae *et al.* [107, 108], Slater [92], Yiu [111], Lam

[47], Salmanoff [89], and Park *et al.* [77] offer strategies for condensing many of these "dissipation" DOFs out of the problem.

There are some advantages to inferring the damping from a frequency-response function. First, the system size is not increased by adding internal variables, as shown in Section 4.2, so the time-dependent material properties can be represented by any number of Prony series terms without penalty. Second, the engineer gets a visual feeling for the modal damping from the shape of the peak. Two disadvantages are that a parameter-estimation routine must be implemented to extract the damping, and the system must be solved for each frequency on the FRF. For simplicity, feedback was modeled between the transverse velocity at the center of the beam and the PZT. Modify Equation (4.32) slightly to get

$$[M]\left\{\ddot{U}(t)\right\} + [K(t)]\{U(t)\} = \{f(t)\} + \{f_d(t)\}, \tag{5.8}$$

where

$$\{f_d(t)\} = -[C_d]\left\{\dot{U}(t)\right\} \tag{5.9}$$

is the velocity feedback and matrix $[C_d]$ is empty except for the piezoelectric load vector from Equation (5.7) times a gain in the column corresponding to the sensing DOF. Take the Laplace transform following Equations (4.31) through (4.35) to get the closed-loop FRF.

$$[H(i\omega)] = \left[-\omega^2[M] + i\omega[C_d] + [K_e] + \sum_{n=1}^{N} \frac{[K_v^n]\; i\omega\,\tau_n}{1 + i\,\tau_n}\right]^{-1} \tag{5.10}$$

Fortunately, only a few points are needed in the vicinity of the peak to extract modal parameters. Alternatively, the velocity feedback matrix $[C_d]$ could have been included in the first-order formulation of Equation (4.21) and complex eigenvalues could be determined as discussed above.

This study was very preliminary, so no attention was paid to numerical values for gains and PZT material constants. The goal was merely to increase the gain and see if the MM model breaks down. Figure 5.23 shows the percent difference between the damping predicted with the MM and C0-20 models. In both cases, the damping was determined by circle-fitting frequency-response functions. The results are for the 5-inch-long test beam with a 10-mil-thick PZT constraining layer. As the gain goes to zero, the PZT just acts like a passive constraining layer, and the damping predictions match closely those for the corresponding geometries with aluminum constraining layers. The stiffer

5-mil-thick VEM is better represented by the MM model, and Figure 5.23(a) shows that this case is insensitive to the range of gains tried. Figure 5.23(b), a case where the MM assumptions are not as good, shows that the error in MM predictions varies slightly with gain, but the errors are very small in the context of an engineering analysis. Consistent with the findings in Section 5.2, the variations are greater for the lower percentages of coverage.

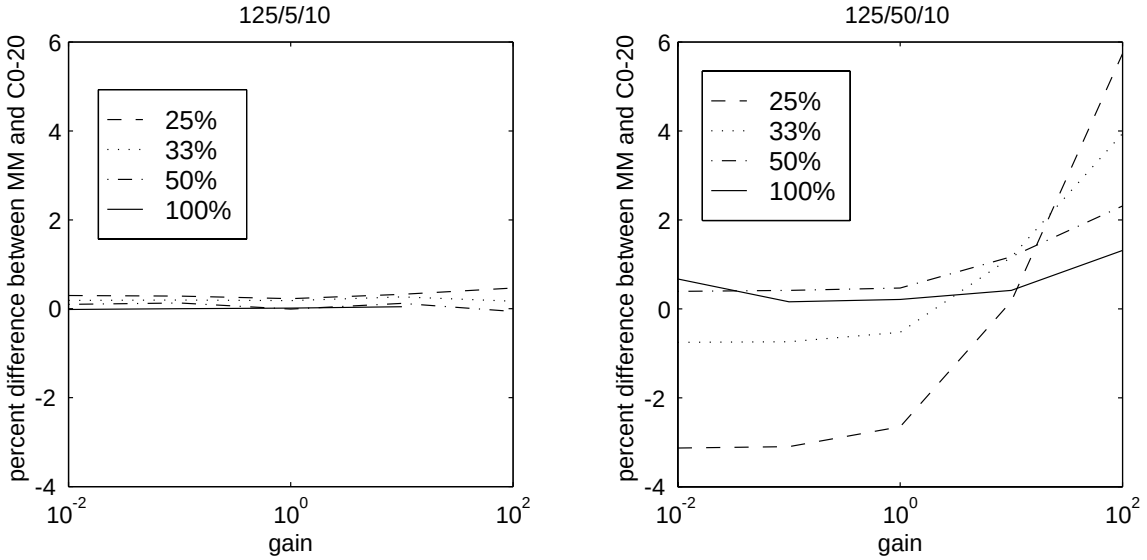

Figure 5.23: Effect of gain on 10-mil PZT constraining layer for the 5-inch-long beam

The conclusions from this brief look at active constrained-layer damping is that the application of gain does not change appreciably the accuracy of the MM model with respect to the higher order C0-20 model. Said another way, if the MM assumptions are good for the passive design, they will be good for the active design. What constitutes the best active design has been the subject of many publications (see summaries in [17] and [52]) and is not discussed here.

Chapter 6

Experiment

The premise of this dissertation is that a thin constraining layer will follow the base beam and thick one will not. An indirect way to show this experimentally is to compare the amounts of damping measured and predicted for cases where the MM assumptions are likely to be in error. A more direct way is to do a modal test and compare the motions of key points on the base and constraining layers. The first alternative is analogous to FEM analysis where the damping was determined by curve-fitting a key frequency-response function (FRF). This is the simpler alternative, but there is a crucial uncertainty: the properties of the viscoelastic material. It does not matter how well a series representation of the VEM properties matches the data if those data do not represent the material used in the experiment. The industry approach is to test the actual VEM used for critical applications before making predictions. Both tests are discussed below

The test article is a 19.2"x1"x1" aluminum bar suspended from the ceiling to simulate a free-free beam. The goal with the boundary condition is minimize the amount of damping introduced to the structure by the fixturing. The test setup is shown schematically in Figure 6.1(a), and the measurement of a driving-point FRF is shown in Figure 6.1(b). One untreated and two treated configurations were tested. The two treated beams had aluminum constraining layers of thicknesses 0.125" and 1.0" covering the middle 25% of the beam, and in both cases the VEM was 10 mils of 3M's ISD 112. Analysis predicted that the thinner CL would follow the MM assumptions and the thicker one would not.

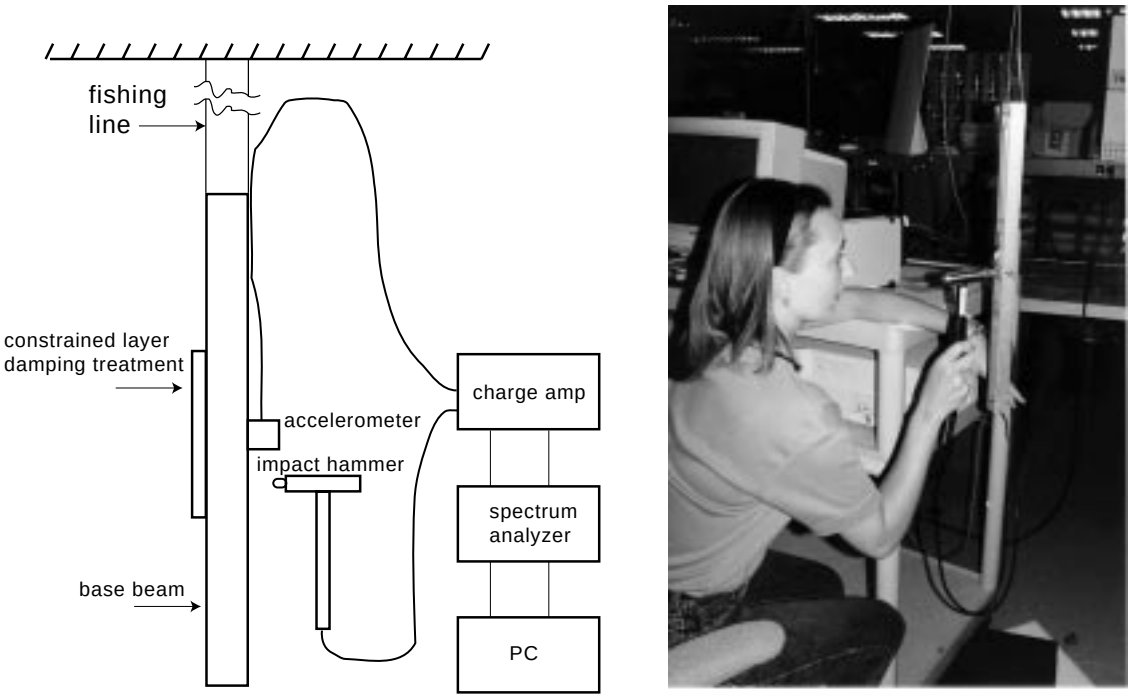

(a) Schematic

(b) Actual impact testing

Figure 6.1: Setup for impact testing

6.1 Approach 1 — Measurements of Modal Damping

Modal damping can be measured from any FRF as long as both the excitation and response locations participate significantly in the mode of interest. The obvious choice for the first mode is the center of the beam, so the damping was determined from driving-point FRFs (excitation and response at the same location) at this point. The normal procedure was to average ten impacts, save the FRF, frequency vector, and coherence to a file, and postprocess the results in MATLAB since the simple data acquisition system used did not have a built-in parameter estimator.

An effect called leakage occurs when a time signal does not die out before the end of a time block, and leakage can lead to false modes and inaccurate levels in the frequency response function (FRF). Consequently, the time signal is often multiplied by a window function that forces the signal to zero by the end of the time block. All windows except the "boxcar" (i.e., no window) affect the shape of a resonant peak in the FRF and, consequently, measurements of damping. This applies also to a "exponential" window, where the window function decreases exponentially to a user-supplied percent of full scale by the end of the time block. This exponential window adds a predictable amount of damping to the signals measured, and this "window damping" can be removed to reveal the true level of damping measured in the structure.

It is nearly impossible to eliminate all external sources of damping such as fixturing and cabling, so the first test was of the bare beam to see how much "accidental" damping was in the system. The FRFs measured by impact test were converted to MATLAB binary data files, and the damping was estimated by the same methods used above [56]. Estimates of damping are very sensitive to spectral resolution, windows, and coherence, so many combinations were tried. After correcting for window effects, the measured loss ranged from 0.09407% to 0.14569%, though the confidence in these outlying measurements was not very high. Table 6.1 shows typical measurements with high confidence (good coherence, good-looking circle fits), so the conclusion from the test of the untreated beam was that miscellaneous sources contribute about 0.12% loss. Figures 6.2(a) and 6.2(b) show the circle fits for this data.

The test of the untreated beam was followed by similar tests of the treated beams with the two different thicknesses of constraining layers. In each case a few different combinations of bandwidths

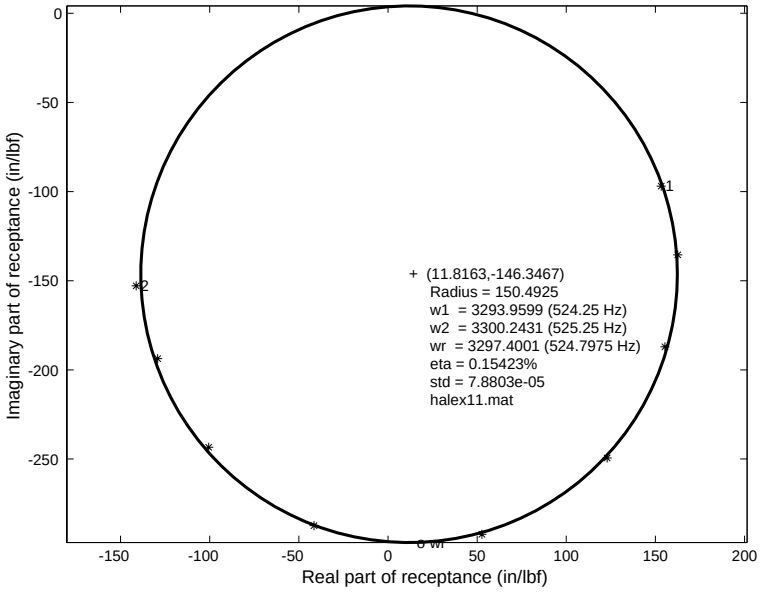

(a) 1% exponential window

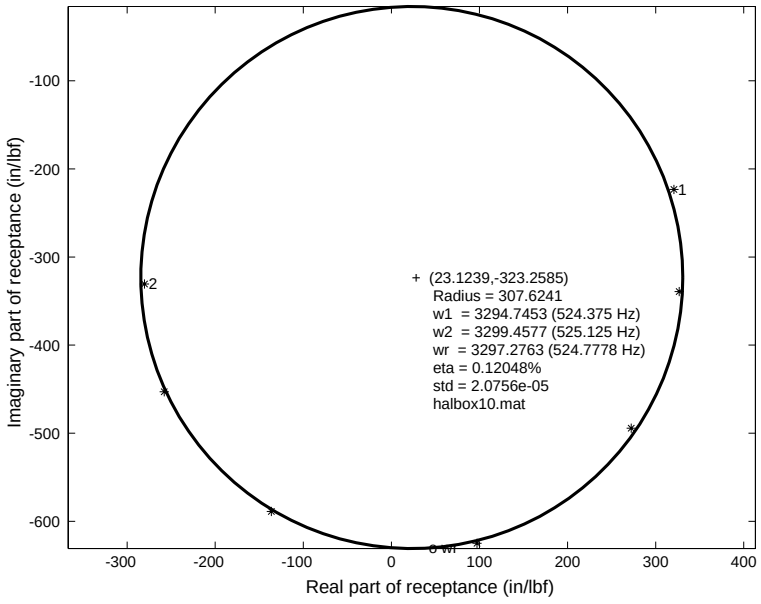

(b) boxcar window

Figure 6.2: Average high-confidence circle fits for the untreated beam

Table 6.1: Frequencies and damping measured for mode 1 with two different response windows for the untreated beam

		loss factor mode 1		
window	freq (Hz)	measured	window	net
1% exp	524.80	0.15423	0.03492	0.11931
boxcar	524.78	0.12048	n/a	0.12048

and record lengths were tried to increase confidence in the loss measurements. It is tempting to specify small spectral resolution, but the price paid is a long time record ($T = \frac{1}{\Delta f}$), and a time record that continues long after the response has died out contains nothing but noise. On the other hand, if the spectral resolution is too coarse, there are not enough points between the half-power frequencies to get a good estimate of loss. Consequently, the spectral resolution was adjusted so that there were on the order of 10 points between the half-power frequencies, and this proved to be a good compromise between spectral resolution and quality of data.

Table 6.2 shows representative loss values measured and analytical predictions using both the C0-20 element and the MM assumptions with free-free boundary conditions. A lumped mass of 8.7

Table 6.2: Experiment vs. analysis for bare and 25% coverage beams

	analytical predictions				experimental measurements		
	C0-20		MM				
test article	freq (Hz)	η (%)	freq (Hz)	η (%)	freq (Hz)	η_o (%)	$\eta - \eta_o$ (%)
bare beam	539	n/a	544	n/a	525	**0.12**	0.0
thin CL	532	**1.18**	536	**1.17**	519	1.42	**1.30**
thick CL	498	**5.32**	584	**1.50**	524	3.22	**3.10**

grams was added to the finite element models to approximate the mass of the accelerometer and cabling. The first line shows that both analysis approaches predict frequencies for first mode about 3% higher than what was measured. The analysis also used nominal properties of E = 10^7 psi for Young's modulus and $\rho = 0.1$ lbs/in^3 for the weight density. Wherever this small frequency discrepancy comes from, it is unlikely to have a significant effect on the fundamental mode of the beam.

The second line of the Table 6.2 shows the predictions and measurements for the 125-mil constrain-

ing layer. Consistent with the analytical studies in earlier sections, the MM and higher order C0-20 approaches predict nearly the same frequency and loss for the fundamental mode for this relatively thin (with respect to the base layer) constraining layer. The analytical predictions of loss are about 10% lower than measured, and as with the untreated beam, the analytical predictions of frequency are about 5% high. The predictions of damping are highly dependent on how well the VEM used in the experiment matches the VEM properties fit for the Maxwell model. Could this account for a 10% variation in final result? This and other possible sources of the discrepancy are discussed at the end of the chapter.

Finally, the third line of the Table 6.2 shows the predictions and measurements for the 1-inch-thick constraining layer. The analytical studies have shown that the MM approach should underpredict the loss greatly for this configuration, and the experimental results confirm that once again. However, the loss measured experimentally is about the average of the two analytical predictions. Rather than focusing on which is right, it is more informative to look at the predicted and measured increases in loss when changing from the thin to the thick constraining layers. If the MM assumptions were valid, the increase in loss would only be on the order of 25%. However, the experiment shows an increase of about 140%. While this is far more than the 25% predicted by MM, it is also far less than the 350% increase predicted by the C0-20 element. This last point will be addressed below, but the conclusion here is that the MM assumptions do a good job for relatively thin constraining layers and a poor job for relatively thick constraining layers, thus verifying the premise of this dissertation.

6.2 Approach 2 — Modal Survey

Measuring modal damping is an indirect way of determining whether or not the CL follows the BL in since it relies on the accuracy of both models and material properties. It is more direct to measure and compare eigenvector amplitudes of points on the base and constraining layers. The simple way to do this with the existing test setup was to leave the accelerometer in place and move the excitation. Then the diameter of circle fits are related to the amplitude of entries in the eigenvector. The excitation points are shown in Figure 6.3.

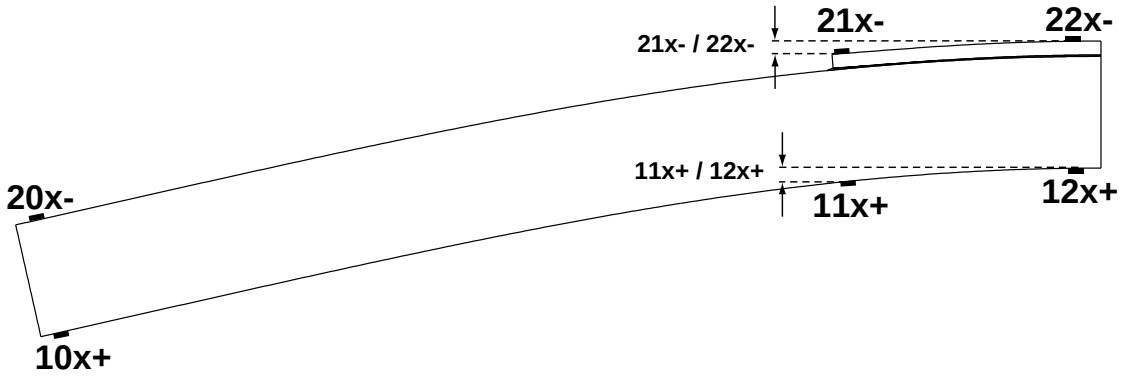

(a) Thin constraining layer

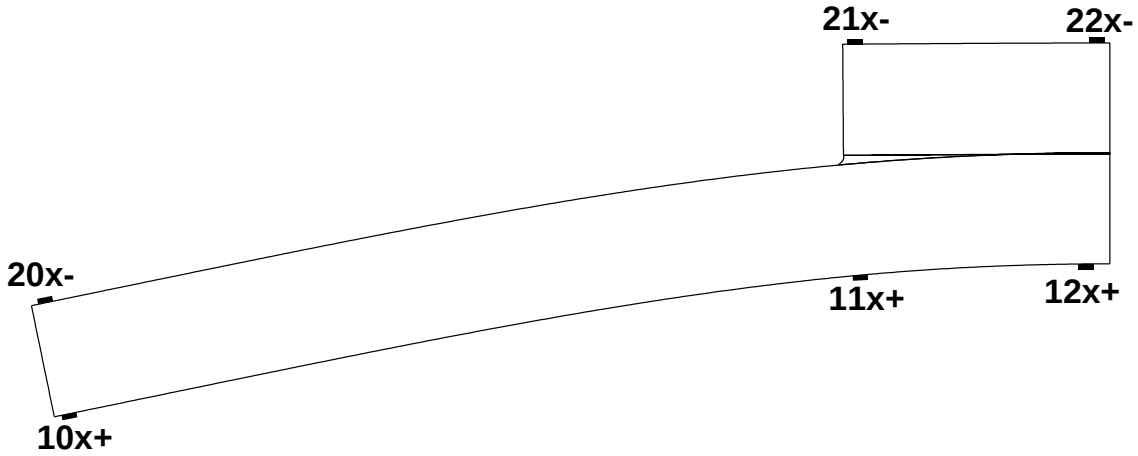

(b) Thick constraining layer

Figure 6.3: Analytical prediction (C0-20 element) of fundamental mode shape of the test articles

The modal amplitudes measured in the test are similar to those predicted by analysis and shown in Figure 6.3. Of particular interest is the ratio of amplitudes at DOFs 21x- and 22x-, i.e., the deflection at the end of the constraining layer relative to its maximum, given in Table 6.2. Similar

Table 6.3: Relationship between BL and CL for fundamental mode of test article: experiment vs. analysis

	0.125"-thick CL			1.0"-thick CL		
	BL $\frac{11x+}{12x+}$	CL $\frac{21x+}{22x+}$	Δ	BL $\frac{11x+}{12x+}$	CL $\frac{21x+}{22x+}$	Δ
C0-20	0.768	0.784	2%	0.731	0.972	33%
experiment	0.750†	0.786†	5%	0.774‡	0.852‡	10%
MM	0.771	0.771	0%	0.791	0.791	0%

† average of 6 modal tests and 2 frequency resolutions
‡ average of 15 modal tests and 4 frequency resolutions

ratios are listed for the base layer, and both are shown in Figure 6.3(a). The analysis results given here assumed a real-valued viscoelastic material. The analytical results with the higher order C0-20 element confirm trends reported earlier in that there is only a 2% difference between the BL and CL ratios for the thin CL, but there is a 33% difference for the thick CL. The large percentage difference is a measure of how much the thick CL wants to stay straight as opposed to bending with the BL. By nature, a MM model will predict a 0% difference between the BL and CL ratios. The most interesting results, however, come from the experiment. The 5% difference in ratios for the thin CL confirm that the CL follows the BL fairly well, though not quite as well as the 2% predicted by analysis. As expected, the experiment showed that the thicker CL does not follow the BL as well as the thinner CL, as evidenced by the 10% difference in amplitude ratios. This 10%, however, is far less than the 33% predicted by analysis and shown in Figure 6.3(b). The most likely explanation for this difference is nonlinear material properties exhibited by the VEM for the large shear and normal displacements. This also could help explain why in Table 6.2 the higher order analysis (C0-20 element) goes from overpredicting the frequency by 2.7% for the bare beam and 2.5% thin CL to *under*predicting the frequency for the thick CL by 5%. The case with the thin CL certainly experiences large shear strains, but the measured and predicted loss and mode shapes are in fairly good agreement. This shifts the focus to the bulk modulus. An analysis that would include

such effects would have to be accompanied by tests capable of predicting the nonlinear multimode material properties. Both of these are outside the goals of this work.

Just like the estimates of damping in the previous section, the modal amplitudes from the experiments came from circle fits of actual data. Table 6.4 lists the frequency ranges for all the tests and gives the minimum coherence over the frequencies used in the circle fits. Figure 6.4 shows the circle-fit and coherence typical of the measurements reported above. Having shown all of this, impact testing is replete with pitfalls, and good-looking frequency response functions, circle fits, and coherence are not guarantees of good measurements [19]. Nonetheless, the test results reported in this section yield physical results and offer a substantial body of evidence that support the basic premise of the dissertation.

Possible reasons for the discrepancies between the analysis and test are

- inaccuracy of the material properties,
- the analytical model does not match the test article, and
- material or geometric nonlinearities.

Rather than casting doubt on the measurement of the material properties, it is likely that the VEM used for the testing has properties different than the one on which the material test were done. Engineers who have performed many damping designs realize the batch-to-batch variation in properties. The more likely culprit is item 2. The test article was chosen for the purpose of a "quick and dirty" test for damping. The analytical model enforces planar motion through the plane stress assumption, but an actual test article that is nearly symmetric has no such restrictions. Finally is the issue of nonlinearity. It is possible to get good coherence in the presence of nonlinearities, so little can be concluded from the current test. It is a future-work item to design fixturing and tests capable of determining nonlinear behavior.

Table 6.4: Frequency resolution and minimum coherence measured for treated test articles

freq (Hz)	Δf (Hz)	DOF	min coh†	tests
0.125-inch-thick constraining layer				
0–1000	1.25	10x+	0.99690	3
0–1000	1.25	11x+	0.99734	3
0–1000	1.25	12x+	0.99891	3
0–1000	1.25	20x–	0.99616	3
0–1000	1.25	21x–	0.99819	3
0–1000	1.25	22x–	0.99835	3
0–1000	2.50	10x+	0.99783	3
0–1000	2.50	11x+	0.99922	3
0–1000	2.50	12x+	0.99861	3
0–1000	2.50	20x–	0.99796	3
0–1000	2.50	21x–	0.99814	3
0–1000	2.50	22x–	0.99878	3
1.0-inch-thick constraining layer				
0–1000	1.25	10x+	0.99828	6
0–1000	1.25	11x+	0.99825	5†
0–1000	1.25	12x+	0.99921	6
0–1000	1.25	20x–	0.99712	6
0–1000	1.25	21x–	0.99959	6
0–1000	1.25	22x–	0.99959	6
0–1000	2.50	10x+	0.99778	6
0–1000	2.50	11x+	0.99887	6
0–1000	2.50	12x+	0.99905	6
0–1000	2.50	20x–	0.99614	6
0–1000	2.50	21x–	0.99956	6
0–1000	2.50	22x–	0.99964	6
525±100	2.00	10x+	0.9809	3
525±100	2.00	11x+	0.99501	3
525±100	2.00	12x+	0.99645	3
525±100	2.00	20x–	0.98482	3
525±100	2.00	21x–	0.99438	3
525±100	2.00	22x–	0.99338	3

†data for one test accidentally not saved

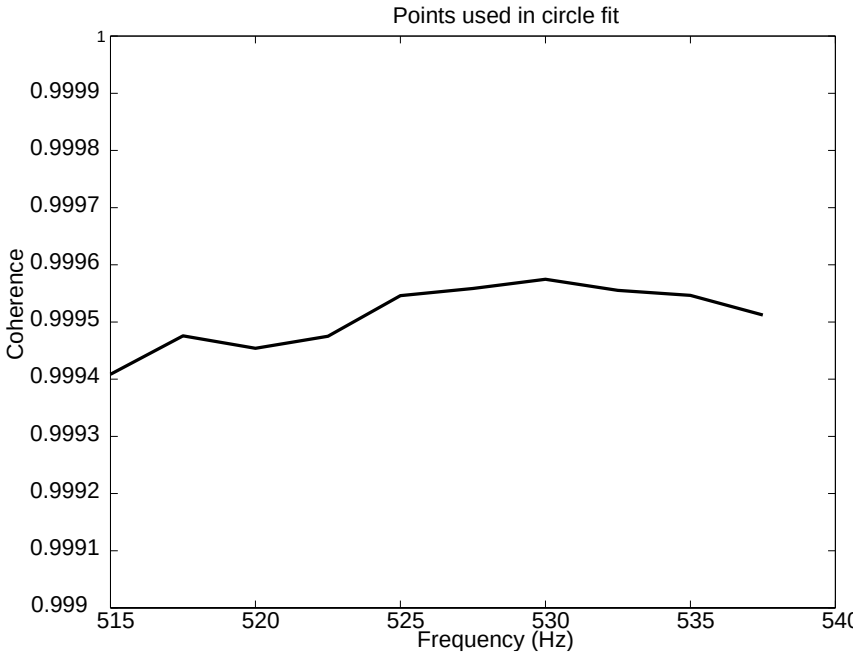

(a) Coherence at frequencies used in circle fit

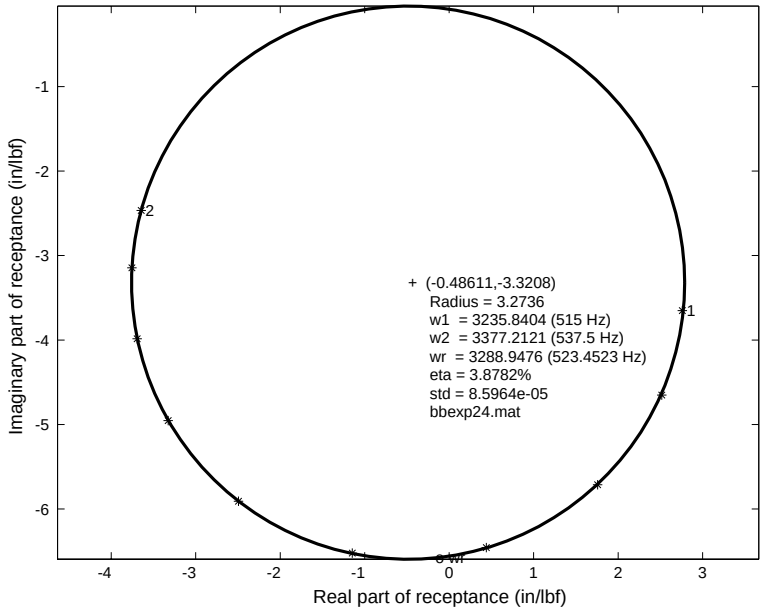

(b) Circle fit

Figure 6.4: Coherence and circle fit typical of the best data reported

Chapter 7

Summary, Conclusions, Contributions, and Future Work

7.1 Summary and Conclusions

There were four goals presented on 2 September 1997 for the dissertation proposal exam. Briefly, they were

1. identify deficiencies in the Mead and Markus modeling approach,
2. implement an internal variable approach to modeling viscoelasticity,
3. assess the difference between modeling PZT's by MM and higher order elements, and
4. perform a proof-of-concept experiment.

All of these items have been addressed and are summarized here.

Item 1

It was first established that the Mead and Markus assumptions were developed for thin, flexible panels, and while this remains a legitimate research topic there are many practical problems where thick, stiff constraining layers must be applied over only small areas of a structure.

Different levels of modeling of the sandwich beams were investigated through finite element analysis. A 4-node, 32-degree-of-freedom, C^1-*capable* element that matches tractions in a functions sense was developed in Section 3.3 to determine the importance of matching tractions at material boundaries. The element is termed C^1-*capable* since it enforces C^1 continuity at same-material boundaries and "breaks" the slope as needed to enforce traction continuity at mismatch material boundaries. A family of C^0 elements (4, 8, 12, 16, and 20 nodes/element) was presented in Section 3.2 and Appendix A. An Euler-Bernoulli beam element with nodes offsetable to the surface was developed in Section 3.4. This element, used for both facesheets, along with the one four-node C^0 for the VEM core simulates the approach taken by Miles and Reinhall, which is also a common approach taken in industry. Adding more elements through the thickness of the VEM showed the effects of a higher order displacement field within the VEM.

The goal of the numerical studies was to show that the MM assumptions break down for benign-looking treatments with only partial coverage. Sandwich beams modeled with the higher order C^0 and C^1 elements were first compared to an elasticity solution for static cylindrical bending. Then, modal strain energy, while not necessarily accurate for large damping, was shown to be an adequate indicator of modeling accuracy. This allowed many trials to be done economically by extracting just the first mode. Next a set of eight thickness geometries were investigated with between 15% and 100% of the beam covered to assess the accuracy of the Mead and Markus modeling assumptions with respect to the 20-node C^0 element. Finally, the effect of not knowing Poisson's ratio was explored for full- and partial-coverage damping treatments.

Item 2

Maxwell representations of linear viscoelasticity were implemented in Chapter 4 following a method published by Johnson [37]. Raw data for the complex shear modulus of 3M's ISD 112 was obtained from CSA Engineering and fit with constants as described in Section 4.3. Four versions of the equations of motion were coded: 1) Johnson's second-order predictor-corrector method, 2) a non-iterative second-order augmented form, a non-iterative first-order augmented form, and a second-

order form in the frequency domain via the viscoelastic correspondence principle.

Item 3

in Section 5.3, a 10-mil-thick PZT was modeled using both higher order C0-20 and MM elements. Straightforward velocity feedback was implemented between a point sensor and induced strains in the PZT. The question was whether the accuracy of the MM model was effected by an increase in gain.

Item 4

A free-free beam was tested three different ways in two different configurations. The middle 25% of a 1-inch-square aluminum bar was treated with 10 mils of ISD 112 and covered by 0.125- and 1.0-inch-thick aluminum constraining layers. Each test was intended to show that the MM assumptions hold for the thin constraining layer and break down for the thick one. Specifics of the testing were discussed in Chapter 6.

The conclusions span the four items as follows.

- The Mead and Markus assumptions work well for sandwich beams with constraining layers weak in bending; this was one of Kerwin's initial assumptions. However, the assumptions breakdown more and more as the percent of partial coverage decreases. There is a hidden trap if only part of the host structure is accessible for a damping treatment: increasing the CL thickness in an attempt to increase damping will cause divergence from the MM assumptions, and large errors will result.

- Configurations where the transverse normal strains are on the same order as the shear strains are very sensitive to the "other" material property, i.e., whatever is deduced from the measured shear modulus. These situations coincide with beams for which the MM assumptions are bad. See Item 7.1.

- As long as they are allowed to deform independently, Euler-beam facesheets provide plenty of accuracy in sandwich beams. Higher order C^0 and C^1 elements are not justified for linear problems.

- feedback through a thin PZT acting as a constraining layer is modeled well by the MM assumptions.
- the C^1-capable element gives good accuracy per degree of freedom, but the computational cost of enforcing the external tractions is high.
- A single bilinear, four-node C^0 through the thickness of the VEM works very well as long as the facesheets deform independently. This is true for linear behavior, but it is untested for problems involving geometric or material nonlinearities.
- The experiment confirms the accuracy of the MM assumptions for a thin CL and their inaccuracy for a thick CL. The question of linearity is still open pending a carefully designed fixturing and testing.

7.2 Contributions

- Demonstrated that the constraints imposed by the Mead and Markus assumptions lead to erroneous predictions of damping in layered viscoelastic damping treatments for practical engineering situations, i.e., partial coverage.
- Revealed that arbitrary choice of Poisson's ratio leads to erroneous predictions of damping in a class of partial-coverage damping treatments.
- Defined the need for multimode characterizations of viscoelastic materials. The shear modulus alone is not enough, even for thin VEM layers if the constraining layer is stiff in bending.
- Developed a 2-D C^1-capable element that matches tractions across material boundaries in a functional sense. This extends the work of Lee *et al.* [49] to 2-D problems with general boundary conditions and partial coverage.
- Demonstrated by experiment that the MM assumptions break down for a stiff, partial-coverage constraining layer.
- Extended Johnson's approach for viscoelasticity to include first- and second-order non-iterative formulations in the time domain.

- Demonstrated that closing the loop on an active constraining layer does not change the applicability of the MM assumptions.

7.3 Future Work

The future work can be broken down in to several broad tasks:

- Determine linear and nonlinear full 3-D viscoelastic material properties for VEMs suitable for layered damping treatments. This is much harder than measuring such properties for poured samples of rubber or elastomers.
- Determine optimal deformation states for loss for viscoelastic materials, i.e., all shear, all transverse normal strain, a combination of the two? What implications would this have on the shape of a passive constraining layer? What about an active constraining layer? and whether they can be achieved through passive means, active means, or a combination of both.
- Extend C^1-capable element to time-dependent tractions due to viscoelasticity.
- Design an experiment and associated fixtures specifically to isolate and investigate possible nonlinearities as well as nonshear loss mechanisms.

7.4 Final Thoughts

Accurate predictions of damping in constrained-layer damping treatments requires both accurate mathematical models and accurate material properties, and as the accuracy of both have advanced there has been a game of leap-frog occurring between the two for the last 50 years. Nakra [64] cites a paper from 1948 by A.W. Nolle [70] on mechanical testing for the properties of rubber, so the technology for such measurements certainly existed. In the early 1950's, Oberst [74, 73, 72] in Germany and Liénard [55] in France published accounts of their trial-and-error approach to qualifying free-layer damping to reduce acoustics in automobile. Neither attempted to design their

coatings, and their work concentrated on test methods and documenting the behavior of various size panels and coatings. Since there were no models, there was no opportunity to include the properties for the viscoelastic coatings. Plass [78] in 1957 developed analytical models for both axial and transverse vibrations of coated bars. He presented some experiment results showing that the amplitudes of axial vibration decrease due to the coating, but he did not determine material properties explicitly. Similarly, Kerwin [41] developed models for constrained-layer damping in 1959, but his tests were only of sandwich panels, not the VEM. Ross *et al.* [87] in 1959 reproduced some plots showing the frequency- and temperature-dependence of a polyvinylchloride, but they did not use them in their analysis. DiTaranto [21] in 1965 develops his sixth-order equations using a complex modulus representation of the VEM. Although this work contains no experimental results, he refers to Ferry [25] for methods of material testing. This seems to be the first mention of incorporating measured VEM properties into a analytical model. Mead and Markus [59] in 1969 also used a complex modulus in their model, but otherwise made no reference to actual VEM properties. Finally, Douglas and Yang [23] use a material with measured properties in their analysis.

With the 1980's came the modal strain energy method [40], and damping analysis and design came within the reach of the general finite element community. There became suddenly a large need for high-quality data on VEM properties. At that time the primary approach to determining the VEM shear modulus was by inferring them from the modal properties of sandwich beams from Mead and Markus models. While sound in theory, the accuracy of the materials depended upon both the accuracy of the modal test and underlying models. By the early 1990's, there were methods for measuring shear moduli directly [8], computer codes for characterizing the properties with models [27], and databases of the VEM properties [68] available to designers. (This list is not complete; there were contributions by other authors to each of these items.)

By the early 1990's, the complex shear modulus had been measured accurately and cataloged for many viscoelastic materials. However, while the materials people perfected their test methods, the engineers and scientists were coming up with applications likely to require more material characterization than just the shear modulus. This is the state of damping analysis in the late 1990's. As researchers work harder to extract more and more energy from VEM layers, the validity of both the MM models and the single-mode material properties should be questioned.

Bibliography

[1] Vibration damping 1984 workshop proceedings. Tech. Rep. AFWAL-TR-84-3064, Air Force Wright Aeronautical Laboratories, November 1984.

[2] Damping 1986 proceedings. Tech. Rep. AFWAL-TR-86-3059, Air Force Wright Aeronautical Laboratories, May 1986.

[3] Proceedings of damping '89. Tech. Rep. WRDC-TR-89-3116, Air Force Wright Aeronautical Laboratories, Nov 1989.

[4] Proceedings of damping '91. Tech. Rep. WL-TR-91-3078, Air Force Wright Aeronautical Laboratories, August 1991.

[5] *Proceedings of the* 32^{th} *AIAA/ASME/ASCE/AHS/ASC Structures, Structural Dynamics, and Materials Conference* (Baltimore, MD, April 1991), no. 3.

[6] Proceedings of damping '93. Tech. Rep. WL-TR-93-3103, Air Force Wright Aeronautical Laboratories, August 1993.

[7] Agnes, G. S. Toward single-element modeling of muli-layer constrained layer damping treatments. In *Proceedings of SPIE Smart Structures and Materials 1995* (March 1995), vol. 2445 Passive Damping and Isolation, SPIE, pp. 336–347.

[8] Allen, B. R., and Kienholz, D. A. Measurement of the mechanical properties of viscoelastics by the direct complex stiffness method. In *Damping '91* (San Diego, CA, February 1991), vol. II, pp. GDD1–GDD11.

[9] Austin, E. M., Flora, T., and Goodding, J. Low-deflection loss and hysteresis measurements on a spacecraft test joint. In *Damping '91* (San Diego, CA, February 1991), vol. III, pp. IBC1–IBC19.

[10] Austin, E. M., and Inman, D. J. Studies on the kimematic assumptions for sandwich beams. In *Proceedings of SPIE Smart Structures and Materials 1997* (February 1997), L. P. Davis, Ed., vol. 3045 Passive Damping and Isolation, SPIE, pp. 173–183.

[11] Austin, E. M., and Inman, D. J. Modeling of sandwich structures. In *Proceedings of SPIE Smart Structures and Materials 1998* (February 1998), vol. 3327 Passive Damping and Isolation, SPIE.

[12] Bai, J. M., and Sun, C. T. A refined theory of flexural vibration for viscoelastic damped sandwich beams. In *Proceedings of Damping '93* (San Francisco, CA, August 1993), no. WL-TR-93-3103, pp. JBB1–JBB16.

[13] Bai, J. M., and Sun, C. T. The effect of viscoelastic adhesive layers on structural damping of sandwich beams. *Mechanics of Structures and Machines 23*, 1 (1995), 1–16.

[14] Baz, A. Active constrained layer damping. In *Proceedings of Damping '93* (San Francisco, CA, August 1993), no. WL-TR-93-3103, pp. IBB1–IBB23.

[15] Baz, A., and Ro, J. Finite element modeling and performance of active constrained layer damping. In *Ninth VPI&SU Conference on Dynamics and Control of Large Structure Conference* (Blacksburg, VA, May 1993), pp. 345–358.

[16] Baz, A., and Ro, J. Partial treatment of flexible beams with active constrained layer damping. In *Conference of Engineering Science Society* (Charlottesville, VA, June 1993), vol. 167, ASME, pp. 61–80.

[17] Baz, A., and Ro, J. Optimum design and control of active constrained layer damping. *Journal of Mechanical Design and Journal of Vibration and Acoustics 117 (B)* (1995), 135–144. ASME 50th Anniversary Design Engineering Division.

[18] Bhimaraddi, A. Sandwich beam theory and the analysis of constrained layer damping. *Journal of Sound and Vibration 179*, 4 (1995), 591–602.

[19] Corelli, D., and Brown, D. L. Impact testing considerations. In *2nd International Modal Analysis Conference* (Orlando, FL, February 1994), pp. 735–742.

[20] Crandall, S. H. The role of damping in vibration theory. *Journal of Sound and Vibration 11*, 1 (1970), 3–18.

[21] DiTaranto, R. A. Theory of vibratory bending for elastic and viscoelastic layered finite-length beams. *Journal of Applied Mechanics 32* (December 1965), 881–886.

[22] Douglas, B. E. Compressional damping in three-layer beams incorporating nearly incompressible viscoelastic cores. *Journal of Sound and Vibration 104*, 2 (1986), 343–347.

[23] Douglas, B. E., and Yang, J. C. S. Transverse compressional damping in the vibratory response of elastic-viscoelastic-elastic beams. *AIAA Journal 16*, 9 (1978), 925–930.

[24] Dubbelday, P. S. Constrained-layer model investigation based on exact elasticity theory. *Journal of the Acoustical Society of America 80*, 4 (October 1986), 1097–1102.

[25] Ferry, J. D. *Viscoelastic Properties of Polymers.* John Wiley & Sons, New York, NY, 1960.

[26] Findley, W. N., Lai, J. S., and Onaran, K. *Creep and Relaxation of Nonlinear Viscoelastic Materials (With an Introduction to Linear Viscoelasticity).* Dover, 1989.

[27] Fowler, B. L. Interactive characterization and database storage of complex modulus data. In *Damping '89* (West Palm Beach, FL, February 1989), vol. I, pp. FAA1–FAA12.

[28] Golla, D. F., and Hughes, P. C. Dynamics of viscoelastic structures — a time-domain, finite element formulation. *ASME Journal of Applied Mechanics 52* (1985), 897–906.

[29] Huang, S.-C., Inman, D. J., and Austin, E. M. Some design considerations for active and passive constrained layer damping treatments. *Journal of Smart Materials & Structures 5* (1996), 301–313.

[30] Hyer, M. W. *Stress Analysis of Fiber-Reinforced Composite Materials*, first ed. McGraw-Hill, 1998.

[31] Ikegami, R., Beck, C. J., and Walker, W. J. Application of damping to imporve reliability of ius-type satellite equipment — RELSAT program. In *Vibration Damping 1984 Workshop Proceedings* (Long Beach, CA, November 1984), pp. TT1–TT15.

[32] Ikegami, R., and Johnson, D. W. The design of viscoelastic passive damping treatments for satellite equipment support structures. In *Damping 1986 Proceedings* (Las Vegas, NV, May 1986), pp. HB1–HB20.

[33] Imaino, W., and Harrison, J. C. A comment on constrained layer damping structures with low viscoelastic modulus. *Journal of Sound and Vibration 149*, 2 (1991), 354–359. Technical Note.

[34] Johnson, A. R., and Quigley, C. J. A viscohyperelastic Maxwell model for rubber viscoelasticity. *Rubber Chemistry and Technology 65*, 1 (March-April 1992), 137–153.

[35] Johnson, A. R., Quigley, C. J., and Freese, C. E. A viscohyperelastic finite element model for rubber. *Computer Methods in Applied Mechanics and Engineering 127* (1995), 163–180.

[36] Johnson, A. R., and Stacer, R. G. Rubber viscoelasticity using the physically constrained systems stretches as internal variables. *Rubber Chemistry and Technology 66*, 4 (Sept-Oct 1993), 567–577.

[37] Johnson, A. R., Tessler, A., and Dambach, M. Dynamics of thick viscoelastic beams. *Journal of Engineering Materials and Technology 119*, 3 (July 1997), 273–278.

[38] Johnson, C. D. Design of passive damping systems. *Journal of Mechanical Design and Journal of Vibration and Acoustics 117 (B)* (June 1995), 171–176. ASME 50th Anniversary of the Design Engineering Division.

[39] Johnson, C. D., and Kienholz, D. A. Finite element prediction of damping in structures with constrained viscoelastic layers. *AIAA Journal 20*, 9 (1982), 1284–1290.

[40] Johnson, C. D., Kienholz, D. A., and Rogers, L. C. Finite element prediction of damping in beams with constrained viscoelastic layers. *The Shock and Vibration Bulletin 51*, 1 (May 1981), 71–81.

[41] Kerwin, E. M. Damping of flexural waves by a constrained visco-elastic layer. *Journal of the Acoustical Society of America 31* (1959), 952–962.

[42] Kerwin, E. M., and Ross, D. A comparison of the effectiveness of homogeneous layers and constrained layers of viscoelastic material in damping flexural waves in plates. In *3rd International Congress on Acoustics* (Stuttgart, 1959), pp. 410–412.

[43] Kerwin, E. M., and Smith, P. W. Segmenting and mechanical attachment of constrained viscoelastic layer damping treatments for flexural and extensional waves. In *Vibration Damping 1984 Workshop Proceedings* (Long Beach, CA, 1984), pp. KK1–KK24.

[44] Kluesener, M. F. Results of finite element analysis of damped structures. In *Vibration Damping 1984 Workshop Proceedings* (Long Beach, CA, 1984), pp. JJ1–JJ12.

[45] Lagnese, T. J., and Jones, D. I. G. Complex modulus behavior of a viscoelastic adhesive measured at harmonic strain amplitudes of 10^{-10}. In *Vibration Damping 1984 Workshop Proceedings* (Long Beach, CA, 1984), pp. E1–E17.

[46] Lall, A. K., Asnani, N. T., and Nakra, B. C. Damping analysis of partially covered sandwich beams. *Journal of Sound and Vibration 123*, 2 (1988), 247–259.

[47] Lam, M. J. *Hybrid Active/Passive Models With Frequency Dependent Damping*. PhD thesis, Virginia Polytechnic Institute and State University, October 1997.

[48] Lee, B.-C., and K.-J, K. Effects of normal strain in core material on modal property of sandwich plates. *Journal of Vibration and Acoustics 119* (October 1997), 493–503.

[49] Lee, C.-Y., and Liu, D. An interlaminar stress continuity theory for laminated composite analysis. *Composites and Structures 42*, 1 (1992), 69–78.

[50] Lee, E. H. Viscoelastic stress analysis. In *Proceedings of the First Symposium on Naval Structural Mechanics* (1960), pp. 456–482.

[51] Lesieutre, G. A. Modeling material damping using augmenting thermodynamic fields (atf). In *Damping '89* (West Palm Beach, FL, February 1989), vol. 167, pp. GDB1–GDB13.

[52] Lesieutre, G. A., and Lee, U. A finite element for beams having segmented active constrained layers with frequency-dependent viscoelastics. *Journal of Smart Materials & Structures 5* (1996), 615627.

[53] Liao, W. H., and Wang, K.-W. On the active-passive hybrid control actions of structures with active constrained layer treatments. *Journal of Vibration and Acoustics 119* (1997), 563–572.

[54] Librescue, L., and Reddy, J. N. A few remarks concerning several refined theories of anisotropic composite laminated plates. *International Journal of Engineering Science 27*, 5 (1989), 515–527.

[55] Liénard, P. Étude d'une méthode de mesure du frottement intérieur de revêtements plastiques travaillant en flexion. *La Recherche Aéronautique 20* (1951), 11–22.

[56] Maia, N. M. M., and Silva, J. M. M., Eds. *Thoeretical and Experimental Modal Analysis*, first ed. Research Studies Press Ltd., 1997.

[57] Marcelin, J.-L., Trompette, P., and Smati, A. Optimal constrained layer damping with partial coverage. *Finite Elements in Analysis and Design 12* (1992), 273–280.

[58] Mead, D. J. A comparison of some equations for the flexural vibration of damped sandwich beams. *Journal of Sound and Vibration 83*, 3 (1982), 363–377.

[59] Mead, D. J., and Markus, S. The forced vibration of a three-layer, damped sandwich beam with arbitrary boundary conditions. *Journal of Vibration and Acoustics 10*, 2 (1969), 163–175.

[60] Meirovitch, L. *Principles and Techniques of Vibrations*, first ed. Prentice Hall, 1997.

[61] Miles, R. N. Beam dampers for skin vibration and noise reduction in the 747. In *Vibration Damping 1984 Workshop Proceedings* (Long Beach, CA, 1984), pp. PP1–PP18.

[62] Miles, R. N., and Reinhall, P. G. An analytical model for the vibration of laminated beams including the effects of both shear and thickness deformation in the adhesive layer. *Journal of Sound and Vibration 108* (1986), 56–64.

[63] Morgenthaler, D. R. The absolute value modal strain energy method. In *Damping '91* (San Diego, CA, February 1991), vol. II, pp. FDB1–FDB16.

[64] Nakra, B. C. Vibration control with viscoelastic materials. *Shock and Vibration Digest 8*, 6 (June 1976), 3–12.

[65] Nakra, B. C. Vibration control with viscoelastic materials – II. *Shock and Vibration Digest 13*, 1 (January 1981), 17–20.

[66] Nakra, B. C. Vibration control with viscoelastic materials – III. *Shock and Vibration Digest 16*, 5 (May 1984), 17–22.

[67] Nashif, A. D., Jones, D. I. G., and Henderson, J. P. *Vibration Damping*, first ed. Wiley-Interscience, 1985.

[68] Nashif, A. D., and Lewis, T. M. Data base of the dynamic properties of materials. In *Damping '91* (San Diego, CA, February 1991), vol. II, pp. DBB1–DBB26.

[69] Nokes, D. S., and Nelson, F. C. Constrained layer damping with partial coverage. *The Shock and Vibration Bulletin 38*, 3 (November 1969), 5–12.

[70] Nolle, A. W. Methods for measuring dynamic mechanical properties of rubber-like materials. *Journal of Applied Physics 19* (November 1948), 753.

[71] Noor, A. K., and Burton, S. W. Assessment of shear deformation theories for multilayered composite plates. *Applied Mechanics Reviews 42*, 1 (January 1989), 1–13.

[72] Oberst, H. Werkstoffe mit extrem hoher innerer dämpfung. *Acustica (Akustiche Beihefte) 6* (1956), 144–153.

[73] Oberst, H., Becker, G. W., and Frankenfeld, K. Über die dämpfung der biegeschwingungen dünner bleche durch fest haftende beläge II. *Acustica 4* (1954), 433–444.

[74] Oberst, H., and Frankenfeld, K. Über die dämpfung der biegeschwingungen dünner bleche durch fest haftende beläge I. *Acustica 2* (1952), 181–194.

[75] Ojalvo, I. U. Departures from classical beam theory in laminated, sandwich, and short beams. *AIAA Journal 15*, 10 (1977), 1518–1521.

[76] Pagano, N. J. Exact solutions for composite laminates in cylindrical bending. *Journal of Composite Materials 3* (1969), 398–411.

[77] Park, C. H., Inman, D. J., and Lam, M. J. Model reduction of viscoelastic finite element models. *Journal of Sound and Vibration* (1998). in press.

[78] Plass, H. J. Damping of vibrations in elastic rods and sandwich structures by incorporation of additional viscoelastic material. In *3rd Midwestern Conference on Solid Mechanics* (1957), pp. 48–71.

[79] Plump, J. M., and Hubbard, J. E. Modelling of an active constrained layer damper. In *12th International Congress on Acoustics* (Toranto, 1986). paper D41.

[80] Plunkett, R., and Lee, C. T. Length optimization for constrained viscoelastic layer damping. *Journal of the Acoustical Society of America 48*, 1, part 2 (1970), 150–161.

[81] Rao, D. K. Vibration of short sandwich beams. *Journal of Sound and Vibration 52*, 2 (1977), 253–263.

[82] Rao, D. K. Frequency and loss factors of sandwich beams under various boundary conditions. *J. Mech. Engr. Science 20*, 5 (1978), 271–282.

[83] Reddy, J. N. On refined computational models of composite laminates. *International Journal of Numerical Methods in Engineering 27*, 2 (1989), 361–382.

[84] Reddy, J. N. A review of refined theories of laminated composite plates. *Shock and Vibration Digest 22*, 7 (1990), 3–17.

[85] Reddy, J. N. *An Introduction to the Finite Element Method*, second ed. McGraw-Hill, Inc., 1993.

[86] Robbins, D. H., and Reddy, J. N. Modelling of thick composites using a layerwise laminate theory. *International Journal of Numerical Methods in Engineering 36*, 4 (1993), 655–677.

[87] Ross, D., Ungar, E. E., and Kerwin, E. M. Damping of plate flexural vibrations by means of viscoelastic laminae. In *Structural Damping — a colloquium on structural damping held at the ASME annual meeting* (Atlantic City, NJ, Dec. 1959), pp. 49–87.

[88] Saito, H., and Tani, H. Vibrations of bonded beams with a single lap adhesive joint. *Journal of Sound and Vibration 92*, 2 (1984), 299–309.

[89] Salmanoff, J. A finite element, reduced order, frequency dependent model of viscoelastic damping. Master's thesis, Virginia Polytechnic Institute and State University, 1997.

[90] Shames, I. H., and Dym, C. L. *Energy and Finite Element Methods in Structural Mechanics*, first ed. Taylor and Francis, 1985.

[91] Shen, I. Y. A variational formulation, a work-energy relation, and damping mechanisms of active constrained layer treatments. *Journal of Vibration and Acoustics 119*, 2 (April 1997), 192–199.

[92] Slater, J. C. Modeling of non-proportional frequency dependent viscoelastic damping in space structures. Master's thesis, State University of New York at Buffalo, 1991.

[93] Sokolnikoff, I. S. *Mathematical Theory of Elasticity*, second (reprint) ed. Krieger, 1983.

[94] Staley, J. A., Stahle, C. V., and Strain, J. C. Design and experimental verification of damped spacecraft equipment panels. In *Damping 1986 Proceedings* (Las Vegas, NV, May 1986), pp. HE1–HE31.

[95] Staley, J. A., and V., C. Damping in support structures for satellite equipment reliability — RELSAT. In *Vibration Damping 1984 Workshop Proceedings* (Long Beach, CA, November 1984), pp. UU1–UU26.

[96] Sylwan, O. Calculation of partially covering damping layers of sandwich structures with some practical results. In *International Conference on Noise Control Engineering (inter-noise 78)* (1978), W. D. Lang, Ed., pp. 219–224.

[97] Sylwan, O. Shear and compressional damping effects of constrained layered beams. *Journal of Sound and Vibration 118*, 1 (1987), 35–45.

[98] Taylor, T. W., and Nayfeh, A. H. Natural frequencies of thick, layered composite plates. *Composites Engineering 4*, 10 (1994), 1011–1021.

[99] Taylor, T. W., and Nayfeh, A. H. The vibration characteristics of thick rectangular multilayer plates. *Composites Part B (Engineering) 27*, 6 (1996), 623–631.

[100] Taylor, T. W., and Nayfeh, A. H. Damping characteristics of laminated thick plates. *Journal of Applied Mechanics 64* (March 1997), 132–138.

[101] Taylor, T. W., Nayfeh, A. H., and Wade, J. E. Dynamic response of thick anisotripic composite plates. *Composites Engineering 4*, 5 (1994), 475–486.

[102] Tessler, A., Saether, E., and Tsui, T. Vibration of thick laminated composite plates. *Journal of Sound and Vibration 179*, 3 (1995), 475–498.

[103] Torvik, P. J. The analysis and design of constrained layer damping treatments. In *Proceedings ASME Winter Annual Meeting — Damping Applications for Vibration Control* (1980), ASME, pp. 85–112.

[104] Torvik, P. J., and Bagley, R. L. Fractional derivatives in the description of damping materials and phenomena. In *Proceedings ASME 11th Biennial Conference on Mechanical Vibrations and Noise* (Boston, MA, 1987), vol. 5, ASME, pp. 125–135.

[105] Ungar, E. E., and Kerwin, E. M. Loss factors of viscoelastic systems in terms of energy concepts. *Journal of the Acoustical Society of America 34* (1962), 954–957.

[106] Wu, C.-P., and Hsu, C.-S. A new local high-order lamination theory. *Comosites Structures Journal 25* (1993), 439–448.

[107] Yae, K. H. *Reduced Order Modeling and Analytical Model Modification for Structural Dynamics and Control*. PhD thesis, State University of New York at Buffalo, 1987.

[108] Yae, K. H., and Inman, D. J. Model reduction in a subset of the original states. *Journal of Sound and Vibration 155*, 1 (1992), 165–176.

[109] Yang, J., Batra, R., and Liang, X. The cylindrical bending vibration of a laminated elastic plate due to piezoelectic actuators. *Journal of Smart Materials & Structures 3* (1994), 485–493.

[110] Yiu, Y. C. A quantitative evaluation of constrained-layer damping. In *Proceedings of the* 34^{th} *AIAA/ASME/ASCE/AHS/ASC Structures, Structural Dynamics, and Materials Conference* (La Jolla, California, April 1993), pp. 2110–2119.

[111] Yiu, Y. C. Substructure and finite element formulation for linear viscoelastic materials. In *Proceedings of the* 35^{th} *AIAA/ASME/ASCE/AHS/ASC Structures, Structural Dynamics, and Materials Conference* (Hilton Head, SC, April 1994), pp. 1585–1594.

[112] Zienkiewicz, O. C. *The Finite Element Method*, third ed. McGraw-Hill, Inc., 1977.

Appendix A

C^0 Shape Functions

This appendix contains C^0 shape functions for serendipity elements with 8, 12, 16, and 20 nodes. The numbering order is shown in Figure A.1. Reddy [85] derives the shape functions for an eight-node element by multiplying equations of the lines that pass through pairs of midside nodes. While simple to understand, it is difficult to extend this approach to higher order elements. Zienkiewicz [112] points this out and gives an algorithm for generating shape functions for elements with any combination of midside nodes. Reddy also lists without derivation the shape functions for a 12-node element with equally spaced midside nodes. The shape functions for 16- and 20-node elements were derived using the procedure in Zienkiewicz as follows.

The algorithm for generating shape functions for midside nodes starts with the shape functions for a basic four-node element (Figure 3.1), which are repeated here from Equation (3.13):

$$\begin{aligned} \hat{N}_1(\xi,\zeta) &= \frac{1}{4}(1-\xi)(1-\zeta) & \hat{N}_3(\xi,\zeta) &= \frac{1}{4}(1+\xi)(1+\zeta) \\ \hat{N}_2(\xi,\zeta) &= \frac{1}{4}(1+\xi)(1-\zeta) & \hat{N}_4(\xi,\zeta) &= \frac{1}{4}(1-\xi)(1+\zeta) \end{aligned} \tag{A.1}$$

where $-1 \le \xi \le 1$ and $-1 \le \zeta \le 1$. Next define the equation of lines that define the four sides of the element:

$$\begin{aligned} \Gamma_b &= 1+\zeta & \Gamma_r &= 1-\xi \\ \Gamma_t &= 1-\zeta & \Gamma_l &= 1+\xi \end{aligned} \tag{A.2}$$

where the subscripts b, r, t, and l stand for bottom, right, top and left. A shape function for the i^{th} node must have a value of 1.0 at that node, 0.0 at all other nodes on that side, and 0.0 on all sides not containing that node. Thus, the shape function for node 5 in Figure A.1(b) would start out as the product of the functions that render the other three sides zero, so tentatively the new shape function would be

$$\hat{N}_5(\xi,\zeta) = \Gamma_r\Gamma_t\Gamma_l = (1-\xi)(1-\zeta)(1+\xi) \tag{A.3}$$

The shape function also has to be zero at any other midside nodes on the same side. This is just node 9 located at $(\frac{1}{3},-1)$ in this case, so multiply the shape function by $(\xi-\frac{1}{3})$ to get

$$\hat{N}_5(\xi,\zeta) = (1-\xi)(1-\zeta)(1+\xi)(\xi-\frac{1}{3}) \tag{A.4}$$

Finally, the new shape function must have a value of 1.0 at node 5, so define

$$N_5(\xi,\zeta) = \frac{\hat{N}_5(\xi,\zeta)}{\hat{N}_5\Big(-\frac{1}{3},-1\Big)} = \frac{\hat{N}_5(\xi,\zeta)}{\frac{-32}{27}} = \frac{9}{32}(1-\xi^2)(1-\zeta)(1-3\xi) \tag{A.5}$$

Following the same procedure for nodes 8, 9, and 12, their shape functions are

$$\begin{aligned}
N_8(\xi,\zeta) =& \frac{9}{32}(1+3\zeta)(1-\zeta^2)(1-\xi)\\
N_9(\xi,\zeta) =& \frac{9}{32}(1-\zeta)(1+3\xi)(1-\xi^2)\\
N_{12}(\xi,\zeta) =& \frac{9}{32}(1-3\zeta)(1-\zeta^2)(1-\xi)
\end{aligned}$$

Now there is the problem that the original shape function $\hat{N}_1$ must be zero at the new midside nodes (5,8,9,12) on adjoining sides. Since

$$\begin{aligned}
&\hat{N}_1\Big(-\frac{1}{3},-1\Big) = \frac{2}{3} \text{ at node 5,}\\
&\hat{N}_1\Big(\frac{1}{3},-1\Big) = \frac{1}{3} \text{ at node 9,}\\
&\hat{N}_1\Big(-1,-\frac{1}{3}\Big) = \frac{2}{3} \text{ at node 12, and}\\
&\hat{N}_1\Big(-1,\frac{1}{3}\Big) = \frac{1}{3} \text{ at node 8,}
\end{aligned}$$

the shape functions N_5, N_8, N_9, and N_{12} can be used to form N_1

$$\begin{aligned}
N_1(\xi,\zeta) =& \hat{N}_1 - \frac{2}{3}N_5 - \frac{1}{3}N_9 - \frac{2}{3}N_{12} - \frac{1}{3}N_8\\
=& \frac{1}{32}(1-\zeta)(1-\xi)(-10+9(\zeta^2+\xi^2))
\end{aligned} \tag{A.6}$$

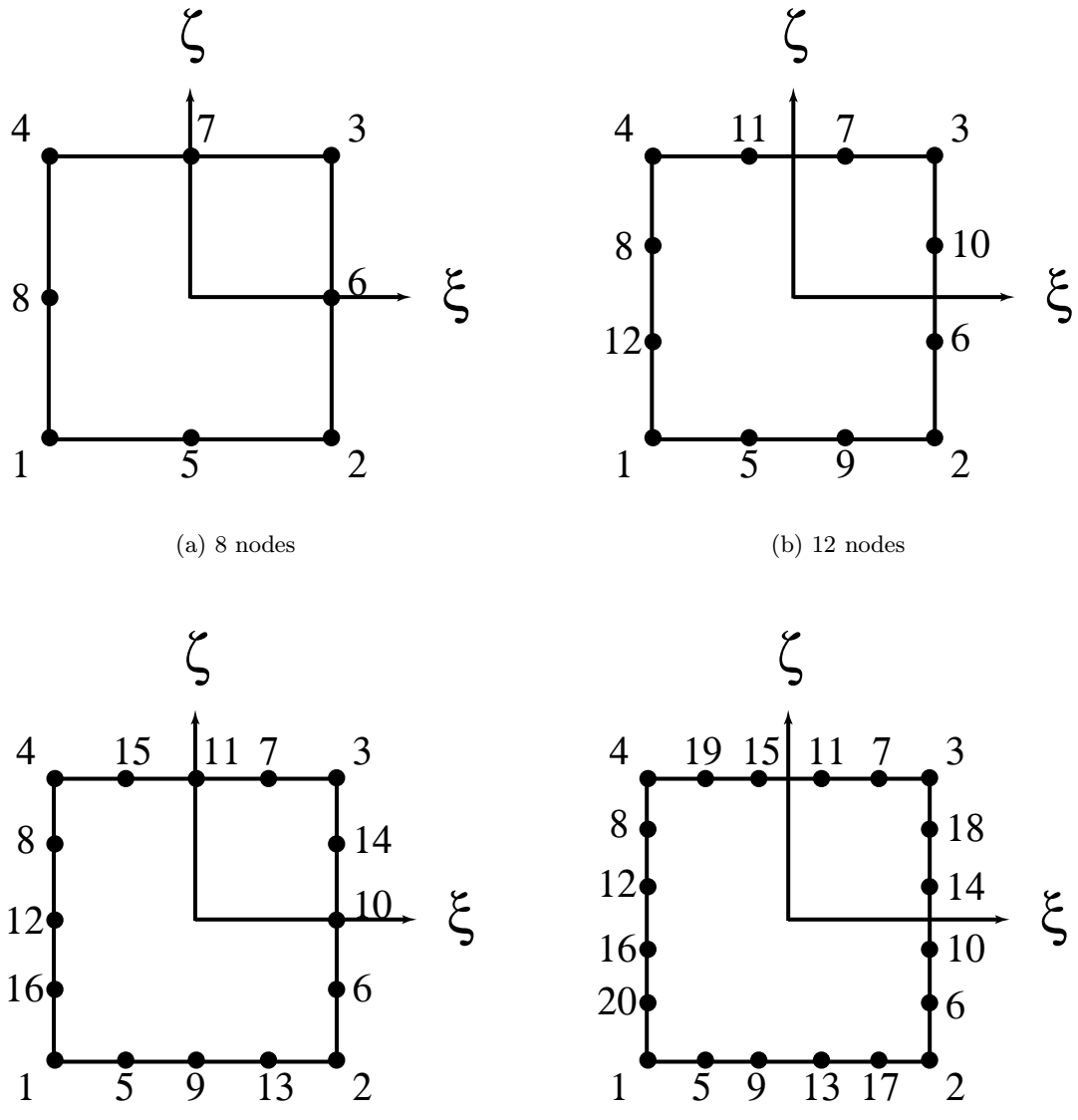

(a) 8 nodes

(b) 12 nodes

(c) 16 nodes

(d) 20 nodes

Figure A.1: Higher order serendipity elements

C0-8.

$$N_1(\xi,\zeta) = \frac{1}{4}(1-\zeta)(\xi-1)(1+\zeta+\xi) \qquad N_5(\xi,\zeta) = \frac{1}{2}(\zeta-1)(\xi^2-1)$$
$$N_2(\xi,\zeta) = \frac{1}{4}(\zeta-1)(1+\zeta-\xi)(1+\xi) \qquad N_6(\xi,\zeta) = \frac{1}{2}(1-\zeta^2)(1+\xi)$$
$$N_3(\xi,\zeta) = \frac{1}{4}(1+\zeta)(1+\xi)(\zeta+\xi-1) \qquad N_7(\xi,\zeta) = \frac{1}{2}(1+\zeta)(1-\xi^2)$$
$$N_4(\xi,\zeta) = \frac{1}{4}(\xi-1)(1-\zeta^2+\xi+\zeta\xi) \qquad N_8(\xi,\zeta) = \frac{1}{2}(\zeta^2-1)(\xi-1)$$

C0-12.

$$N_1(\xi,\zeta) = \frac{1}{32}(1-\zeta)(1-\xi)(-10+9(\zeta^2+\xi^2)) \qquad N_7(\xi,\zeta) = \frac{9}{32}(1+\zeta)(1+3\xi)(1-\xi^2)$$
$$N_2(\xi,\zeta) = \frac{1}{32}(1-\zeta)(1+\xi)(-10+9(\zeta^2+\xi^2)) \qquad N_8(\xi,\zeta) = \frac{9}{32}(1+3\zeta)(1-\zeta^2)(1-\xi)$$
$$N_3(\xi,\zeta) = \frac{1}{32}(1+\zeta)(1+\xi)(-10+9(\zeta^2+\xi^2)) \qquad N_9(\xi,\zeta) = \frac{9}{32}(1-\zeta)(1+3\xi)(1-\xi^2)$$
$$N_4(\xi,\zeta) = \frac{1}{32}(1+\zeta)(1-\xi)(-10+9(\zeta^2+\xi^2)) \qquad N_{10}(\xi,\zeta) = \frac{9}{32}(1+3\zeta)(1-\zeta^2)(1+\xi)$$
$$N_5(\xi,\zeta) = \frac{9}{32}(1-\zeta)(1-3\xi)(1-\xi^2) \qquad N_{11}(\xi,\zeta) = \frac{9}{32}(1+\zeta)(1-3\xi)(1-\xi^2)$$
$$N_6(\xi,\zeta) = \frac{9}{32}(1-3\zeta)(1-\zeta^2)(1+\xi) \qquad N_{12}(\xi,\zeta) = \frac{9}{32}(1-3\zeta)(1-\zeta^2)(1-\xi)$$

C0-16.

$$N_1(\xi,\zeta) = \frac{1}{12}(1-\zeta)(\xi-1)(3-\zeta+4\zeta^3-\xi+4\xi^3) \qquad N_9(\xi,\zeta) = \frac{1}{2}(1-\zeta)(\xi^2-1)(4\xi^2-1)$$
$$N_2(\xi,\zeta) = \frac{1}{12}(\zeta-1)(1+\xi)(3-\zeta+4\zeta^3+\xi-4\xi^3) \qquad N_{10}(\xi,\zeta) = \frac{1}{2}(\zeta^2-1)(4\zeta^2-1)(1+\xi)$$
$$N_3(\xi,\zeta) = \frac{1}{12}(1+\zeta)(1+\xi)(-3-\zeta+4\zeta^3-\xi+4\xi^3) \qquad N_{11}(\xi,\zeta) = \frac{1}{2}(1+\zeta)(\xi^2-1)(4\xi^2-1)$$
$$N_4(\xi,\zeta) = \frac{1}{12}(1+\zeta)(1-\xi)(-3-\zeta+4\zeta^3+\xi-4\xi^3) \qquad N_{12}(\xi,\zeta) = \frac{1}{2}(1-\zeta^2)(4\zeta^2-1)(\xi-1)$$
$$N_5(\xi,\zeta) = \frac{2}{3}(\zeta-1)(\xi^2-1)\xi(2\xi-1) \qquad N_{13}(\xi,\zeta) = \frac{2}{3}(\zeta-1)\xi(\xi^2-1)(1+2\xi)$$
$$N_6(\xi,\zeta) = \frac{2}{3}(1-\zeta^2)\zeta(2\zeta-1)(1+\xi) \qquad N_{14}(\xi,\zeta) = \frac{2}{3}(1-\zeta^2)\zeta(1+2\zeta)(1+\xi)$$
$$N_7(\xi,\zeta) = \frac{2}{3}(1+\zeta)(1-\xi^2)\xi(1+2\xi) \qquad N_{15}(\xi,\zeta) = \frac{2}{3}(1+\zeta)(1-\xi^2)\xi(2\xi-1)$$
$$N_8(\xi,\zeta) = \frac{2}{3}\zeta(\zeta^2-1)(1+2\zeta)(\xi-1) \qquad N_{16}(\xi,\zeta) = \frac{2}{3}\zeta(\zeta^2-1)(2\zeta-1)(\xi-1)$$

C0-20.

$$
\begin{aligned}
N_1(\xi,\zeta) =& \frac{1}{1536}(-1+\zeta)(-1+\xi)(-366-250\zeta^2+625\zeta^4-250\xi^2+625\xi^4)\\
N_2(\xi,\zeta) =& \frac{1}{1536}(1-\zeta)(1+\xi)(-366-250\zeta^2+625\zeta^4-250\xi^2+625\xi^4)\\
N_3(\xi,\zeta) =& \frac{1}{1536}(1+\zeta)(1+\xi)(-366-250\zeta^2+625\zeta^4-250\xi^2+625\xi^4)\\
N_4(\xi,\zeta) =& \frac{1}{1536}(1+\zeta)(1-\xi)(-366-250\zeta^2+625\zeta^4-250\xi^2+625\xi^4)\\
N_5(\xi,\zeta) =& \frac{25}{1536}(1-\zeta)(-1+\xi)(1+\xi)(-3+5\xi)(-1+5\xi)(1+5\xi)\\
N_6(\xi,\zeta) =& \frac{25}{1536}(-1+\zeta)(1+\zeta)(-3+5\zeta)(-1+5\zeta)(1+5\zeta)(1+\xi)\\
N_7(\xi,\zeta) =& \frac{25}{1536}(1+\zeta)(1-\xi)(1+\xi)(-1+5\xi)(1+5\xi)(3+5\xi)\\
N_8(\xi,\zeta) =& \frac{25}{1536}(-1+\zeta)(1+\zeta)(-1+5\zeta)(1+5\zeta)(3+5\zeta)(-1+\xi)\\
N_9(\xi,\zeta) =& \frac{25}{768}(-1+\zeta)(-1+\xi)(1+\xi)(-3+5\xi)(-1+5\xi)(3+5\xi)\\
N_{10}(\xi,\zeta) =& \frac{25}{768}(1-\zeta)(1+\zeta)(-3+5\zeta)(-1+5\zeta)(3+5\zeta)(1+\xi)\\
N_{11}(\xi,\zeta) =& \frac{25}{768}(1+\zeta)(-1+\xi)(1+\xi)(-3+5\xi)(1+5\xi)(3+5\xi)\\
N_{12}(\xi,\zeta) =& \frac{25}{768}(1-\zeta)(1+\zeta)(-3+5\zeta)(1+5\zeta)(3+5\zeta)(-1+\xi)\\
N_{13}(\xi,\zeta) =& \frac{25}{768}(1-\zeta)(-1+\xi)(1+\xi)(-3+5\xi)(1+5\xi)(3+5\xi)\\
N_{14}(\xi,\zeta) =& \frac{25}{768}(-1+\zeta)(1+\zeta)(-3+5\zeta)(1+5\zeta)(3+5\zeta)(1+\xi)\\
N_{15}(\xi,\zeta) =& \frac{25}{768}(1+\zeta)(1-\xi)(1+\xi)(-3+5\xi)(-1+5\xi)(3+5\xi)\\
N_{16}(\xi,\zeta) =& \frac{25}{768}(-1+\zeta)(1+\zeta)(-3+5\zeta)(-1+5\zeta)(3+5\zeta)(-1+\xi)\\
N_{17}(\xi,\zeta) =& \frac{25}{1536}(-1+\zeta)(-1+\xi)(1+\xi)(-1+5\xi)(1+5\xi)(3+5\xi)\\
N_{18}(\xi,\zeta) =& \frac{25}{1536}(1-\zeta)(1+\zeta)(-1+5\zeta)(1+5\zeta)(3+5\zeta)(1+\xi)\\
N_{19}(\xi,\zeta) =& \frac{25}{1536}(1+\zeta)(-1+\xi)(1+\xi)(-3+5\xi)(-1+5\xi)(1+5\xi)\\
N_{20}(\xi,\zeta) =& \frac{25}{1536}(1-\zeta)(1+\zeta)(-3+5\zeta)(-1+5\zeta)(1+5\zeta)(-1+\xi)
\end{aligned}
$$

Vita

Eric Michael Austin was born on September 3, 1959, in Aurora, Illinois, the second child of George and Dolores Austin. He graduated from the University of Illinois at Urbana-Champaign in May, 1980, with Bachelor of Science in General Engineering and in January, 1982, with a Masters of Science in Theoretical and Applied Mechanics. He joined Anamet Laboratories, Inc., of San Carlos, CA, in October, 1981, and left in January, 1983, when three key technical members of Anamet formed CSA Engineering, Inc., of Palo Alto, CA. Eric left industry after 12 years to pursue a Ph.D. in Engineering Mechanics at Virginia Polytechnic Institute and State University starting in January, 1994, under the supervision of Prof. Daniel J. Inman. In June of 1995 he married the former Elizabeth Goodpaster, and together they have celebrated the birth of Margaret Ann Austin in June of 1996 and Gavin Winchester Austin in April of 1998. Upon graduation, Eric plans to remain at Virginia Tech as a postdoctoral research associate under Prof. Inman while looking for a faculty position in academia.

Eric M. Austin